Genesis of the Rockstone graphite showing, Shebandowan Greenstone Belt, Western Superior Province, Canada

by

Gokhan Yildirim

A Thesis submitted to the Faculty of Graduate Studies of The

University of Manitoba

in partial fulfilment of the requirements of the degree of

MASTER OF SCIENCE

Department of Earth Sciences

University of Manitoba

Winnipeg, Manitoba, Canada

ABSTRACT

Beyond its economic significance as a critical mineral, graphite provides valuable insights into the early carbon cycle and the environmental conditions of early Earth. The origin of graphite in Precambrian rocks has been a longstanding subject of interest in geological studies, owing to the possibility that it could represent remnants of early life on Earth. At the Rockstone property in Thunder Bay, Ontario, graphite occurs as very fine-grained particles (~10 to 80 μm) within late-stage chlorite–sulfide–quartz veins hosted by Neoarchean metasedimentary and metavolcanic rocks. Transmitted Electron Microscopy and Raman studies confirm that graphite is predominantly poorly crystalline and exhibits a turbostratic structure, which is indicative of deformation. Ti-in-biotite geothermometry yields peak amphibolite facies temperatures between ~500 and 565°C (±50°C). Raman temperatures of graphite are lower, varying from ~350 to 465°C (±50°C). Chlorite, interpreted to be in textural equilibrium with graphite, yields temperatures ranging from ~110 to 280°C (±20°C). *In situ* $\delta^{13}C_{VPDB}$ values of vein graphite ranges between -41.1 to -33.3‰ with a median of -36.7‰ (n=28) and indicates that the carbon is biogenic. *In situ,* sulfur isotope values ($\delta^{34}S_{VCDT}$) of pyrite, sphalerite and pyrrhotite, vary from -0.5 to +6.7‰ with a median of +2.4‰ (n=55), which fall within the range characteristic of both metamorphic and igneous origins and are comparable to other sulfur isotope values of Archean VMS deposits in the Superior Province. Overall, our data indicates that organic matter was impacted by graphitization processes during regional metamorphism. Subsequently, vein graphite, highly depleted in ^{13}C, might have formed from two main processes: (1) devolatilization of organic matter during low-grade metamorphism, and/or (2) migration from an existing graphite body at depth, during regional metamorphism. Alternatively, The Fischer-Tropsch (FT) reactions may have involved in the deposition of graphite at Rockstone. The occurrence of graphite within veins, closely associated with hydrous minerals such as chlorite and muscovite, as well as sulfide minerals, supports this interpretation.

ACKNOWLEDGMENTS

First and foremost, I would like to express my sincere and profound gratitude to my advisor, Dr. Alfredo Camacho, for his unwavering academic guidance and financial support during my MSc study. It has been a privilege to be his student, and I will always take pride in that. I am also deeply grateful to my committee members, Dr. Andrew G. Conly and Dr. Mostafa Fayek, for their continuous support, valuable insights, and thoughtful discussions, which greatly contributed to the development and improvement of this study.

My heartfelt thanks go to Dr. Panseok Yang, Dr. Michael Schindler, Ryan Sharpe, and Adam Snyder whose generosity in sharing their expertise and guidance during the laboratory phase. Their support and mentorship were vital to the success of this research. I would like to thank Mr. Ken Kukkee for granting access to the drill cores. This research would not have been possible without his support. Special thanks go to Dr. Karen Ferreira for her assistance with the preparation and editing of the thesis text, and to Dr. Biltan Kurkcuoglu for the many insightful discussions and support throughout this journey. I am also very grateful to Dr. Andrew M. McDonald from Laurentian University for his assistance with the Raman analyses.

I would like to extend my deepest appreciation to the Republic of Turkey and its Ministry of National Education for providing the financial support that enabled me to pursue my master's degree in Canada.

I am also thankful to the faculty, staff, and fellow graduate students for their support during my time in the program. Finally, I wish to express my deepest gratitude to my wife, who accompanied me to Canada and stood by me every step of the way, and to my parents, whose moral support has been the foundation of my academic journey.

Table of Contents

List of Figures

List of Tables

CHAPTER 1 – INTRODUCTION

1.1) Overview

In response to the recent global shift to clean energy, the world demand has significantly increased for natural graphite, an allotrope of carbon formed mainly by metamorphic and hydrothermal processes in Earth's crust (Beyssac and Rumble, 2014). Consequently, in today's market, graphite is considered a critical raw material and is essential in Li-ion battery technology, industrial applications (e.g., automobile, steel, refractories, nuclear and solar energy equipment), and nanotechnology (as a source of graphene, i.e., single hexagonal planar layers of carbon atoms; Luque et al., 2014; Beyssac and Rumble, 2014; Robinson et al., 2017; European Commission 2020; Natural Resources Canada 2023). As a result, the exploration, production, and determination of geological properties of graphite occurrences are increasing globally. According to USGS National Minerals Information (2024) for graphite, Canada ranks 9th within the top 10 graphite-producing countries of the world, with approximately 5.7-million-ton world reserves, which equates to 2.17% of the total world graphite reserves (Fig. 1.1).

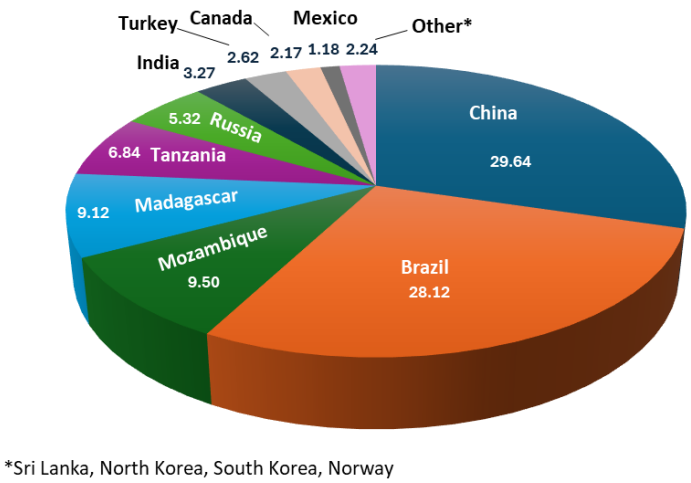

Figure 1.1: *Global graphite reserves by country in percent. Based on data from USGS National Minerals Information (2024).*

The advantages of graphite over other elements stem from having a high melting point (~3,550°C), high chemical resistance, excellent thermal and electrical conductivity (Spence, 1920; Hewitt, 1965; Taylor, 2006), and both metallic and non-metallic properties (Beyssac and Rumble, 2014). Although natural and synthetic graphite are widely used in a variety of fields (e.g., batteries, refractories and lubricants; Beyssac and Rumble, 2014), natural graphite has become the preferred commodity, as synthetic graphite is very costly to produce in today's economic market as it is energy-intensive. In addition to these properties, natural graphite can be used in the investigation of geological processes, such as tracing of the carbon cycle and early life in the biosphere (Beyssac and Rumble, 2014). To this end, a variety of studies pertaining to natural graphite formations, their geologic characteristics and origin have been published in the literature in recent years (e.g., Conly and Moore, 2015; Pascal et al., 2016a; 2016b; Taner et al., 2017; Song et al., 2022; Toma et al., 2022; Al-Ani et al., 2022; Ren et al., 2022; Case et al., 2023; Drever et al., 2023; Coueslan, 2023; Engvik et al., 2023; Toma et al., 2024).

In this regard, the characterization of graphite formations in Archean greenstone belts in Canada can positively affect graphite exploration. This project elucidates the mineralogical and geochemical character and determines the origin of a graphite formation in the Shebandowan greenstone belt near Thunder Bay, Ontario. Understanding the features of this graphite and the processes that led to its deposition could potentially help bring this mineral occurrence into production.

1.2) Features, Formation and Classification of Natural Graphite

Natural graphite is a form of pure elemental carbon: opaque, very soft (0.5 to 2 on the Mohs hardness scale), dark grey to black in colour, with a metallic lustre in hand specimen. It has a crystalline structure, composed of stacks of graphene, with each graphene sheet comprising

six carbon atoms. Based on the spatial order of carbon atoms in a basal plane of graphite, there are mainly two polytypes, which are hexagonal and less commonly rhombohedral (Bernal, 1924; Lipson and Stokes, 1942; Li et al., 2007). Hexagonal graphite, α-graphite, shows ABABAB sequences; rhombohedral graphite, β-graphite, shows an ABCABC arrangement (Fig. 1.2; Reynolds, 1968). The thermodynamically stable polytype of graphite in nature is hexagonal graphite. It has a fully ordered crystallite structure, with an interplanar spacing (d_{002}) of ~0.335 nm, ~3.34 Å); its unit cell has dimensions of a ≈ 2.46 Å (0.246 nm) and c ≈ 6.708 Å (0.6708 nm) (Fig. 1.2; Reynolds, 1968; Landis, 1971; Luque et al., 1993). The rhombohedral polymorph of graphite is metastable and can be formed by shear deformation of hexagonal graphite (Verma and Quraishi, 2023). Furthermore, it can be produced by mechanical (e.g., milling) and thermal changes in laboratory (Freise and Kelly, 1963; King, 2006).

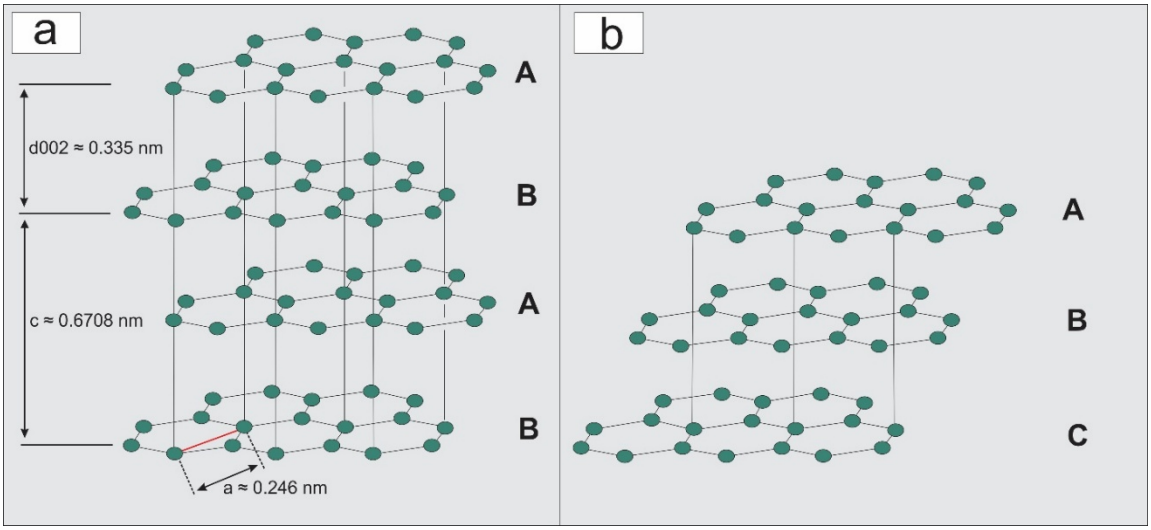

Figure 1.2: *Hexagonal (a) and rhombohedral (b) lattice of graphite (modified from Reynolds, 1968).*

Turbostratic graphite, a type of deformation of hexagonal graphite, is also called disordered graphite and is considered a variation of hexagonal graphite. It has generally

disordered stacking, curved-shaped at the edges of graphene and with increased d-spacing between graphene layers. Turbostratic modifications are mainly caused by deformation and mechanical changes (e.g., milling). If the milling process is lengthy, amorphous carbon can be formed (Li et al., 2007; Conly and Moore, 2015; Qing et al., 2017).

Natural graphite generally is composed of ordered (hexagonal) and lesser disordered crystal forms (Kwiecinska, 1978; Kwiecinska and Petersen, 2004). This combination tends to give information about the degree of graphite crystallinity as well as the metamorphic degree of carbonaceous matter: as temperature increases, d-spacing between the graphene layers becomes narrower and finally, the crystallinity of graphite gradually becomes ordered. Overall, the degree of graphite crystallinity is mainly controlled by increasing temperature (Pasteris and Wopenka, 1991). The lengths between hexagonal graphite sheets (L_a) (basal planes) and the stacking height of graphene layers (L_c) (edge planes) control the form of fully ordered graphite (Fig. 1.3). Therefore, quantitative d-spacing, L_a and L_c parameters indicate the degree of graphite crystallinity (Fig. 1.3; Pasteris and Wopenka, 1991; Beyssac and Rumble, 2014).

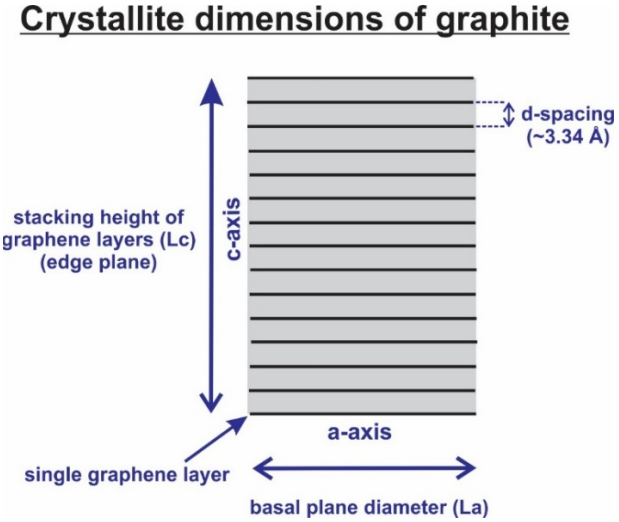

Figure 1.3: *Schematic view of graphite showing the main quantitative crystallite parameters (modified from Pasteris and Wopenka, 1991).*

Characterization of graphite crystallinity can be done by X-ray diffractometry (XRD), micro-Raman spectroscopy, and high-resolution transmission electron microscopy (HRTEM) (Pasteris and Wopenka, 1991). In this study, micro-Raman and HRTEM techniques are used.

In addition to large graphite crystals (>300 μm), fine-grained varieties, namely microcrystalline and cryptocrystalline graphite, also occur in nature (Barrenechea et al., 2009; Drever et al., 2023). These two terms, *cryptocrystalline* and *microcrystalline* graphite, are frequently used alternatively to describe graphite with very fine grain sizes. Although they refer to essentially the same material, a distinction is often made based on the visibility of individual crystals under magnification (Simandl et al., 2015). When individual fine-grained graphite crystals can be observed under a light microscope, the crystal is referred to as microcrystalline graphite. In contrast, cryptocrystalline graphite typically consists of grains smaller than 10 μm, which are not clearly visible under a light microscope (Barrenechea et al., 2009; Luque et al., 2012).

Graphite is generally thought to form during regional and/or contact metamorphism of organic and/or inorganic carbon compounds, which can be chiefly found in sedimentary rocks, but can also form through precipitation from C-O-H fluids (carbon dioxide or methane-rich) that originated from hydrothermal systems in different tectonic systems (Fig. 1.4; Luque et al. 2012; 2014; Beyssac and Rumble, 2014). Most graphite formations around the world formed mainly in Precambrian rocks with different origins and depositional types (Table 1.1; King, 2006; Parnell et al., 2021).

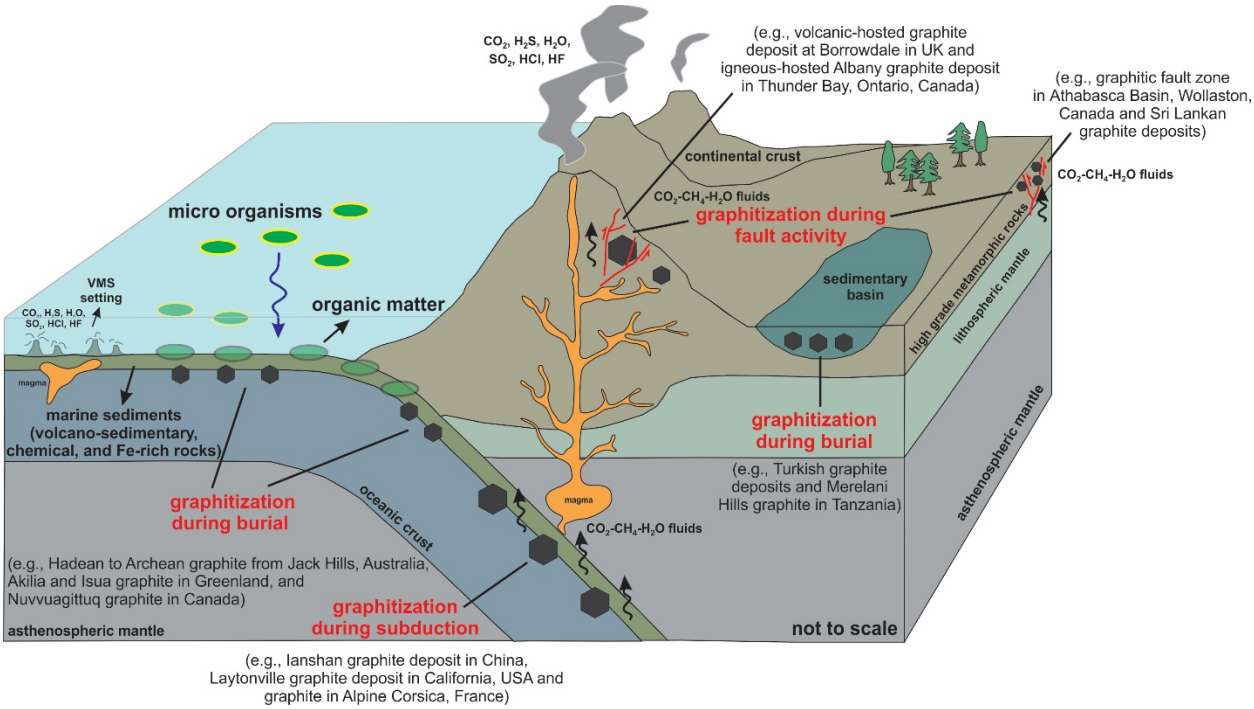

Figure 1.4: *Some examples of depositional settings of graphite within the Earth's crust within different tectonic settings (modified from Beyssac and Rumble 2014). Graphite with organic carbon originates from the preservation of organic matter during burial, subduction and subsequent geologic processes. Mantle- and carbonate- derived carbon can originate from during subduction and fluids within mid and lower crustal fault-controlled environments (Galvez et al., 2013)*

Table 1.1: *A range of various Precambrian graphite localities around the world and their geological features.*

Location	Host Rock	Age	Deposit Type	Origin of Carbon	References
Sri Lankan graphite, Sri Lanka	Garnet-biotite quartzo-feldspathic gneiss, calc-silicate gneiss	~1-3.4 Ga	Epigenetic (fluid-derived)	Mantle	Luque et al., 2012; Touret et al., 2019
Bissett Creek graphite, Ontario, Canada	Quartzo-feldspathic gneiss	~1-1.6 Ga	Syngenetic and epigenetic (fluid-derived)	Organic	Taner et al., 2017; Drever et al., 2022
Montpellier graphite, Quebec, Canada	Metavolcanic and metasedimentary rocks (quartzite, paragneiss, and calc-silicate)	~1-1.6 Ga	Syngenetic and minor contribution from fluids (epigenetic)	Organic with minor carbonate	Taner et al., 2017
Lac Knife graphite, Quebec, Canada	Pelitic mica-graphite rich schist with some calc-silicate bands	~1.8 Ga	Syngenetic and epigenetic (fluid-derived)	Possible organic	Birkett et al., 1989; Simandl and Kenan 1997
Albany graphite, Ontario, Canada	Quartz syenite to diorite to nepheline syenite	~> 2.6 Ga	Epigenetic (fluid-derived)	Mantle	Conly and Moore 2015
Duluth graphite, Minnesota (USA)	Sulfide-bearing igneous rocks and pelitic metasediments	~1.1 Ga	Epigenetic (fluid-derived)	Organic	Hollister, 1980; Ripley and Taib 1988; Paces and Miller 1993
Rautalampi and Kapysuo graphite, central Finland	Quartz-mica schist and feldspathic hornblende biotite gneiss	~1.8-2 Ga	Syngenetic	Organic	Al-Ani et al., 2022
The Lewisian graphite, Scotland	Carbonaceous pelites and schists	~1.8–2.1 Ga	Syngenetic and epigenetic (fluid-derived)	Organic and carbonate	Parnell et al., 2021

The formation of graphite deposits is controlled by parameters such as tectonic setting, metamorphic conditions and carbon content in the fluids and/or in the host rocks (Fig. 1.4; Luque et al., 2012). For example, in subduction zones, graphitization might take place with increasing temperature and pressure (Galvez et al., 2013; Beyssac and Rumble, 2014). In continental settings, both graphite is produced in sedimentary basins during burial and precipitated by carbon-bearing fluids during fault activity in fault zones (Fig. 1.4; Beyssac and Rumble, 2014; Toma et al., 2022 and references therein).

Traditionally, the classification of graphite has been based primarily on crystal size (i.e., microcrystalline, flake and vein graphite) according to commercial demands, whereas geological factors have generally been incidental (Simandl et al., 2015). However, in a geological context, natural graphite can be basically divided into two classes as either a syngenetic or an epigenetic deposit (Luque et al., 2014; Conly and Moore, 2015). In syngenetic formations, carbonaceous material is transformed from structurally disordered to fully ordered graphite by contact and/or regional metamorphism — this transformation also known as graphitization (Rumble and Hoering, 1986; Rumble et al., 1986; Kwiecinska and Petersen, 2004). As for epigenetic occurrences, graphite develops from the precipitation of carbon-bearing fluids/melts such as CO_2 and/or CH_4 through major fault or/and vein systems, and thus, structurally controlled vein graphite might form within this epigenetic formation (e.g., Sri Lankan graphite deposits; Luque et al., 2014; Touret et al., 2019).

1.3) Origin of the Carbon Component

Three main sources of carbon can be identified in graphite: (1) organic-biogenic compounds, (2) carbonate rocks such as marble and marine carbonates, and (3) mantle sources

(Luque et al., 2012). These different reservoirs have distinct carbon isotopic ranges. For example, $\delta^{13}C$ for organic carbon ranges from ~ -40 to -10‰ with a mean value of ~ -23‰. This organic carbon signature is isotopically light. Graphite derived from marine carbonates, which is abiogenic/inorganic origin, has a narrow $\delta^{13}C$ range from -2 to +2‰ (average 0‰), which is higher and isotopically heavier than the value for organic matter. Finally, the $\delta^{13}C$ for mantle carbon ranges from approximately -3 to -10‰, which is heavier than for organic carbon (Weis et al., 1981; Hahn-Weinheimer and Hirner, 1981; Schidlowski, 1987). However, in some circumstances, a carbon isotopic signature may be modified by decarbonization reactions and/or CO_2-rich fluids that originated from mantle, which enables the carbon isotope ratio in graphite to have a heavy isotopic signature compared with the value for organic matter (Weis et al., 1981; Hahn-Weinheimer and Hirner, 1981; Schidlowski, 1987; Rollinson, 1993; Clark and Fritz, 1997; Schidlowski, 2001; Deines, 2002; Faure and Mensing, 2005; Luque et al., 2012; Dissanayake 2013; Luque et al., 2014). In subduction zones, organic and inorganic matter have been transmitted to the mantle depths exceeding ~90 km (Fig. 1.4; Hu et al., 2023). Therefore, carbon can be transformed into graphite or diamond with burial and ultra-high-pressure (UHP) metamorphism (Hu et al., 2023). In this type of setting, the carbon isotope signature of graphite tends to have light $\delta^{13}C$ values. However, if the carbon in graphite is derived from these three components, $\delta^{13}C$ values tend to have a wide range that indicates all three of mantle, carbonate and organic carbon components (Hu et al., 2023).

Identifying the source and thus the geologic environment can become complicated when metamorphic graphite interacts with fluid-precipitated graphite (Luque et al., 2012; Drever et al., 2023). Alternatively, there might be two distinct origins (i.e., organic and inorganic carbon) and two types of graphite formations (metamorphic and fluid-derived) in one graphite deposit

(Parnell et al., 2021). Evaluating the principal source and depositional environment can mainly be solved by using carbon isotope measurements supported with isotope data from other paragenetically equivalent sulfide minerals such as pyrite, pyrrhotite and sphalerite. More importantly, the determination of carbon isotopes in graphite is fundamental to identify whether the origin of carbon is organic or inorganic and to detect possible fluid-mixing scenarios that enabled graphite precipitation and to comprehend graphite evolution during geological time (Luque et al., 2012).

1.4) The Rockstone Property

The project area, the Rockstone Property, is situated approximately 50 km west of Thunder Bay, Ontario (Fig. 1.5) in the Archean Shebandowan greenstone belt.

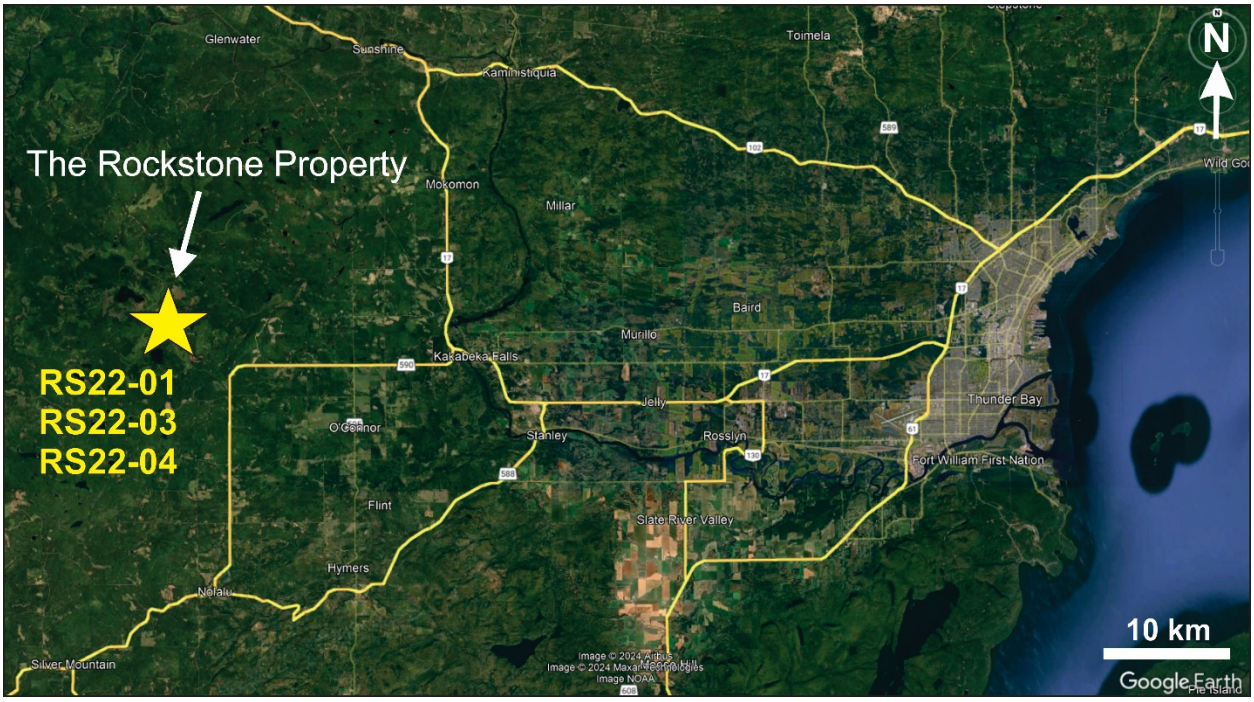

Figure 1.5: *Google Earth view of the roads to the Rockstone Property and its surroundings. The yellow star indicates the locations of drill holes (RS22-01, RS22-03 and RS22-04) that intersected graphite.*

Graphite samples were collected from diamond drill core from three holes drilled in the north part of Marks Township. These holes were drilled by Greencastle Resources Ltd. in 2012 (Cullen and Garry-Clark, 2014). In 2012, while investigating potential copper-zinc volcanogenic massive sulfide (VMS) mineralization, Greencastle Resources Ltd. identified a graphitic argillite unit on the Rockstone Property. Deveron Resources Limited is now interested in graphite for economic purposes (Cullen and Garry-Clark, 2014). The drill hole coordinates are as follows: (1) DDH RS22-01, 5364770 N, 291263 E, (2) DDH RS22-03, 5364817 N, 291221 E, and (3) DDH RS22-04, 5364830 N, 291228E (UTM Zone 16N NAD83). The property is reachable from Kakabeka Falls on the east by Highway 590 (Fig. 1.5). The area is accessible by road year-round.

Generally, Rockstone graphite shows evidence of low-grade regional metamorphism, that is shown by alteration of mineral assemblages and textures (Cullen and Garry-Clark, 2014). Carbon remobilization zones are indicated by structural elements such as brecciation and a vein like system within the Rockstone graphite formation. Furthermore, the volcano-sedimentary hosted graphitic zone contains sulfide minerals such as mainly pyrite, pyrrhotite, sphalerite and minor chalcopyrite and galena. Therefore, this type of setting might reflect deposition of graphite in a possible Archean marine environment. In summary, the characteristics, depositional conditions, origin of carbon, peak metamorphism temperature and thermal maturity of the Rockstone graphite have not been fully studied. This project is designed to provide data to resolve some of these outstanding questions.

1.5) Objectives of the Project

The aims of this study are as follows: (1) Describe petrographically the graphite and determine mineral paragenesis, surface morphology and textural information using transmitted and reflected-light microscopes and scanning electron microscopy (SEM). (2) Characterize

carbon atom arrangements, such as the stacking pattern of graphene and identify lattice defects of graphite, where applicable, using transmission electron microscopy (TEM), especially the high-resolution TEM (HRTEM) technique. (3) Characterize the graphite quantitatively and estimate the degree of metamorphism/graphitization of carbonaceous matter and its host rock using in-situ micro-Raman spectroscopy. (4) Characterize chlorite and biotite mineral chemistry (associated with graphite formation) to estimate chlorite and Ti-in-biotite temperatures. In addition to the micro-Raman geothermometer, the chlorite and Ti-in-biotite geothermometers are used to correlate the temperatures that led to graphite formation. By doing this, the results from multiple thermometers are evaluated to constrain the temperature range that precipitated graphite. (5) Identify the carbon isotopic composition of graphite to determine whether the graphite is biogenic or abiogenic. (6) Identify the sulfur isotopic composition of sulfide minerals like pyrite, pyrrhotite and sphalerite that are directly associated with graphite to evaluate depositional environments using secondary ion mass spectrometry (SIMS). (7) Finally, synthesize all of the data to understand the evolution of the Rockstone graphite formation and its deposition mechanism.

CHAPTER 2 – GEOLOGIC SETTING

2.1) Regional Geology

The Rockstone property is situated in the western part of the Wawa Subprovince of the Superior Province of the Canadian Shield (Fig. 2.1; Thurston, 1991; Percival, 2007; Percival and Easton, 2007; Percival et al., 2012). The Superior Province, by far the largest Archean craton on Earth (Thurston, 1991; Percival et al., 2012), consists of Archean oceanic and continental crustal components originating mainly from subduction events and/or plume-dominated settings. Defined by structural, lithological, geochemical, geochronological and metallogenic properties, the Superior Province comprises generally linear, east-trending, fault-bounded subprovinces (Fig. 2.1; Card and Ciesielski, 1986; Percival and Easton, 2007; Percival et al., 2012) with different major characteristics: volcano-plutonic (granite-greenstone), metasedimentary, gneissic-plutonic and high-grade gneissic (Card and Ciesielski, 1986; Thurston, 1991; Percival and Easton, 2007; Percival et al., 2012). The province is surrounded by the Hudson Bay and Moose River Basins of Phanerozoic age (mainly Paleozoic and Mesozoic sequences) on the north, northeast and southernmost, Proterozoic units on the northwest, and the Southern and Grenville Provinces on the south and southeast (Thurston, 1991; Percival, 2007; Card and Ciesielski, 1986; Stott, 2011; Fig. 2.1).

Figure 2.1: *Major tectonic subdivisions of the Superior Province (modified from Thurston, 1991; Stott, 2011; Percival et al., 2012). The yellow star indicates the location of the sampling area.*

2.1.1) Wawa Subprovince

The Wawa Subprovince is an amalgamation of several Neoarchean greenstone belts and tonalite and granodiorite units with massive, foliated and gneissic characteristics. It trends east – west and is tectonically bounded by the Quetico Subprovince in the north. Its southwest boundary is constrained by the Proterozoic Animike Basin; Abitibi supracrustal units with the Kapuskasing structural zone are situated to the east (Figs. 2.1, 2.2; Williams et al., 1991; Percival et al., 2012). Furthermore, the western part of the Wawa subprovince is intruded by Mesoproterozoic Logan diabase sills (quartz-normative tholeiites) (Fig. 2.2; Blackadar, 1956; Weiblen et al., 1972; Jones, 1984; Blackburn et al., 1991). Because of the abundance of iron and gold deposits in the subprovince, the terrane has been subjected to many geologic investigations (Lodge et al., 2015, and references therein).

Greenstone belts in the Wawa subprovince mainly contain komatiitic to tholeiitic and calc-alkalic basalt, intermediate to felsic volcanic rocks such as dacite and rhyolite, and metasedimentary rocks as such turbiditic wacke, conglomerate, and iron formations (Williams et al. 1991). The boundaries and relationships between these units are structurally controlled and commonly remain unclear. The westernmost part of the Wawa Subprovince includes the Shebandowan greenstone belt, in which the study area is located (Fig. 2.2; Williams et al., 1991; Berger, 1993; Rogers and Berger, 1995).

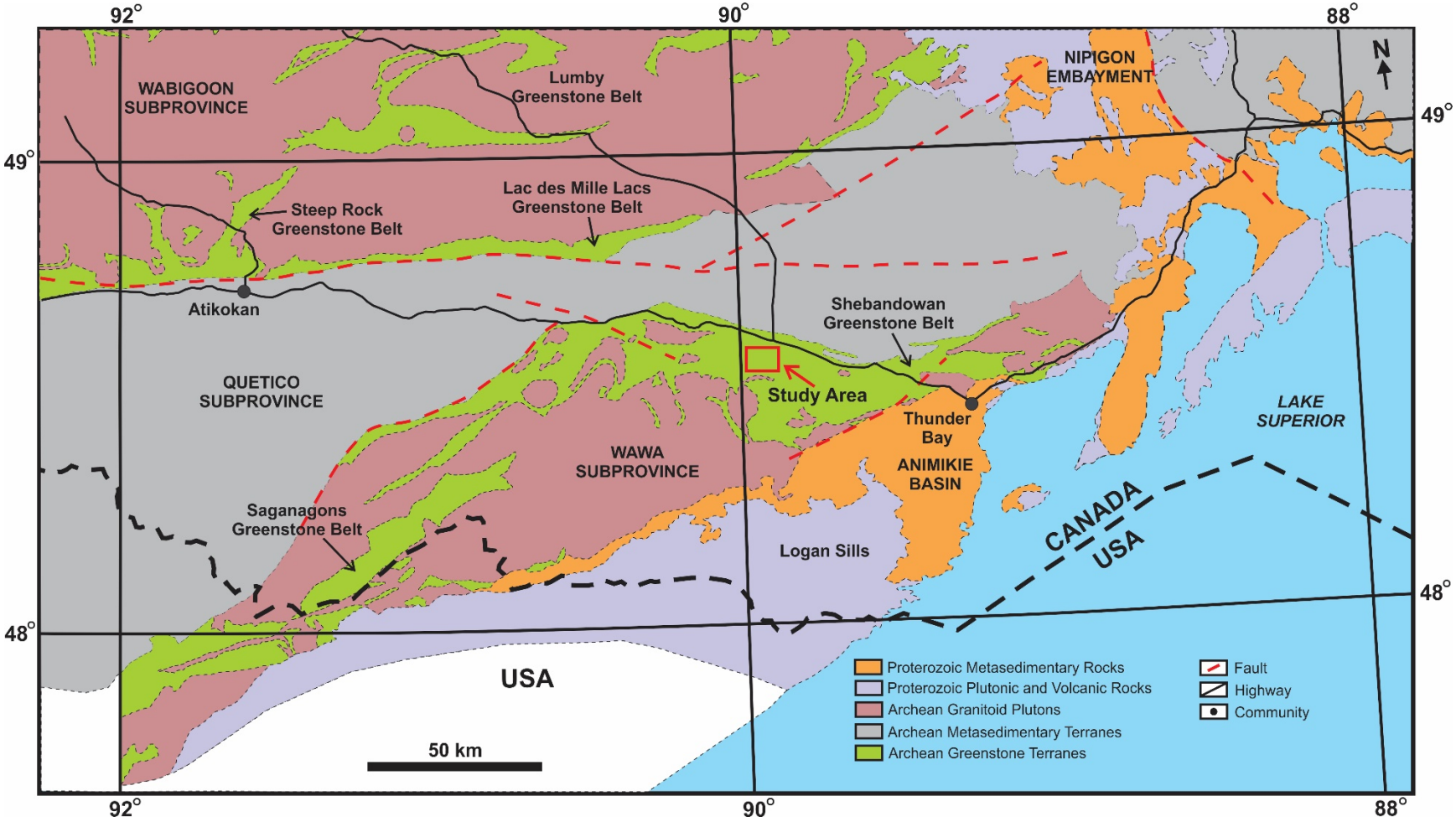

Figure 2.2: *Regional geology along the northwest shore of Lake Superior, Ontario (modified from Santaguida, 2001).*

2.1.2) Shebandowan Greenstone Belt

The Rockstone graphite is hosted by the Shebandowan greenstone belt (SGB) within the Wawa Subprovince (Rogers and Berger, 1995). Approximately 150 km in length, the SGB stretches from Thunder Bay in the east to the Minnesota (USA) – Canada border in the southwest (Fig. 2.2). The SGB has been mapped by many researchers at various scales from regional to property (e.g., Corfu and Stott, 1986; Stott, 1986; Kehlenbeck, 1988; Carter, 1990; Williams et al., 1991; Berger, 1993; Rogers and Berger, 1995), and it has attracted attention for many years in terms of mineral exploration for gold, copper, zinc, and graphite (Chorlton, 1987; Williams et al., 1991; Corfu and Stott, 1998; Stott and Schnieders, 1983; Jobin-Bevans and Cullen, 2006; Cullen and Garry-Clark, 2014; Lodge et al., 2015). The SGB was formed *ca.* 2.7 Ga, based on tests of detrital zircons (Corfu and Stott, 1998; Hart, 2007; Lodge et al., 2015). The SGB, curved in shape and broadly northeast-southwest trending, is in fault contact with the Quetico Subprovince and felsic to intermediate intrusive rocks (e.g., granodiorite, diorite, tonalite) to the north, and is overlain by the Proterozoic Animikie Basin to the south and southeast. The western boundary of the SGB is intruded by granitoid plutons of the Wawa subprovince (Fig. 2.2; Rogers and Berger, 1995).

The supracrustal rocks of the SGB are classified into two assemblages, the Greenwater and Shebandowan, described below (Williams et al., 1991; Berger, 1993; Rogers and Berger, 1995). The supracrustal units experienced lower to middle greenschist-facies regional metamorphism. In some areas, the effect of metamorphism is increased to upper greenschist and lower amphibolite facies in supracrustal rocks in the contact zones of granitic intrusions (Rogers and Berger, 1995). Furthermore, two regional deformation events affected the supracrustal rocks of the SGB. The deformation history of the earliest assemblages of the SGB is poorly

understood. The earliest deformation event (D_1; 2696 ± 2 Ma) caused generally northwest-trending isoclinal folds and foliations and westward-stretching mineral lineation with schistosity striking east-west and dipping to the north, only locally seen in rocks of the Greenwater assemblage (Williams et al., 1991; Rogers and Berger, 1995; Harris et al., 2023). The emplacement of the granitoid rocks, associated with calc-alkaline magmatism, to the south of the region might have caused the D_1 event. Therefore, the supracrustal rocks of the Greenwater assemblage were deformed by D_1. As for the second deformation event (D_2, between 2685 and 2680 Ma), it is characterized by regional folds, brittle and ductile shear zones, which host of gold deposits, that are associated with Kenoren orogeny and regional metamorphism and these structural elements overprint all metavolcanic and metasedimentary rocks of the SGB (Corfu and Stott, 1998; Harris et al., 2023). D_2 caused east-striking mineral foliations and folds, especially in the Shebandowan assemblage. These folds are regional in scale and crossed by northeast- and northwest-trending faults, which postdate first and second deformation events (Stott and Schwerdtner, 1981; Stott and Schnieders, 1983; Stott, 1985; Williams et al., 1991).

2.1.2.1) Greenwater Assemblage

The Greenwater assemblage hosts the Rockstone graphite deposit. Furthermore, it also hosts magmatic Ni-Cu (e.g., Shebandowan Mine), VMS and gold deposits (e.g., Huronian and North Coldstream VMS mines, Greenwater Lake and Delta-1 gold mines) (Williams et al., 1991; Lodge et al., 2015). The Greenwater assemblage generally contains tholeiitic basalt, minor komatiitic basalt and pillowed flows. These are underlain by calc-alkalic andesite, dacite and rhyolite as well as clastic (mainly wacke, siltstone, mudstone, graphitic argillite, graphitic mudstone, conglomerate and minor biotite-hornblende gneiss, schist and even migmatite) and chemical (magnetite-ironstone, sulfide-bearing ironstone, and chert) metasedimentary rocks

(Williams et al., 1991; Rogers and Berger, 1995; Osmani, 1997; Corfu and Stott, 1998). The felsic volcanic units are up to 1 km in thickness (Thuston, 1984); however, all volcanic cycles constitute approximately 5 km thickness in this assemblage (Williams et al., 1991). Based on U-Pb dating of detrital zircons in felsic volcanic rocks, the age of the Greenwater assemblage ranges from 2722.6 ±3.0 to 2718.7 ±4.9 Ma (Corfu and Stott, 1998; Hart, 2007). According to Williams et al. (1991) and Percival (2007), the assemblage is considered to have been deposited in a subaqueous to partially subaerial island-arc environment. The Greenwater assemblage is broken up by a wide range of intrusions such as gabbro, granodiorite, monzonite, granite, diorite, syenite, and monzonite (Rogers and Berger, 1995).

2.1.2.2) Shebandowan Assemblage

The Shebandowan assemblage contains two groups of rocks: metasedimentary (lithic wacke, argillite, magnetite-argillite ironstone, sandstone, conglomerate) and minor metavolcanic (hornblende trachyandesite, diorite tuff, lapilli tuff, tuff breccia, syenite) rocks. Based on the tests on zircons from the volcaniclastic rocks, the U-Pb age of the assemblage is *ca.* 2690 Ma, younger than the rocks of the Greenwater assemblage (Corfu and Stott, 1998). The Shebandowan assemblage of the SGB is thought to have been deposited in a subaerial to a shallow marine environment (Shegelski, 1980; Lodge et al., 2013). In terms of economic potential, the Shebandowan assemblage is mainly known for gold deposits (e.g., Gold Greek and Gold Creek West; Williams et al., 1991; Corfu and Stott, 1986; Rogers and Berger, 1995; Corfu and Stott, 1998).

2.2) Geology of the Study Area

The project area is located in the eastern branch of the SGB (Williams et al. 1991), and the geology was examined by Berger (1993, scale 1:15 840) and Rogers and Berger (1995, scale 1:20 000) (Figs. 2.2 and 2.3).

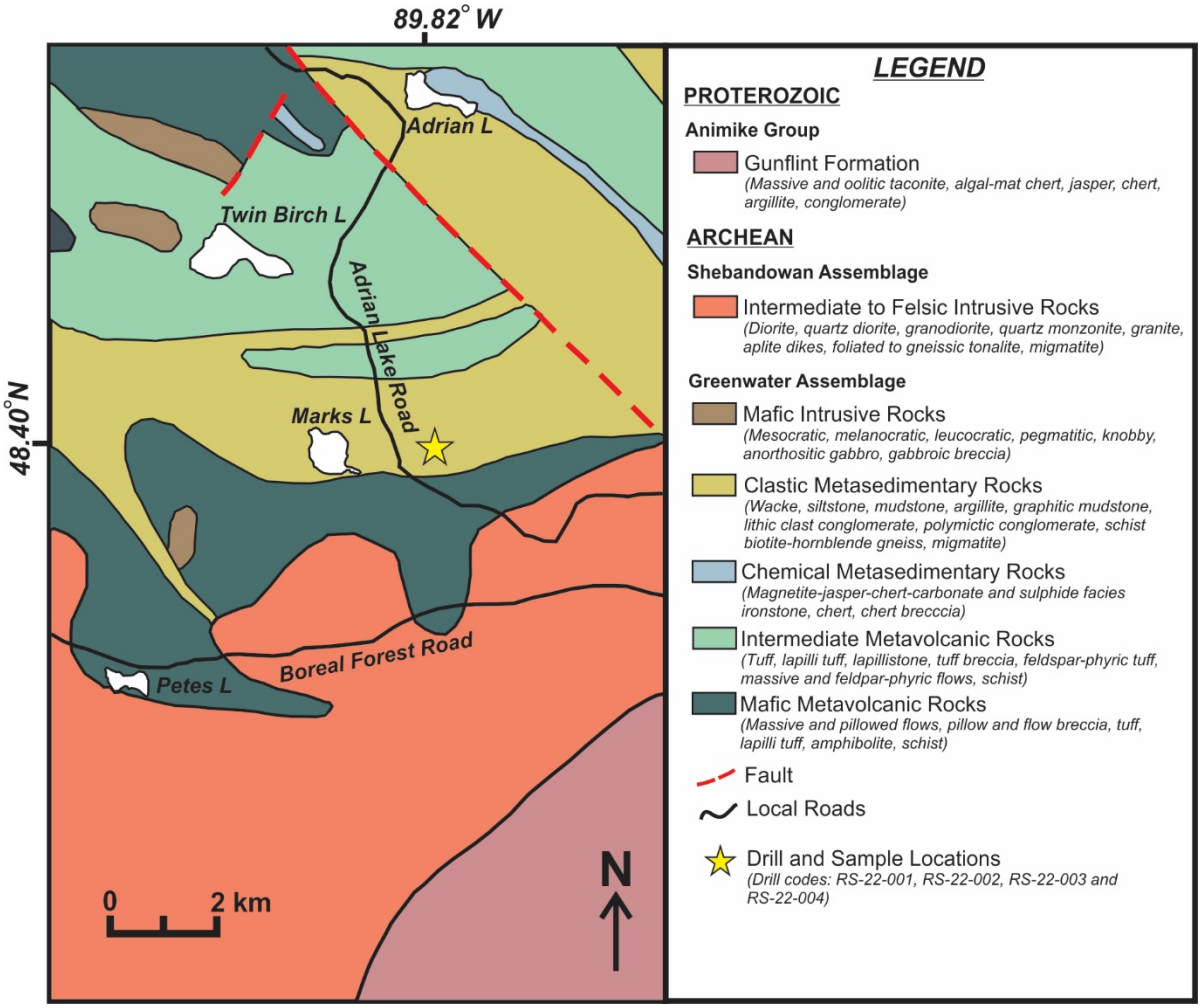

Figure 2.3: *Geology of the sampling area and location of the drill cores from which graphite-rich samples were taken (modified from Rogers and Berger, 1995).*

Within the project area is a range of mafic to felsic metavolcanic (i.e., amphibolite, dacitic and andesitic flows, basaltic dikes, tuff, lapilli tuff, tuff breccia, quartz-feldspar porphyry,

and schist) and metasedimentary (i.e., conglomerate, sandstone, wacke, arkose, arenite, iron formations and graphitic argillite) rocks. The area is intruded by mafic intrusive rocks (i.e., gabbro, gabbroic and komatiitic flows) in the north and felsic and intermediate intrusive rocks (i.e., granodioritic, dioritic, gneissic and tonalitic units) in the south (Fig. 2.3; Schneiders et al., 1998; Bajc, 1999).

Neoarchean supracrustal rocks unconformably underlie the Paleoproterozoic sedimentary rocks of the Gunflint Formation, which comprise taconite, chert, and algal-mat chert with minor conglomerate (Fig. 2.3). All of the Archean supracrustal rocks within the study area are affected by lower to middle greenschist facies regional metamorphism (Rogers and Berger, 1995).

Intermediate to felsic intrusive rocks are situated mainly in the south and intrude the supracrustal rocks of the Greenwater assemblage. This unit is mainly composed of gneissic tonalite, granodiorite, quartz monzonite and granite, with minor diorite, migmatite (Fig. 2.3; Williams et al. 1991). Mafic intrusive rocks are generally located in the northwest. These rocks include a variety of gabbro, mainly associated with mafic volcanic rocks of the Greenwater assemblage, with minor gabbroic breccia (Fig. 2.3). Mafic dykes a few meters in core length were identified in DDH RS22-01 and RS22-04 within intermediate volcaniclastics and tuff unit, respectively (Fig. 2.4).

Clastic metasedimentary rocks are one of the major lithologies in the study area. Among these rocks, mudstone and siltstone dominate the rock types within the region (Fig. 2.3). These are laminated, black in colour and contain, in some places, graphitic sequences. These rocks mainly are situated at the top of wacke units. Furthermore, mudstone and siltstone show turbiditic structures and massive to laminated features, which represent a deep-water basinal environment (Walker and James, 1992). The wacke unit is an extensive rock unit, especially in

the northern part of the study area. It is composed of intermediate tuff and mudstone and is thickly bedded and folded. Wacke and mudstone are frequently interbedded with intermediate tuff and lapilli tuff units within the study area. Grains of magnetite and hematite are also seen in the clastic metasedimentary rocks. Chemical metasedimentary rocks generally outcrop to the north and northeast of the study area (Fig. 2.3). They contain mainly chert, jasper-magnetite ironstone and sulfide-facies ironstone. Chert, interbedded with clastic metasedimentary rocks, is the most common chemical sedimentary rocks. Chert and ironstone units are generally interlayered with the clastic metasedimentary rocks. Especially southeast of the Adrian Lake, chert, graphitic and sulfidic mudstone are seen together. Widespread graphitic horizons within the clastic metasedimentary rocks are black and thickly laminated and thus they are fissile feature. Furthermore, they commonly contain disseminated pyrite. Graphitic argillite zones higher than ~5 meters in core length were identified in all drill holes (Fig. 2.4; DDH RS22-01, RS22-03 and RS22-04) Furthermore, graphite beds and graphite argillite layers were identified in DDH RS22-01 and RS22-03 within intermediate tuff units (Fig. 2.4).

Intermediate metavolcanic rocks are the other major rock type in the area, dominantly characterized by poorly and moderately sorted tuff and lapilli tuff (Figs. 2.3 and 2.4). They are chiefly wide and discontinuous, averaging around 50 meters in apparent thickness in drill core, and interbedded with clastic metasedimentary rocks (wacke and mudstone) within the project area. Generally, nearer the graphitic argillite units, it is observed that the tuff units contain graphite argillite layers (making up 10% of the intermediate tuff unit) and graphite beds (5%). In DDH RS22-01, the apparent thickness of the graphite-bearing portion of the intermediate tuffaceous is ~45 m, including 5 m of graphitic argillite (Fig. 2.4). Intermediate metavolcanic rocks within the study area show that they are deposited in deep water because of their massive

features and interbedding with other sedimentary rocks. As for felsic metavolcanic rocks, they are mainly composed of lithic tuff and lapilli tuff with minor quartz porphyry.

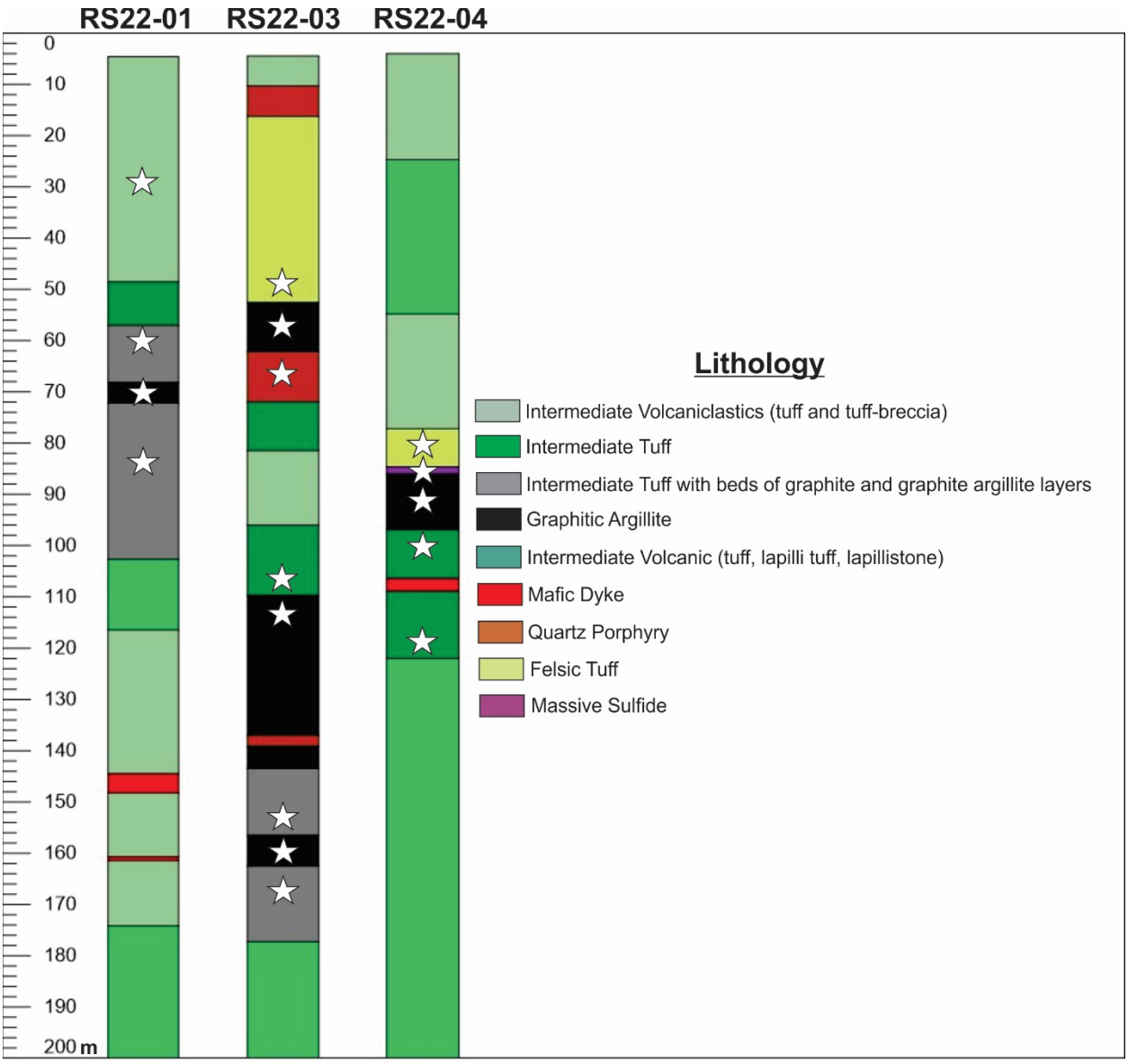

Figure 2.4: *Stratigraphic sections of the Rockstone property lithologies for three drill holes. White stars show the approximate depths that were sampled for this thesis.*

Mafic metavolcanic rocks are situated in the center and the northwest of the study area (Fig. 2.3). They are mainly fine- to medium-grained (less than 1 to 3 mm) and contain massive

and pillowed flows with minor pyroclastic rocks magnetite (Rogers and Berger, 1995). They are comparatively minor and were not intersected in drilling. The pillowed flows in the study area indicate submarine depositional environment (Rogers and Berger, 1995).

2.2.1) Close-up of Rockstone Drilling Lithologies

Although the initial goal of the exploration project was to identify potential Cu-Zn VMS deposits in the Rockstone property, a graphitic argillite unit approximately 28 m in apparent thickness was intersected by Greencastle Resources Ltd. during diamond drilling in 2012. Afterwards, in 2022, Deveron Resources Ltd. drilled again to replicate the values obtained in 2012 drilling and to get additional data about the graphitic zones. Information on the drill holes is as follows: DDH RS22-01, azimuth: 042.5 and dip: -45°, DDH RS22-03 is oriented in the same way as DDH RS22-01 and DDH RS22-04; however, the location is 50 m away to the south-east. The end of each hole is approximately 200 meters (Fig. 2.4). Representative photographs of drill cores, graphitic and sulfidic zones are shown Fig. 2.5.

Rockstone graphite is disseminated in argillite and intermediate tuff units (as in DDH RS22-01, RS22-03, RS22-04) and in brittle brecciated zones with massive sulfide mineralization (as in DDH RS22-04). Drill core logs by Clark Exploration Consulting of Thunder Bay, indicates that the Rockstone graphite is hosted chiefly by graphitic argillite, and it has a gradational contact with intermediate metavolcanic–volcaniclastic rocks such as intermediate to felsic tuff (Figs. 2.4). The graphitic argillite is dark grey to black, very fine-grained, with 70-90% graphite. Additionally, it does not contain massive graphite beds. In DDH RS22-01, ~5 m in core length graphitic argillite unit can be seen in ~40 m in core length intermediate tuff lithology, which contains graphite beds.

Figure 2.5: *Representative photographs of drill core from the Rockstone property; DDH RS22-04. NQ drill core: width = 5 cm. Graphitic intervals are shown by yellow markings and massive sulfide zone is shown by red markings.*

Graphitic argillite units are particularly notable in two zones in DDH RS22-03. The first one, ~10 m in core length, is nearer the top of the hole, overlain by felsic tuff and underlain by quartz porphyry. The second is further downhole, ~38 m in core length, overlain by intermediate volcanics and underlain by intermediate tuff unit, which is ~25 m in core length and contain ~ 6 meters graphitic argillite in it. Furthermore, in DDH RS22-04, ~12 m in core length graphitic argillite unit is overlain by ~ 2 m in core length massive sulfides and underlain by intermediate tuff unit (Fig. 2.4).

Graphitic brecciated zones are widely observed in DDH RS22-01. These zones contain milky grey quartz clasts (40-50 %, 3 mm to 5 cm in size), calcite (10-15 %) and pyrite veinlets (a few mm in width), disseminated pyrite (15-20 %) and graphite (15-20 %). However, some brecciated zones contain only quartz, calcite and sulfide minerals; they have a fracture-fill texture. A narrow-brecciated zone within the graphitic argillite unit contains quartz, calcite, and minor pyrite veins (DDH RS22-03). Graphite within the intermediate tuff unit occurs with very fine-grained and fracture-fill pyrite, blebby chalcopyrite and pyrrhotite and graphite and sulfides are in small bands along strong foliation of the rock (DDH RS22-03). Furthermore, sulfide minerals in the graphitic argillite zone comprise mainly disseminated banded and fracture-fill pyrite (20-40 %), fracture-fill and wispy chalcopyrite (10-15 %), and banded pyrrhotite (10-15%) with minor sphalerite (1-3 %). In graphitic argillite zones, minute graphite crystals are weakly to well foliated with fracture-fill and fine-grained pyrite, chalcopyrite, blebby and banded pyrrhotite and fracture-fill calcite (Cullen and Garry-Clark, 2014; Figs. 2.4 and 2.5).

In addition to the above-mentioned graphitic occurrences, massive sulfide mineralization was intersected immediately uphole from graphitic argillite in DDH RS22-04 (Fig. 2.4). The sulfidic unit is ~1.5 m in core length and contains mainly pyrite, sphalerite and chalcopyrite.

Overall, fine to coarse-grained pyrite, pyrrhotite, and minor sphalerite and chalcopyrite are associated with the graphite-rich unit and massive sulfide mineralization (Cullen and Garry-Clark, 2014). In all drill cores, intermediate volcanoclastic units were found at the bottom.

CHAPTER 3 – SAMPLING AND METHODS

3.1) Sampling and Sample Preparation

Thirty-two samples containing graphite and sulfide minerals (e.g., pyrite, pyrrhotite and sphalerite) were collected from three diamond drill cores, named RS22-01, RS22-03 and RS22-04, drilled by Deveron Resources Limited. Representative samples that showed the best graphitic and sulfidic zones and their relations in different intervals were selected for analysis. After sampling, the surfaces of the hand specimens were polished using 60-90, 320- and 600-grit carborundum powders at the Thin Section Laboratory, Department of Earth Sciences, University of Manitoba. Thirty-nine polished thin sections were produced from thirty-two hand specimens at the Thin Section Laboratory of the Department of Geology, Lakehead University, for further characterization.

Thin sections were polished with water using standard 400-1000 grit compounds with the final polish including 0.3-micron aluminum oxide. Before SEM-BSE (backscattered electron) imaging analyses, polished thin sections were cleaned with alcohol; carbon coating was omitted. For TEM analysis, the ion milling sample preparation technique was used. In this technique, a thin section is placed on resin and dissolved in acetone with the help of heat (Barber, 1981). The sample is then placed in an ion mill and bombarded with Ar^{+} ions, which makes it easier to thin the sample, making it very smooth and electron transparent. More importantly, this bombardment highlights very fine details in the internal structure of the sample for deeper analysis (Barber, 1993). If the material to be analyzed is polymineralic, it is difficult to thin the material. However, it is a suitable sample preparation method for single-component materials such as graphite (Lee, 2010). Sample thicknesses, which are generally less than 100 nm, may vary according to the TEM analyses planned to be performed (Lee, 2010; Kwiecinska et al.,

2019). Before EMPA (Electron Microprobe Analysis), polished thin sections were coated with carbon. Prior to SIMS analysis, the area of interest on thin sections were cut appropriately 2.5 cm in diameter circles and were cleaned with alcohol. The samples were then coated with a thin layer (~40 nm) of gold to provide the conductivity of the sample (Riciputi et al., 1998; Sheahan et al., 2016; Whattam et al., 2022).

3.2) Transmitted and Reflected Light Microscopy Analyses

Thirty-nine polished thin sections were examined and imaged at the Microbeam Laboratory, Department of Earth Sciences, University of Manitoba, using a Nikon Eclipse50/POL petrographic transmitted and reflected light microscope with a DS-Fi1 digital camera to characterize their mineral assemblages, textures and paragenetic sequences, alteration (e.g., chlorite, calcite, quartz) and sulfide minerals (e.g., pyrite, pyrrhotite, sphalerite). Areas of interest were marked for further analysis, described below.

3.3) Scanning Electron Microscopy (SEM) Analysis

After detailed petrographic examination, 16 thin-sections (RS22-01-4, RS22-01-5a, RS22-01-5b, RS22-01-6, RS22-01-7, RS22-03-3, RS22-03-4, RS22-03-7, RS22-03-8a, RS22-03-10, RS22-03-11, RS22-04-3, RS22-04-6, RS22-04-8, RS22-04-9a, and RS22-04-9b) were selected to be further characterized with an FEI Inspect S50 Scanning Electron Microscope with back-scattered electron and EDS X-ray detectors at the Microbeam Laboratory, Department of Earth Sciences, University of Manitoba. BSE imaging was performed with a low vacuum stage and an accelerating voltage of 15keV, using methods described by Cheng et al. (2015) and Kwiecinska et al. (2019).

In geology, scanning electron microscopy (SEM) is being widely used to determine the nature of grain boundaries by secondary electrons (SE), textural information with backscattered

electrons (BSE), and chemical compositions and elemental analysis (e.g., mapping) of minerals, using energy dispersive X-ray spectroscopy (EDS).

Scanning electron microscopy (SEM) of polished thin sections incorporates a backscattered electron imaging (BSE) technique that relies on atomic number contrast (Cheng et al., 2015). Backscattered electron works better on mineral phases containing elements with high atomic numbers, as opposed to graphite and similar mineral phases containing light elements such as carbon. The regions with heavy exhibit a brighter appearance (Barnes, 2003). These analyses were done to determine the nature of grain boundaries and textural information of graphite and minerals pertaining to graphite deposition such as coexisting sulfides and chlorite.

3.4) Electron Microprobe (EMP) Spectrometry Analysis

Chlorite and biotite in 11 thin sections (RS22-01-1, RS22-01-2, RS22-01-4, RS22-01-5a, RS22-01-5b, RS22-03-1, RS22-03-9b, RS22-04-8, RS22-04-9a, RS22-04-10, and RS22-04-12) was analyzed using a Cameca SX100 Electron Microprobe with WDS and EDS spectrometer at the Microbeam Laboratory, Department of Earth Sciences, University of Manitoba to establish the formation temperature of these minerals. Quantitative mineral chemistry analyses of chlorite and micas were carried out with a 15 kV acceleration voltage, a 20 nA beam current, a 10 μm beam size, a 20s peak counting times, and 20s background counting times. 2-29 Diopside (Si), 2-35 Pyrope (Al), 4-40 Rutile (Ti), 2-29 Diopside (Ca), 2-41 Olivine (Mg), 1-05 Albite (Na), 1-14 Fayalite (Fe), 2-31 Orthoclase (K), and 1-17 F-Riebeckite (F) were employed as standards.

3.5) Transmission Electron Microscopy (TEM) Analysis

Transmission electron microscopy (TEM) is an advanced microscopy technique that enables the acquisition of atomic-scale data by passing electron beams through specially prepared, very thin samples (Williams and Carter 1996). With TEM, magnifications of about

10,000,000x and resolutions of less than 0.1 nm, i.e., sub-angstrom scale (0.050 nm ultimate resolution for High-Resolution Transmission Electron Microscopy - HRTEM) can be achieved (Goldstein et al., 2007; O'Keefe, 2008; Muller, 2009; Williams and Carter, 1996). HRTEM allows direct examination of the atomic structure of a sample. This imaging technique is highly effective for investigations at the atomic scale. Advances in HRTEM have made it possible to reveal the evolution of mineral crystal lattices including crystal orientation and stacking disorder by analyzing their physical and chemical properties at the atomic level (Buseck, 1983). For instance, HRTEM enables precise observation of the graphene layers in graphite. Additionally, the dark-field imaging technique is used to enhance contrast by forming an image from electrons scattered at specific angles. Dark-field imaging highlights specific crystallographic orientations or defects on graphene layers, making features such as dislocations and stacking faults more visible. This method is particularly useful for studying structural inhomogeneities and distinguishing between different crystalline phases such as poorly and highly crystalline graphite (Williams and Carter, 1996). Like the preparation technique applied to other minerals, graphite samples used for TEM analyses are prepared very thin (generally < 100 nm) so that almost all electron beams can easily pass through the sample without scattering too much. Samples with this thin thickness are called 'electron transparent' (Williams and Carter, 1996; Lee, 2010). A carbon-free micro-Cu-grid was used to obtain the TEM images. This technique allows for characterizing the crystallinity of graphite and imaging of the d_{002} spacing, i.e., the distance between two graphene layers, and the nanotexture of graphene layers (Beyssac et al., 2002; Buseck and Beyssac 2014).

Using the High-Resolution Transmission Electron Microscopy (HRTEM) and dark-field imaging techniques, the crystal structures of three samples of the Rockstone graphite (RS22-01-

1a, RS22-01-4, RS22-04-9b) were measured at nanoscale using an FEI Talos F200X Transmission Electron Microscopy operating at 200kV at Manitoba Institute for Materials, University of Manitoba.

3.6) Raman Spectrometry Analysis

One of the most effective methods for studying carbonaceous materials, particularly carbon compounds like graphene and graphite, is Raman spectroscopy, because it enables analysis of microcrystalline graphite grains (Pasteris and Wopenka, 1991). Currently, a variety of studies have applied Raman spectroscopy to graphite to identify peak metamorphism temperature, crystal structure and thermal maturity of graphite (e.g., Buseck and Beyssac, 2014; Rantitsch et al., 2016; Parnell et al., 2021; Song et al., 2022; Al-Ani et al., 2022; Zhang et al., 2023; Hu et al., 2023; and Case et al., 2023). Raman study is a rapid, non-destructive, *in situ* technique that requires only a polished thin section. Raman analyses of five selected graphite samples (RS22-01-4, RS22-01-5a, RS22-01-5b, RS22-04-9a, and RS22-04-9b) were carried out by using a Horiba JobinYvon XPLORA confocal Raman spectroscopy interfaced with an Olympus BX41 microscope at the Harquail School of Earth Sciences, Laurentian University. The analytical protocol of Beyssac et al. (2002a, 2002b) was applied to these analyses.

3.7) Secondary-ion Mass Spectrometry (SIMS) Analysis

Based on petrographic observations, 5 samples (RS22-01-1a, RS22-01-4, RS22-01-5a, RS22-03-4 and RS22-04-12) were selected for carbon and sulfur isotope analyses. Carbon isotopes ($\delta^{13}C$) in graphite and sulfur isotopes ($\delta^{34}S$) in pyrite, sphalerite and pyrrhotite were measured, *in situ*, by a CAMECA 7f ion microprobe (secondary-ion mass spectrometry; SIMS) at the Manitoba Isotope Research Facility (MIRF), Department of Earth Sciences, University of Manitoba. Carbon and sulfur stable isotope ratios are reported in δ notation and presented

relative to Vienna Pee Dee Belemnite (VPDB, ‰) and Vienna Canyon Diablo Troilite (VCDT, ‰), respectively.

During SIMS measurement, a mass-dependent bias is introduced (Riciputi et al. 1998). The bias is strongly influenced by sample chemistry (i.e. matrix effects), therefore the instrument was calibrated by analyzing matrix matched reference material (RM). In house RM for graphite and sphalerite were used. For sphalerite, a suite of reference material (RM) with varying Fe content was used to produce calibration curves. The sphalerite RM consisted of multiple grains mounted in random orientations to account for any crystal orientation effects (Kita et al. 2010). Balmat pyrite and Anderson pyrrhotite were used as pyrite and pyrrhotite reference materials, respectively (Crowe and Vaugh, 1996). All uncertainties are reported at 1SD level with precisions of ~0.5‰ for C isotopes in graphite, 0.2‰ for S isotopes in pyrite and pyrrhotite, and 0.6‰ in sphalerite.

During analysis ~5 nA primary Cesium (Cs^+) ions were used to bombard the sample surfaces and accelerated at 10.0 kV. The beam size for graphite and sulfur minerals are ~25µm and ~10µm, respectively. A 200V sample offset was used to supress isobaric interference. Entrance slits were set to 225µm, the energy window was set at ±25V and a MRP of 350 was used. Each analysis consisted of 50 cycles, where one cycle consisted of 1 second and 5 seconds of counting on the major (i.e. ^{12}C & ^{32}S) and minor isotopes (i.e. ^{13}C & ^{34}S), respectively. An electron multiplier was used to detect ions with an overall deadtime of 25 ηs. An electron gun was used for charge compensation for sphalerite and graphite. Similar analytical protocol used from Riciputi et al. (1998), Sheahan et al. (2016) and references therein.

3.8) Isotope Ratio Mass Spectrometry (IRMS) Analysis

One graphite was analyzed via combustion in a Costech Elemental Analyzer, and three

calcite powder samples through acid digestion in a Gasbench II, both connected to a Delta V+ Isotope Ratio Mass Spectrometer (IRMS). For graphite samples, calibration was achieved by analyzing two internationally recognized reference materials, USGS40 and USGS41, at the beginning, middle, and end of each analytical run. To monitor analytical performance and ensure data quality, a sediment standard (B2151) with known isotopic composition was included and analyzed alongside the unknown samples. The calcite samples were dissolved in 100% phosphoric acid. Calibration was performed using two international calcite standards, NBS-18 and IAEA-603, also analyzed at the beginning, middle, and end of each run. Analytical precision and accuracy were monitored using an internal calibrated calcite standard, which was analyzed concurrently with the unknown samples. Calibration curves were generated via least-squares linear regression using the known and measured values of these standards of graphite and calcite samples.

To maximise analytical accuracy in IRMS, calibration standards are selected to closely match the chemical and physical matrix of the samples under investigation. This “matrix matching” approach reduces matrix-dependent fractionation effects and instrumental bias. Accordingly, carbonate standards were employed for the analysis of carbonate samples. As no graphite standard was available for comparison, the most effective alternative for high-carbon content analysis on the elemental analyser (EA) was selected. Based on prior performance evaluations, standard B2151, a high-organic sediment standard, was used for this purpose. Similar analytical protocol used from Sharpe (2013).

CHAPTER 4 – RESULTS

4.1) Macroscopic Description

Rockstone graphite is predominantly very fine- to fine-grained (up to 0.5 mm) as observed in drill cores RS22-01, RS22-03 and RS22-04 (Fig. 4.1). The host rocks in the Rockstone property are graphite-bearing, argillic metasedimentary and metavolcanic units composed mainly of silicates (e.g., quartz, mica, chlorite) and sulfides (e.g., pyrite and sphalerite). The host rocks are typically very fine- to fine-grained (<0.5 mm) and grey to dark grey in color due to the abundance of microcrystalline graphite and dark-colored silicates such as biotite. Graphite and micas both exhibit a black coloration, making it difficult to distinguish between them in hand specimens (Fig. 4.1). The host rocks exhibit a moderately developed foliation defined by aligned pyrite, quartz and biotite. Certain domains dominated by pyrite and pyrrhotite commonly exhibit flotation textures within the rock, occasionally accompanied by recrystallized pyrite grains (up to 1 cm; Fig. 4.1c).

The host rock is disrupted by brecciated zones and vein networks, where angular to rounded fragments are embedded in a fine-grained matrix, and cut by numerous fractures (Figs. 4.1a and 4.1b). These brecciated domains are characterized by quartz and calcite clasts, ranging up to 1 cm in size, which are angular to rounded and cemented by calcite veins with disseminated fine-grained pyrite (Fig. 4.1a). Microcrystalline graphite occurs as a disseminated crystals within the brecciated zones, in association with quartz, pyrite, sphalerite, and occasionally pyrrhotite (Fig. 4.1c). Graphite-rich veins appear dark and lack visible grain structure or layering. These veins are associated with silicates and aggregates of medium-grained pyrite and sphalerite (Fig. 4.1). Quartz and sulfides are intergrown with graphite, contributing to the definition of foliation within the rock (Fig. 4.1c). Pyrite, pyrrhotite, and sphalerite are the

primary sulfide minerals associated with the vein-hosted graphite (Fig. 4.1).

The host rocks are crosscut by thin veins of calcite, quartz, and sulfide (typically ranging from approximately 1 mm to 4 mm in thickness (Figs. 4.1a and 4.1c). These veins are generally narrow and irregular, locally exploiting foliation planes and fractures within the rock. In certain domains, very fine sulfide veinlets cut the graphite- and silicate-rich units (Fig. 4.1b), with individual sulfide veins measuring only a few millimeters in length. The transition between massive sulfide and graphite-rich zones is sharp (Fig. 4.1c).

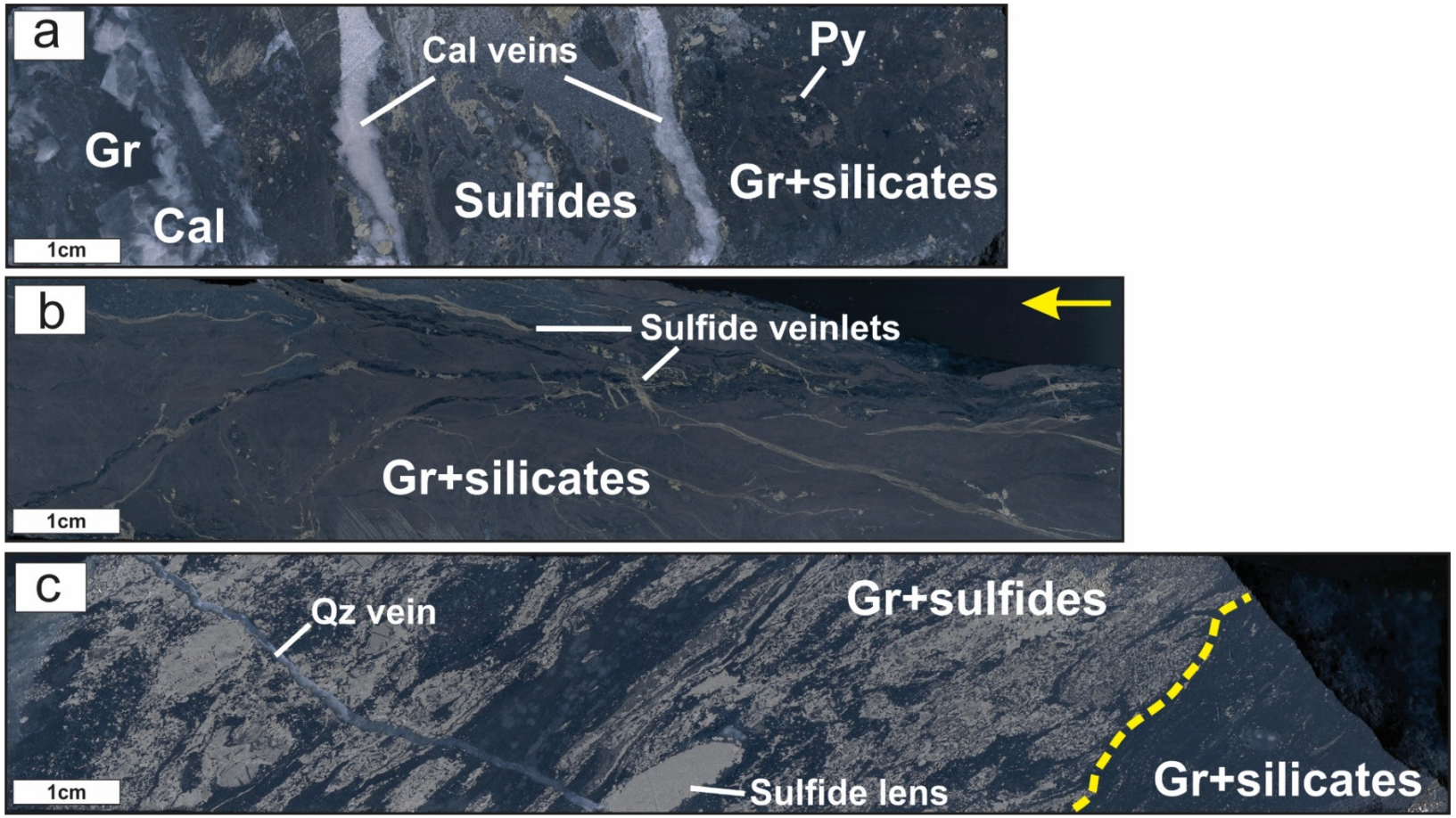

Figure 4.1: *Representative photographs of polished drill core predominantly composed of graphite, sulfides, and silicates. a) Brecciated calcite with calcite veins, disseminated pyrite, and graphite. b) Very fine-grained, massive graphite zone cut by pyrite veins. c) Quartz vein crosscutting all lithologies, incorporating graphite, sulfides, and silicates. The yellow dashed lines highlight graphite-sulfide contacts, while the yellow arrows indicate the top orientation of each drill core. Mineral abbreviations: Gr – graphite, Cal – calcite, Py – pyrite, Qz – quartz. In all figures, mineral abbreviations from Whitney and Evans (2010).*

4.2) Transmitted and Reflected Light Microscopy

Petrographic examination confirms that the Rockstone graphite occurs primarily in veins and/or brecciated zones as folded-deformed graphite flakes and aggregates of microcrystalline graphite (10-100 μm). In addition, scattered cryptocrystalline graphite grains (<10 μm) are identified within microcracks of the argillic host rock (Figs. 4.2-4.5).

4.2.1) Host Rock

The main minerals of the meta-volcano-sedimentary host rock are quartz (Qz), albite (Ab), chlorite (Chl), trioctahedral micas, muscovite (Ms), pyrite (Py), hornblende (Hbl) and a minor amount of epidote (Ep), sericite (Ser), calcite (Cal), sphalerite (Sp) and pyrrhotite (Po) (Fig. 4.2). In addition, titanite (Ttn), ilmenite (Ilm) and zircon (Zrn) are accessory minerals that are disseminated unevenly within the matrix. Characteristics of these minerals are described below.

Quartz (Qz) is the dominant mineral in all the studied thin sections: it constitutes modal ~50% of the rock. Quartz crystals (up to 0.1 mm) are anhedral, forming a recrystallized mosaic texture and mainly found in the matrix (Fig. 4.2). Albite (Ab; ~20%) is medium to coarse-grained (~0.2 to 0.5 mm) and is commonly twinned. Almost all albite is partially and/or completely sericitized (Figs. 4.2d and 4.2f). Brown and tabular, fine- to medium-grained (~0.2 to 0.4 mm) trioctahedral mica grains, comprise ~15% of the rock, is evenly distributed and defines the dominant fabric in the host rock (Figs. 4.2c). Disseminated, very fine- to fine-grained (up to 0.4 mm) trioctahedral crystals are subhedral to anhedral, similar to muscovite (Ms; ~0.1 to 0.4 mm). Trioctahedral micas and muscovite comprise ~10% of the rock (Fig. 4.2). Pale green chlorite (Chl), ~10% of the rock, varies in grain size from 0.5 to 1 mm, primarily occurs as elongated and platy aggregates, is intergrown with other minerals such as trioctahedral mica,

hornblende (Hbl), and pyrite (Py) (Figs. 4.2a and 4.2c). Hornblende and epidote (Ep) constitute ~5% of the host rock.

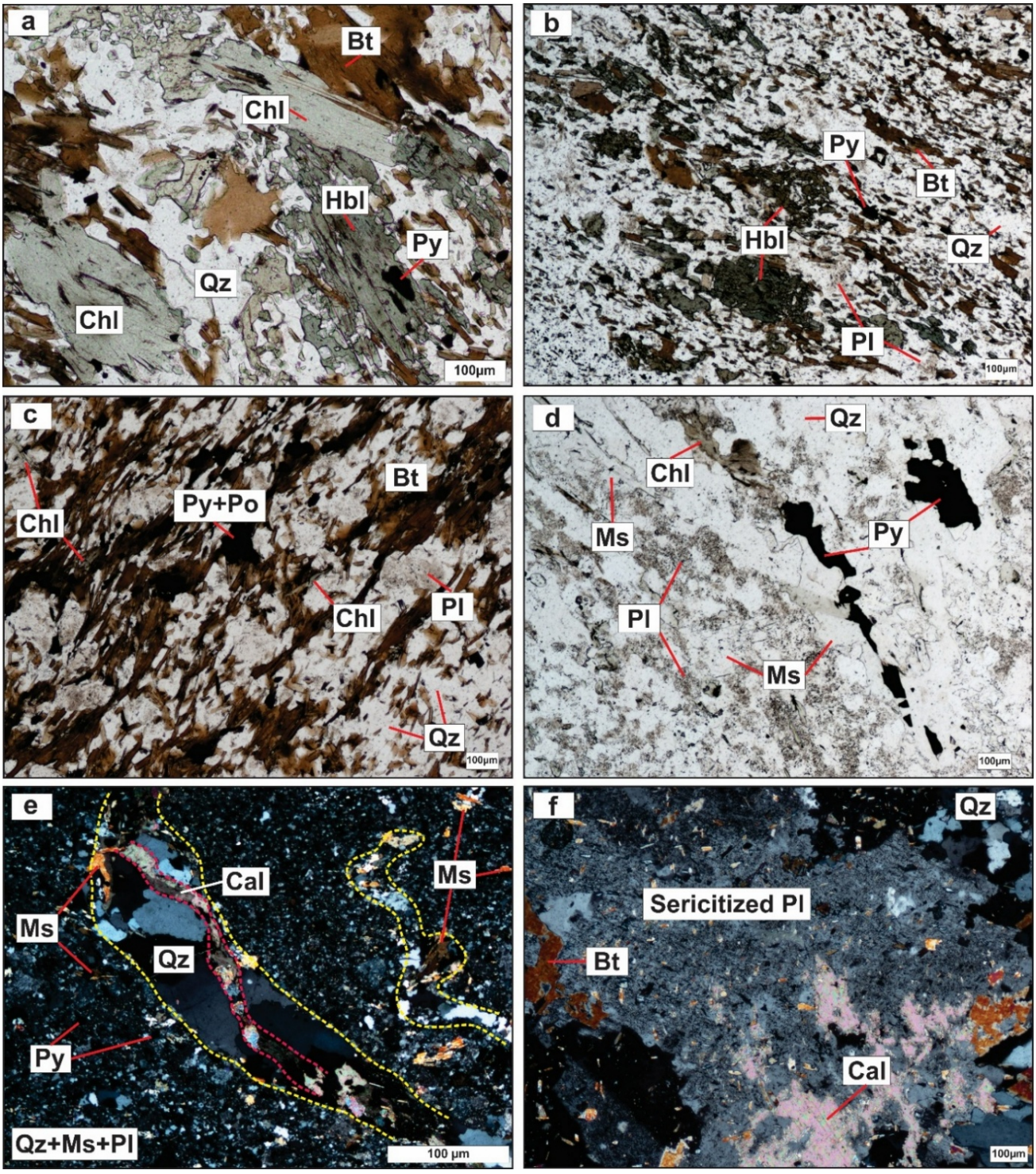

Figure 4.2: *Transmitted light photomicrographs of fine-grained volcano-sedimentary host rock (a-d: plane-polarized light (PPL); e-f: cross-polarized light (XPL)): (a) Biotite, pale green chlorite, and hornblende, accompanied by plagioclase and quartz, with minor amounts of pyrite. (b) Fine-grained biotite and hornblende defining the foliation of the rock. (c) Foliation defined by biotite, pyrrhotite, pyrite, quartz, and plagioclase, with minor chlorite present. (d) Muscovite, plagioclase partially altered to "dusty" sericite, and quartz, along with minor chlorite and pyrite. (e) Coarse-grained quartz, calcite, and muscovite-bearing veins cutting through a recrystallized matrix of quartz, muscovite, and plagioclase. Notably, calcite veins postdate the generation of quartz veins. These veins represent microfractures within the host rock. (f) Sericitized plagioclase and quartz, along with calcite and biotite. Mineral abbreviations: Bt – biotite, Chl – chlorite, Hbl – hornblende, Py – pyrite, Qz – quartz, Pl – plagioclase, Po – pyrrhotite, Ms – muscovite, Cal – calcite.*

Dark green hornblende (~0.3-0.5 mm) is subhedral to anhedral and scattered throughout the rock (Figs. 4.2a and 4.2b). Epidote is found as anhedral grains, varying in size from 0.1 to 0.2 mm, and as aggregates in the host rock. Accessory minerals (e.g., titanite, ilmenite, rutile and zircon) constitute modal <1% of the rock and <0.1 mm in size. These are disseminated within the host rock and predominantly occur in subhedral form.

The host rock is cut by narrow (<100 μm wide) veins of quartz and calcite, which also contain dispersed to locally concentrated graphite particles (<10 μm in size) are unevenly dispersed (Figs. 4.2e and 4.7a). Graphite (Gr) is also present as small black fragments within the matrix of the host rock.

4.2.2) Veins

Veins within the rock can be classified into two primary groups (Figs. 4.3-4.5). The first group, representing an early generation of veins, is predominantly composed of graphite. In contrast, the second group, representing a later generation, consists of quartz, calcite, and pyrite that cut both the host rock and the earlier graphite-rich veins (Fig. 4.6). Petrographic analysis supports the macroscopic observations, confirming that graphite is primarily concentrated within the early-generation veins (Figs. 4.3-4.5).

The mineralogy of the first-generation veins is dominated by graphite, chlorite, quartz, pyrite, sphalerite, and pyrrhotite, with minor amounts of muscovite, calcite, pyrrhotite and chalcopyrite (Ccp). Additionally, trace amounts of albite, trioctahedral mica, galena (Gn), molybdenite (Mol), titanite, rutile (Rt), and apatite (Ap) are present (Figs. 4.3-4.5). The average width of these early vein formations ranges from approximately 100 to 300 μm (Figs. 4.3 and 4.4). These veins are primarily characterized by very fine- to fine-grained graphite (~45%; 40–100 μm), anhedral dark green chlorite (~15%, <100 μm), fine- to medium-grained quartz (~10%; 100–500 μm), subhedral fine-grained albite (<5%; up to 100 μm), and anhedral to subhedral pyrite and sphalerite (~15%, 100 to 300 μm; Figs. 4.3-4.5). Very fine- to fine-grained tabular muscovite (~5%, <100 μm) and trioctahedral mica (<5%, <100 μm) are present in these veins (Fig. 4.5). Furthermore, dark green chlorite exhibits a flow texture and predominantly surrounds the crystal boundaries of graphite, pyrite, and sphalerite (Fig. 4.4). Pyrite (0.1 to 0.3 mm) occurs as subhedral to anhedral grains within the veins and is intergrown with graphite flakes (Figs. 4.3b, 4.4a, and 4.5). Moreover, pyrite occasionally displays anhedral forms and occurs as a fracture-fill, often accompanied by subhedral pyrite crystals (Figs. 4.3b and 4.3d). Sphalerite and pyrrhotite are generally anhedral to subhedral, up to 1 mm, and are interstitial to graphite (Fig. 4.3c). Fine-grained chalcopyrite, galena and molybdenite (<0.1 mm) occur in in trace amounts (Figs. 4.4d and 4.9d).

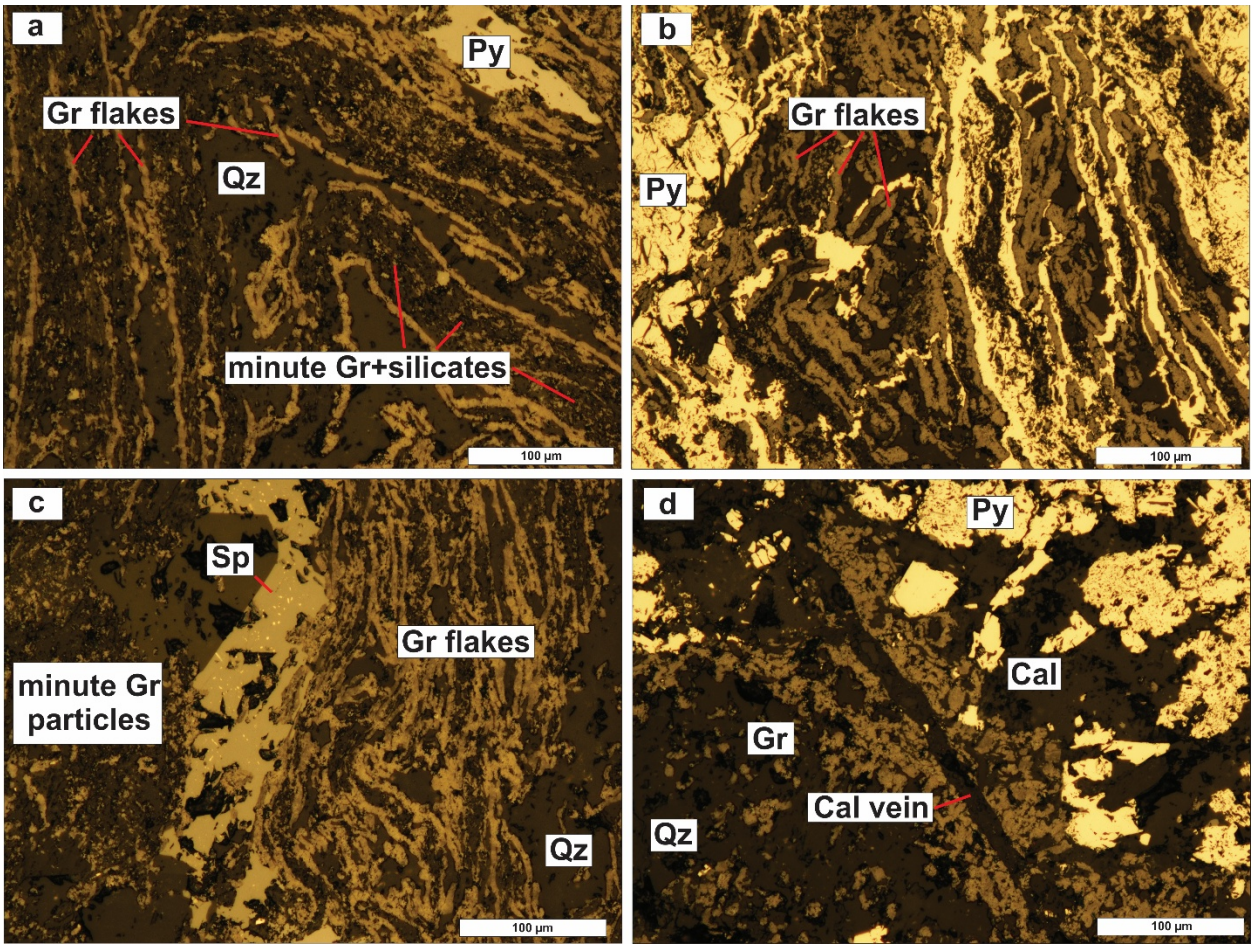

Figure 4.3: *Reflected light photomicrographs illustrating vein-hosted graphite textures and mineral associations. (a) Folded brown-grey to yellow-brown graphite flakes within a quartz matrix. Note the presence of minute graphite crystals and quartz grains situated between two folded graphite flakes. (b) Graphite flakes spatially associated with pyrite. (c) Microcrystalline graphite fragments within a quartz matrix (left), with graphite flakes intergrown with sphalerite and chalcopyrite. (d) Graphite- and calcite-filled veins containing disseminated pyrite crystals. Mineral abbreviations: Gr – graphite, Qz – quartz, Py – pyrite, Sp – sphalerite, Cal – calcite.*

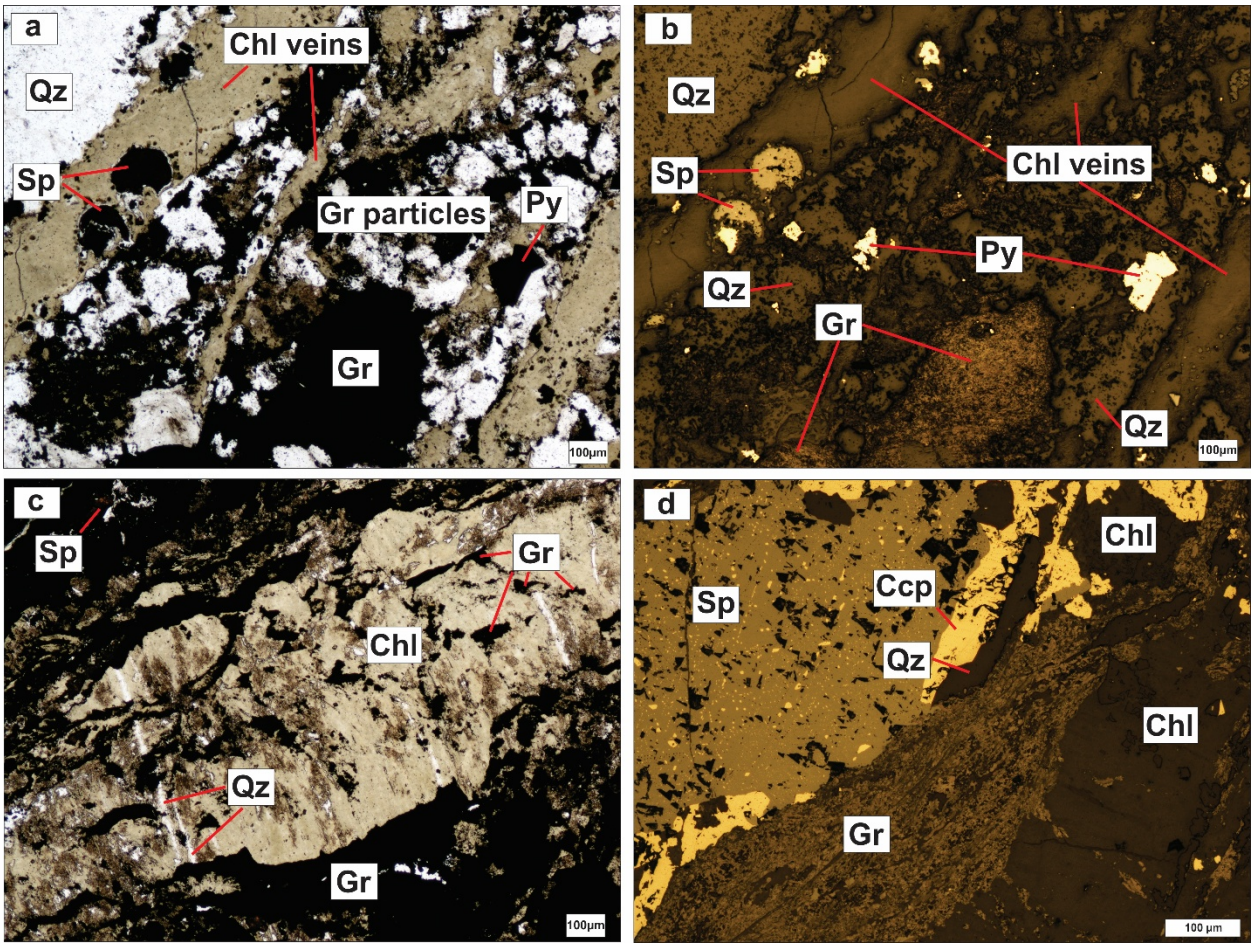

Figure 4.4: *Transmitted light (a, c) and reflected light (b, d) photomicrographs of vein-hosted graphite and associated mineral assemblages. (a) Dark green chlorite veins associated with brecciated and disseminated graphite fragments, pyrite, and sphalerite within a quartz matrix. (b) The RL image corresponding to (a), emphasizing the same mineral associations. (c) Chlorite and graphite veins bordered by sphalerite and chalcopyrite, with narrow, vertically oriented quartz veins. (d) Graphite in a chlorite vein, associated with sphalerite, chalcopyrite, and quartz. Mineral abbreviations: Qz – quartz, Sp – sphalerite, Py – pyrite, Chl – chlorite, Gr – graphite, Ccp – chalcopyrite.*

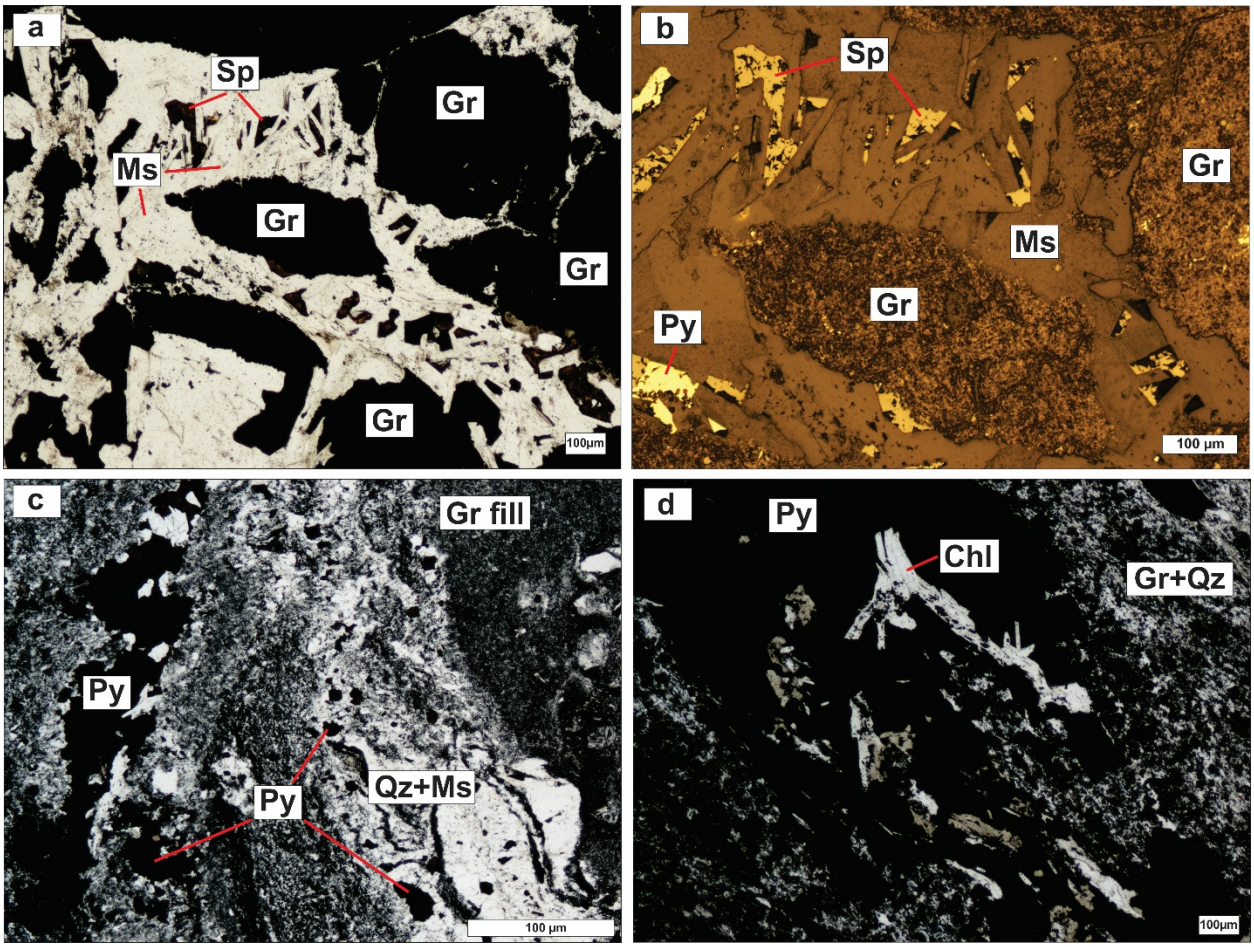

Figure 4.5: *Transmitted light (a, c, d) and reflected light (b) photomicrographs of vein-hosted graphite and associated mineral assemblages. (a) Microcrystalline brecciated graphite aggregates surrounded by muscovite and sphalerite (b) Magnified view of (a), showing the close association of graphite aggregates with muscovite, sphalerite and pyrite. (c) and (d) Intergrowths of microcrystalline graphite with quartz, chlorite, muscovite, and pyrite. Mineral abbreviations: Gr – graphite, Ms – muscovite, Sp – sphalerite, Py – pyrite, Qz – quartz, Chl – chlorite.*

Very fine-grained graphite flakes (~60%) define a strong foliation in certain areas in the veins and are texturally associated with chlorite, quartz, plagioclase, muscovite, pyrite and sphalerite (Figs. 4.3 and 4.5). Furthermore, the fabric is also defined by alternating layers of microcrystalline graphite, quartz and muscovite (Fig. 4.5c and 4.5d). Graphite is generally found as folded flakes and aggregates (clusters of fragments) within the veins and occasionally tends to concentrate along the vein walls (Figs. 4.3, 4.4, and 4.5). In certain areas of the rock, muscovite

crystals surround graphite aggregates in association with sphalerite (Fig. 4.5a). Throughout the veins, graphite occurs as very fine to fine-grained crystals, primarily ranging from 40 to 100 μm in length (Figs. 4.5a and 4.5c). Moreover, in certain areas of the veins, graphite crystals within the quartz matrix are generally smaller than 20 μm in length (Fig. 4.5d).

A network of pyrite + quartz + calcite veins represent the last stages of hydrothermal activity in the area as they cut both the graphite-rich veins and the host rock (Figs. 4.3d and 4.6). These late-stage veins are fine- to coarse-grained, with crystals varying from 10 to 200 μm in size (Fig. 4.6).

Overall, fine- to very fine-grained graphite flakes and particles are generally difficult to detect using traditional reflected light microscopy. Microcrystalline graphite flakes occurring within the veins typically range in length from 10 to 100 μm. In the host rock, a weak foliation is manifested by the alignment of quartz, trioctahedral micas, and sulfide layers (Fig. 4.2c). Conversely, in certain areas of the first vein generation, the graphite foliation is crenulated with quartz, chlorite, and minor sulfide minerals (e.g., pyrite and sphalerite) and concentrated in the fold hinges with micas (Fig. 4.3a). Taken together, Rockstone graphite occurs both as minute, unevenly distributed cryptocrystalline grains within the fractures of the host rock and as folded, flaky crystals and brecciated aggregates within veins.

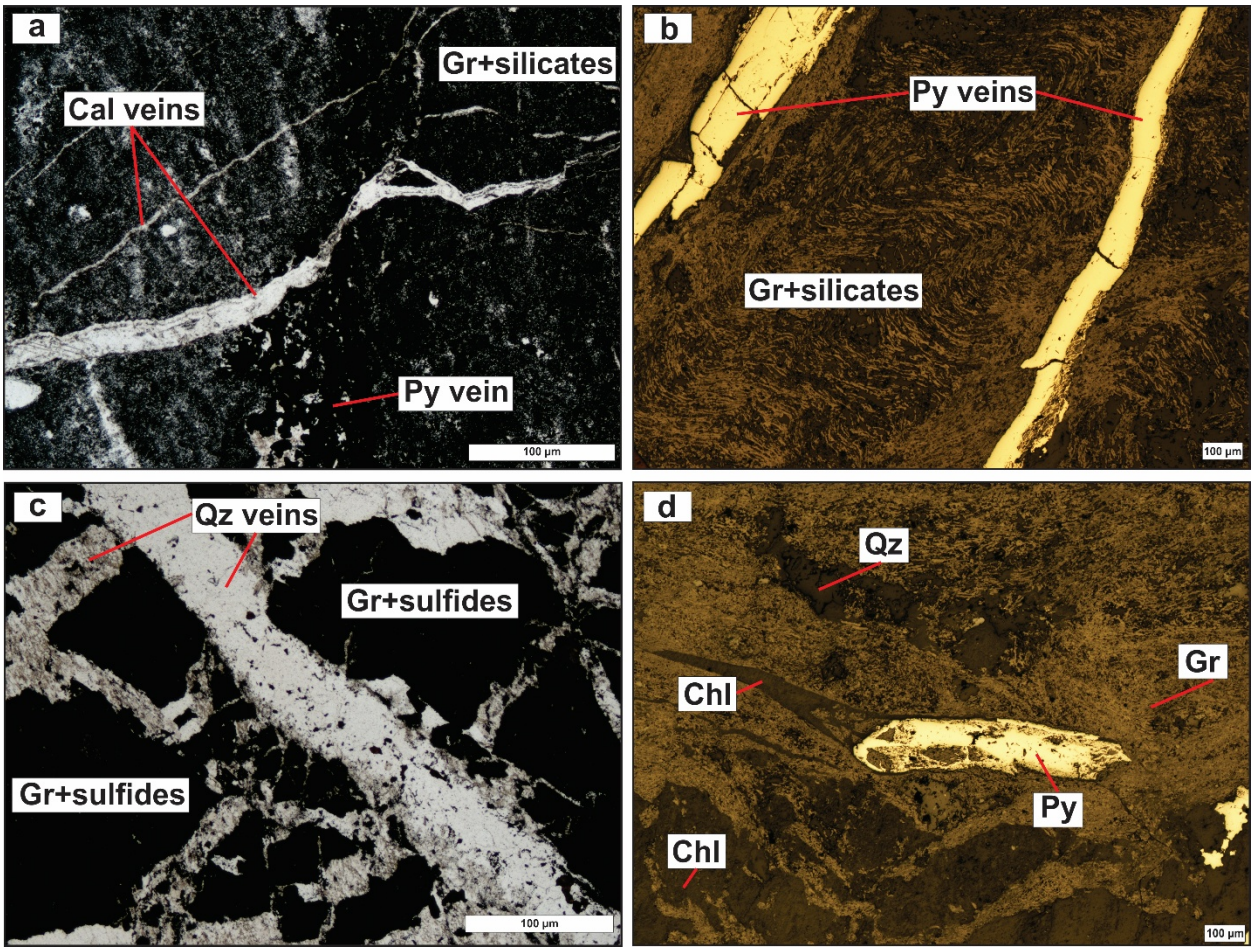

Figure 4.6: *Transmitted light (a, c) and reflected light (b, d) photomicrographs illustrating second generation of veins affecting vein-hosted mineral assemblages. (a) Calcite veins overprinting earlier quartz, chlorite, mica, pyrite and graphite. (b) Pyrite veins crosscutting folded graphite, indicating a later mineralization phase. (c) Coarse- to fine-grained quartz veins overprinting graphite, pyrite, and sphalerite. (d) Graphite and chlorite veins altering a pre-existing pyrite crystal. Mineral abbreviations: Gr – graphite, Py – pyrite, Cal – calcite, Qz – quartz, Chl – chlorite.*

4.3) SEM Results

Back scatter electron (BSE) images were collected to determine the textural relations, graphite flake sizes and paragenesis of graphite and associated minerals. A detailed SEM investigation reveals that graphite occurs as very fine-(<10 µm) to fine-grained flakes (10-100 µm), which are sometimes unevenly distributed within microfractures of the host rock and

appear folded or clustered into nodule-like aggregates within the veins (Figs. 4.7-4.9).

In the host rock, graphite particles are rare, cryptocrystalline (<10 μm), unevenly scattered (Fig. 4.7a) and associated with quartz, trioctahedral mica, pyrite and pyrrhotite. In addition, graphite is seen to be associated with fine-grained anhedral calcite and ilmenite (Fig. 4.7a).

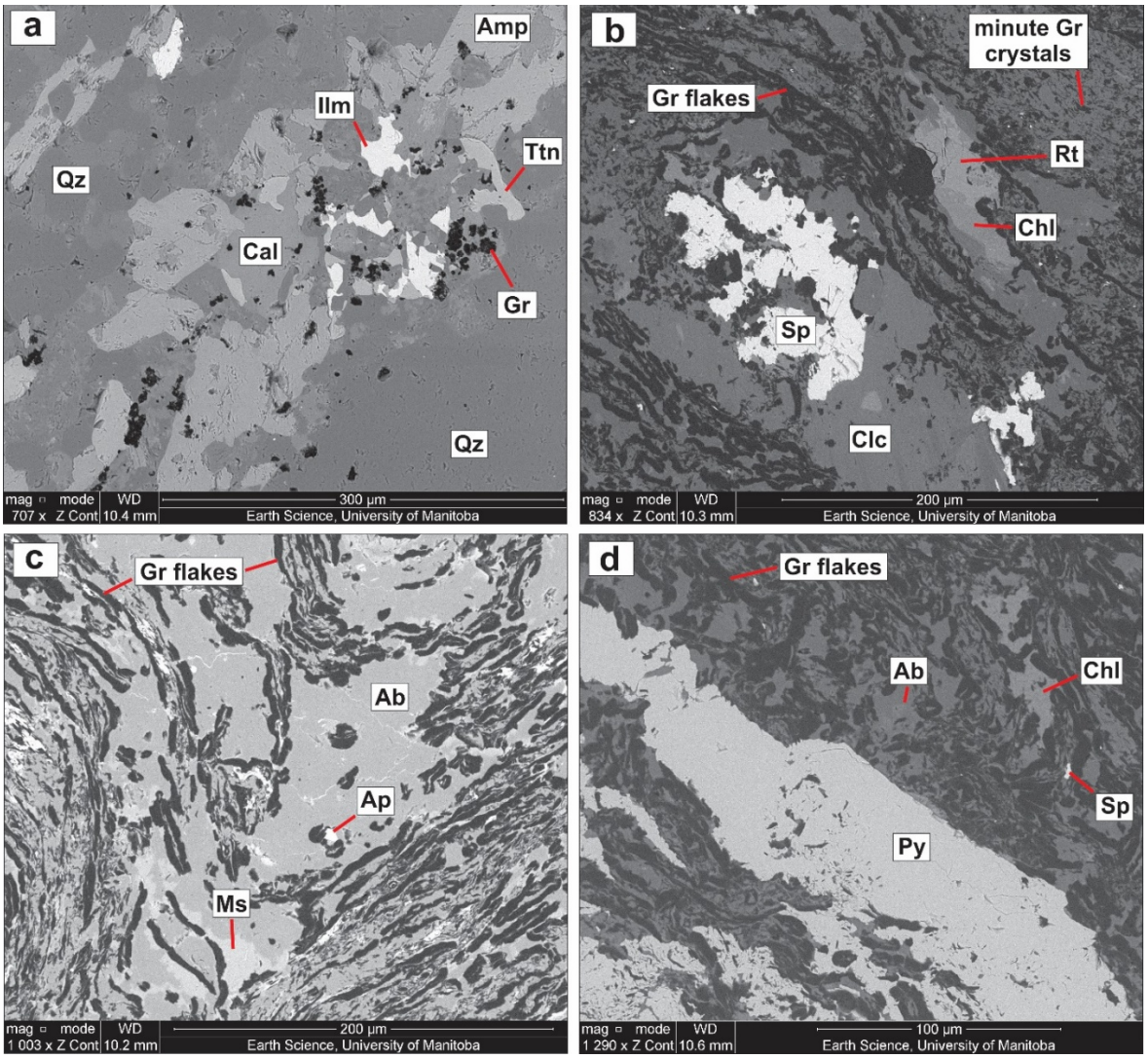

Figure 4.7: *Back scatter electron (BSE) images of graphite-bearing zones and associated mineral assemblages. (a) Microfracture of the host rock infilled with minute grains of graphite in association with titanium-bearing minerals, calcite, and silicates. (b) Vein-hosted graphite aligned with chlorite and spatially associated with sphalerite. (c) Folded graphite flakes intergrown with muscovite and albite; apatite in the center of the image is surrounded by fine graphite grains. (d) Coarse-grained pyrite closely associated with graphite flakes. Chlorite, albite, and minor sphalerite are also present in association with graphite.*

Mineral abbreviations: Ab – albite, Amp – amphibole, Ap – apatite, Cal – calcite, Chl – chlorite, Clc – clinochlore, Gr – graphite, Ilm – ilmenite, Ms – muscovite, Py – pyrite, Rt – rutile, Sp – sphalerite, Ttn – titanite, Qz – quartz.

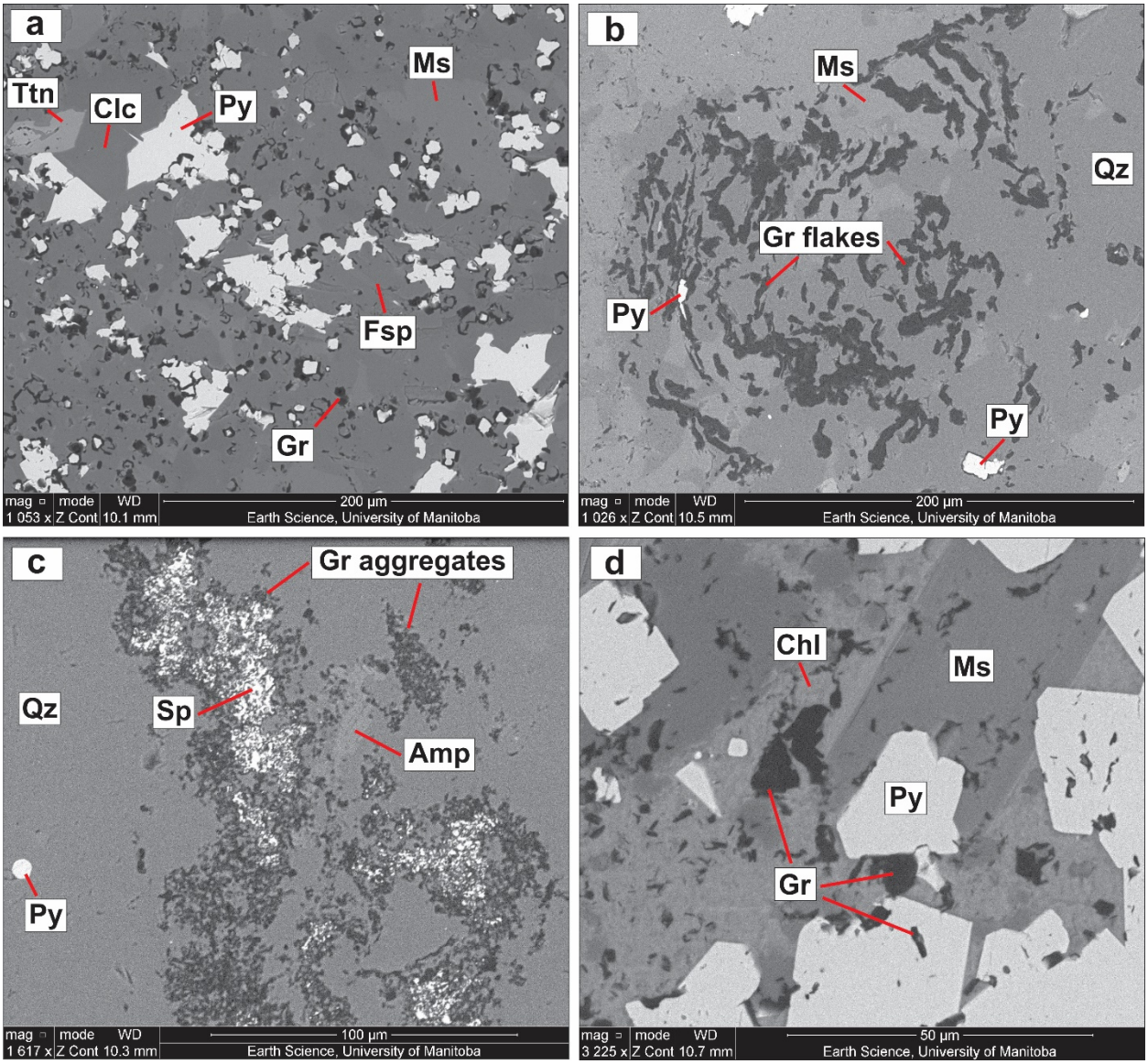

Figure 4.8: *Back scatter electron (BSE) images of vein-hosted graphite and associated sulfide-silicate mineral assemblages. (a) Disseminated minute graphite grains, predominantly associated with anhedral pyrite crystals. Note the presence of oblong-shaped graphite flakes within the silicate matrix. (b) Clustered graphite flakes with minor pyrite hosted in a quartz matrix. (c) Microcrystalline graphite grains in close association with sphalerite. (d) Euhedral to subhedral pyrite grains accompanied by disseminated graphite. Graphite occurs both within the silicate matrix (chlorite and muscovite) and as inclusions within individual pyrite crystals. Mineral abbreviations: Amp – amphibole, Cal – calcite, Clc – clinochlore, Gr – graphite, Ms – muscovite, Py – pyrite, Sp – sphalerite, Ttn – titanite, Qz – quartz.*

In the veins, graphite flakes are folded and primarily seen together with silicates (e.g., chlorite, quartz, albite and muscovite) and sulfide minerals (e.g., pyrite and sphalerite) (Figs. 4.7-4.9). In some parts, coarser grained pyrite veins cut graphite (Fig. 4.7d). Very fine-grained apatite (<10 μm) surrounded by minute graphite flakes is also detected (Fig. 4.7c). Titanium-bearing phases (e.g., rutile and titanite) are associated with graphite flakes (Figs. 4.7b and 4.8a). Pyrite and sphalerite are the sulfide minerals that are intimately associated with minute graphite aggregates and folded-flake graphite grains in the veins (Fig. 4.8). Graphite crystals are intergrown with or surrounded by chlorite and sulfides (Fig. 4.9). Some silicate minerals, including trioctahedral micas, muscovite, and albite, are aligned parallel to the foliation, commonly occurring alongside coarse-grained pyrite and fine-grained graphite (Fig. 4.9a).

Microcrystalline graphite particles are present within quartz in the matrix. Furthermore, in certain areas, there are minute graphite and pyrite together within the muscovite-rich matrix. Coarse-grained anhedral pyrite commonly hosts inclusions of albite and graphite (Fig. 4.9b). Within the vein zones, graphite flakes are locally aligned parallel to chlorite, mainly clinochlore, and other silicates such as quartz, albite, and muscovite (Fig. 4.9c). In addition to all, molybdenite is the rarest sulfide mineral that is surrounded by graphite flakes in the veins (Fig. 4.9d).

Overall, cryptocrystalline (typically <10 μm) are hosted as micro-veins of argillic host rock. In contrast, graphite crystals occur in the veins and generally range from 10 to 80 μm in length, with an average length of approximately 35 μm (Figs. 4.7-4.9). Notably, variations in graphite grain size and distribution are observed even over small areas (Figs. 4.7b and 4.9b).

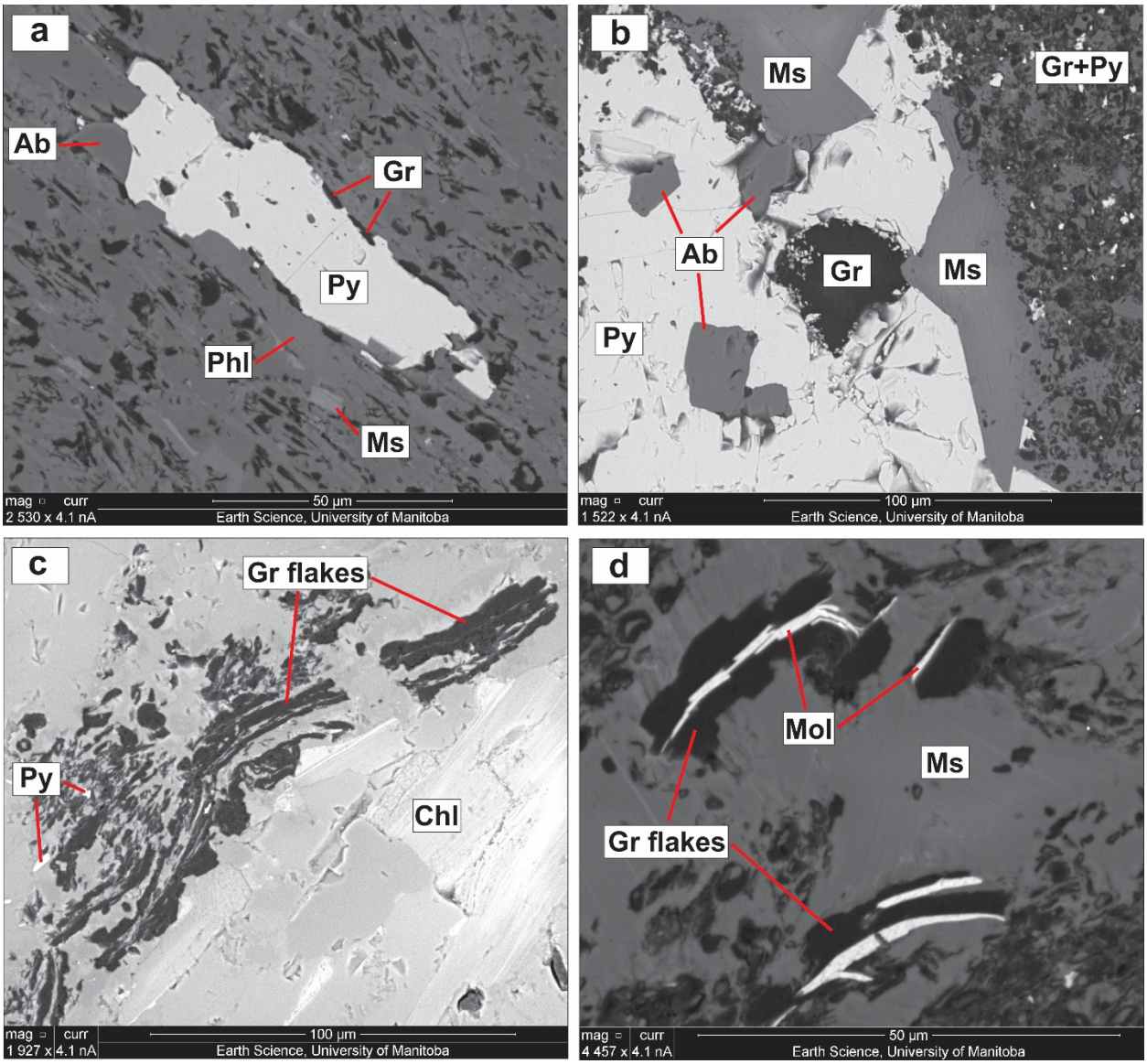

Figure 4.9: *Back scatter electron (BSE) images of vein-hosted graphite and associated mineral phases. (a) Pyrite crystal rimmed by minute graphite flakes; additional graphite is dispersed within the surrounding matrix. (b) Graphite grains of variable sizes occurring alongside pyrite, muscovite, and albite. Note the presence of albite inclusions within the pyrite crystal. (c) Graphite flakes and chlorite intergrown with fine-grained pyrite. (d) Molybdenite surrounded by graphite flakes hosted within a muscovite-rich matrix. Mineral abbreviations: Ab – albite, Chl – chlorite, Gr – graphite, Mol – molybdenite, Ms – muscovite, Phl – phlogopite, Py – Pyrite.*

4.4) Mineral Paragenesis

The study area comprises a metasedimentary and metavolcanic unit that exhibit mineral assemblages reflecting greenschist-amphibolite facies metamorphism and differences in bulk composition. Both rock-types are overprinted by veins; the first generation of veins is dominantly characterized by graphite, pyrite and sphalerite and is interpreted as syn-deformational while the second, post deformation, generation is characterized by quartz, calcite, and pyrite (Table 4.1).

The primary, depositional/volcanic mineral assemblage of the host rocks is not preserved. The regional metamorphic assemblage of the host rocks consists of quartz, albite, trioctahedral mica, pyrite along with hornblende. Minor constituents include epidote and pyrite, while trace amounts of titanium-bearing minerals such as ilmenite and titanite are also present (Table 4.1). Metamorphic overprinting has led to the chloritization of biotite, sericitization of albite, and recrystallization of quartz. Recrystallized pyrite, sphalerite and pyrrhotite are also present. Calcite patches in the host rock is most likely an alteration product derived from calcium-rich plagioclase. Primary mineral assemblage of the host rocks developed prior to metamorphic overprinting, along with the occurrence of fractured zones.

The first vein generation is primarily composed of graphite, chlorite, quartz, muscovite, calcite, albite with lesser amount trioctahedral mica and a range of sulfide minerals (i.e., pyrite, pyrrhotite, sphalerite, chalcopyrite, galena and molybdenite), along with accessory phases such as titanite, rutile, and apatite (Table 4.1). A subsequent vein generation (late overprint stage), characterized by quartz, pyrite, and calcite, crosscuts both the host rock and earlier graphite-bearing structures. In certain sections, pyrite appears to be overprinted by graphite (Fig. 4.6d; Table 4.1).

Table 4.1: *Mineral paragenesis of the Rockstone mineralization based on petrographic investigations.*

Protolith (Sedimentary)		
Mineral	**Host Rock**	**Prograde to Retrograde Metamorphism**
Quartz		
Albite		
Recrystallized Quartz		
Sericitized Albite		
Trioctahedral Mica		
Muscovite		
Chlorite		
Calcite		
Pyrite		
Pyrrhotite		
Ilmenite		
Titanite		
Protolith (Volcanic)		
Quartz		
Albite		
Recrystallized Quartz		
Sericitized Albite		
Trioctahedral Mica		
Chlorite		
Hornblende		
Epidote		
Calcite		
Pyrite		
Sphalerite		
Pyrrhotite		
Ilmenite		
Titanite		
major,	minor,	rare

Table 4.1: *(continued).*

	Vein Generations	
Mineral	**Deformational**	**Late Overprint**
Quartz	major	major
Chlorite	major	
Muscovite	minor	
Albite	rare	
Trioctahedral Mica	rare	
Calcite	minor	major
Graphite	major	
Pyrite	major	major
Sphalerite	major	
Pyrrhotite	minor	
Chalcopyrite	minor	
Galena	rare	
Molybdenite	rare	
Titanite	rare	
Rutile	rare	
Apatite	rare	

major, minor, rare

Aside from vein-hosted occurrences, the presence of graphite within the host rock remains uncertain, as it has not been conclusively identified due to its extremely fine-grained nature—often less than 10 microns in size. Nonetheless, minute graphite crystals may be present, locally associated with calcite and Ti-bearing minerals (e.g., ilmenite and titanite) within micro-veins of the host rock.

4.5) TEM Results

High resolution transmission electron microscopy (HR-TEM) and scanning transmission electron microscopy (STEM) images provide detailed structural and chemical information of the Rockstone graphite at the nanoscale. The former method provides the visualization of graphene layers (lattice fringes), orientations and defects in the crystal structure, whereas the latter provides 3-D images using the high-angle annular dark-field (HAADF) detector on the morphology of graphite grains (Figs. 4.10-4.12).

Long-range order of graphene layers (ordering to disordering crystalline characteristics) can be seen in Rockstone vein-hosted graphite (as demonstrated in A. Conly's previous XRD studies, personal communication, 2025). In the veins, poorly crystalline graphite is characterized by the presence of dislocations in folded and brecciated graphene layers (Figs. 4.10-4.12). Ordered, highly crystalline graphite, indicative of sharp diffraction spots following hexagonal symmetry in SAED pattern, is rare but can occur in subdomains especially in graphite fragments with calcite fillings (Fig. 4.10d). Disordered, poorly crystalline graphite, on the other hand, is depicted by ambiguous and diffused diffraction spots in SAED patterns and seen is in many subdomains (Figs. 4.10-4.12). For example, in vein-hosted graphite, graphene layers are associated with stacking defects (Fig. 4.10), which produce smeared diffraction spots in SAED patterns (Figs. 4.10b and 4.10f). Additionally, folded flaky grains exhibit distorted features, including changes in orientation likely resulting from shearing and/or deformation, as well as bending of the graphene sheets. (Figs. 4.11b, 4.11c, 4.11d and 4.11e). Lattice defects also occur in brecciated graphite aggregates (Fig. 4.12), which can be recognized on the morphology of the lattice fringes in HR-TEM images (e.g., distortion and bending in graphene layers) and on smeared diffraction spots in SAED patterns (Figs. 4.12b and 4.12c).

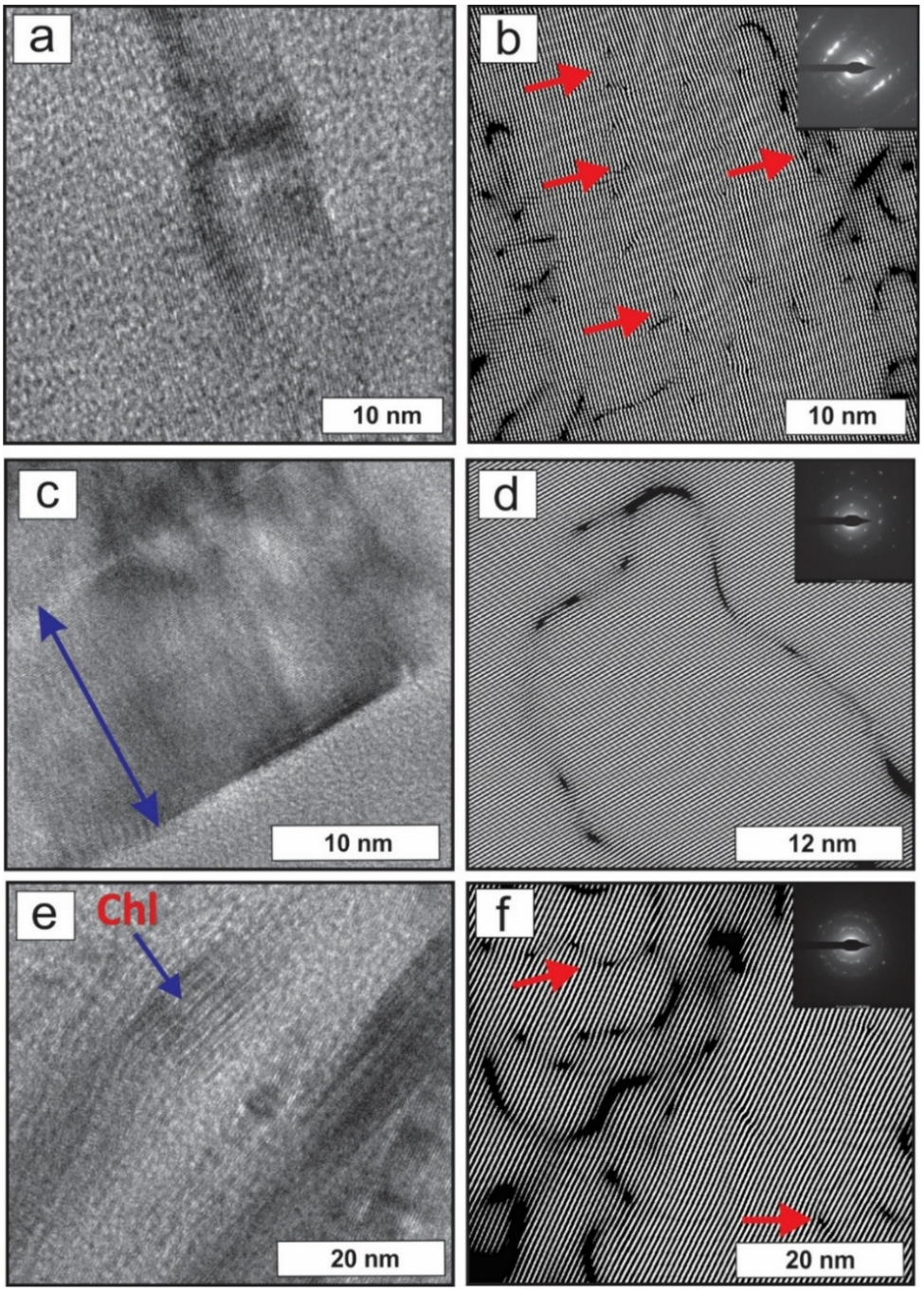

Figure 4.10: *Transmission electron microscopy (TEM) images of vein-hosted graphite (sample RS22-01-1a). (a), (c), and (e) show high-resolution TEM (HRTEM) images illustrating the lattice fringes of the graphite. Corresponding noise-filtered images and selected area electron diffraction (SAED) patterns are displayed in (b), (d), and (f), respectively. These images reveal both ordered (hexagonal) and disordered atomic arrangements within the graphene layers. Crystalline defects are indicated by red arrows, while blue arrows in (c) denote stacked graphene layers.*

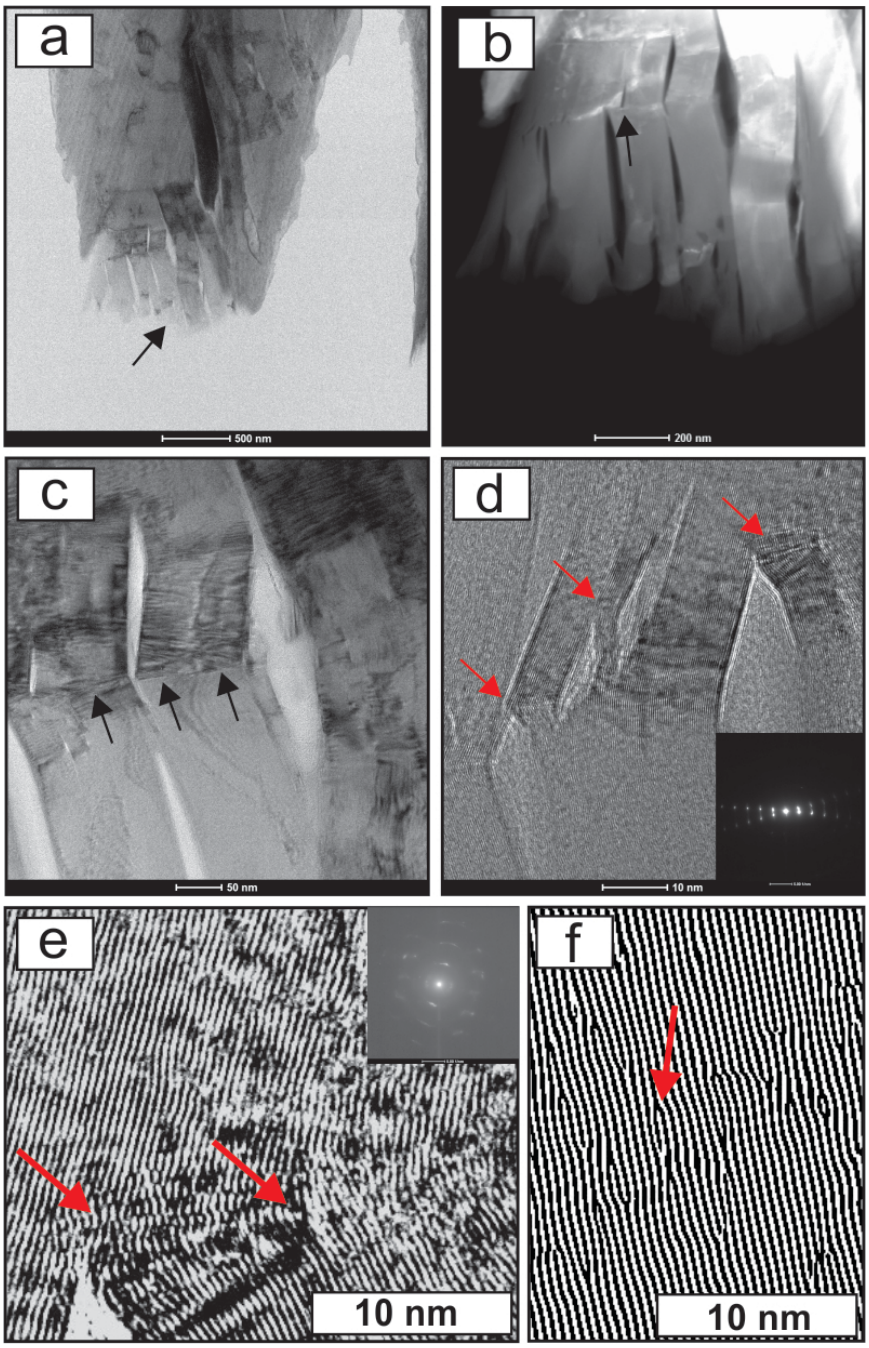

Figure 4.11: *Transmission electron microscopy (TEM) images of vein-hosted folded flaky graphite (sample RS22-01-4). (a) and (b) display scanning transmission electron microscopy (STEM) images illustrating folded and deformed graphite flakes. High-resolution TEM (HRTEM) images of the lattice fringes of flaky graphite grains are shown in images (c) and (d), alongside selected area electron diffraction (SAED) patterns indicating two distinct orientations of the graphene layers. (e) and (f) present noise-filtered images and corresponding SAED patterns, highlighting distortions and bending features within the graphene stacks, as indicated by the arrows.*

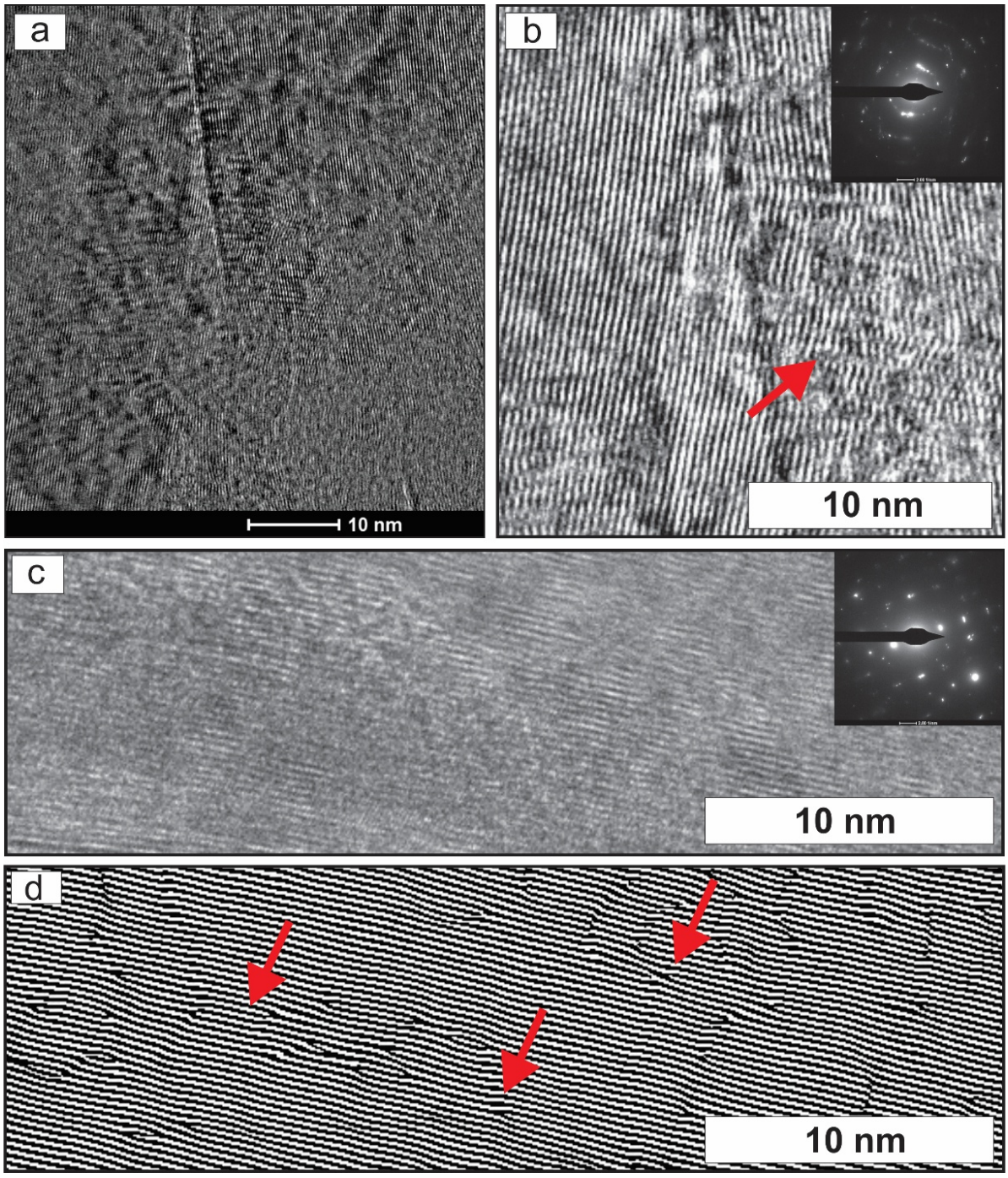

Figure 4.12: *Transmission electron microscopy (TEM) images of brecciated graphite fragments (sample RS22-04-9b), along with selected area electron diffraction (SAED) patterns illustrating disordered atomic arrangements within the graphene layers. (a) and (c) show high-resolution TEM (HRTEM) images of the lattice fringes in graphite grains, while (b) and (d) display noise-filtered images of the graphene layers. Red arrows indicate distortions, primarily associated with dislocations in the graphene stacks.*

4.6) Host Rock and Vein-hosted Chlorite Mineral Chemistry

The chemical composition of host rock and vein-hosted chlorite intimately associated with graphite, as deduced from textural relationships, was used to calculate the temperature of graphite formation. Representative EMP analyses of chlorite from the studied thin sections are presented in the Appendix A (Table 4.2).

The results show that chlorite within the veins have SiO_2 and Al_2O_3 values varying from 25.25 to 31.48 wt.% and 12.25 to 21.75 wt.%, respectively. Additionally, the FeO_t and MgO compositions range from 3.55 to 44.51 wt.% and from 2.89 to 31.62 wt.%, respectively (Table 4.2). In general, there is a considerable variation in the FeO_t and MgO amounts of the chlorite veins. In the host rock, chlorite SiO_2 values range from 29.97 to 34.41 wt.%, Al_2O_3 range from 16.37 to 21.01 wt.%, FeO_t range from 4.60 to 11.98 wt.%, and finally, MgO vary from 22.66 to 31.63 wt.% (Table 4.2).

Chlorite structural formulae were calculated based on 28 oxygen atoms per formula unit (*a.p.f.u.*) (Table 4.2). Using the chlorite classification diagram of Hey (1954), it was determined that there are two types of chlorites: clinochlore (Mg-rich) and chamosite (Fe-rich) (Fig. 4.13). The samples that plot in the fields of diabantite (RS22-01-5b), pennite (the host rock: RS22-03-1), and pycnochlorite (RS22-01-4, RS22-03-9b, and RS22-04-8) are classified as Mg-rich chlorite varieties (Fig. 4.13). The host rock samples (RS22-01-2, RS22-01-5a, RS22-04-12) that also plot in the clinochlore domain are highly rich in MgO. The diagram also indicates that samples RS22-01-1a, RS22-01-5a, RS22-04-9a mainly fall in the domains of brunsvigite and chamosite (Fe-rich chlorites). Furthermore, these Fe-rich chlorites are also rich in Si (Fig. 4.13).

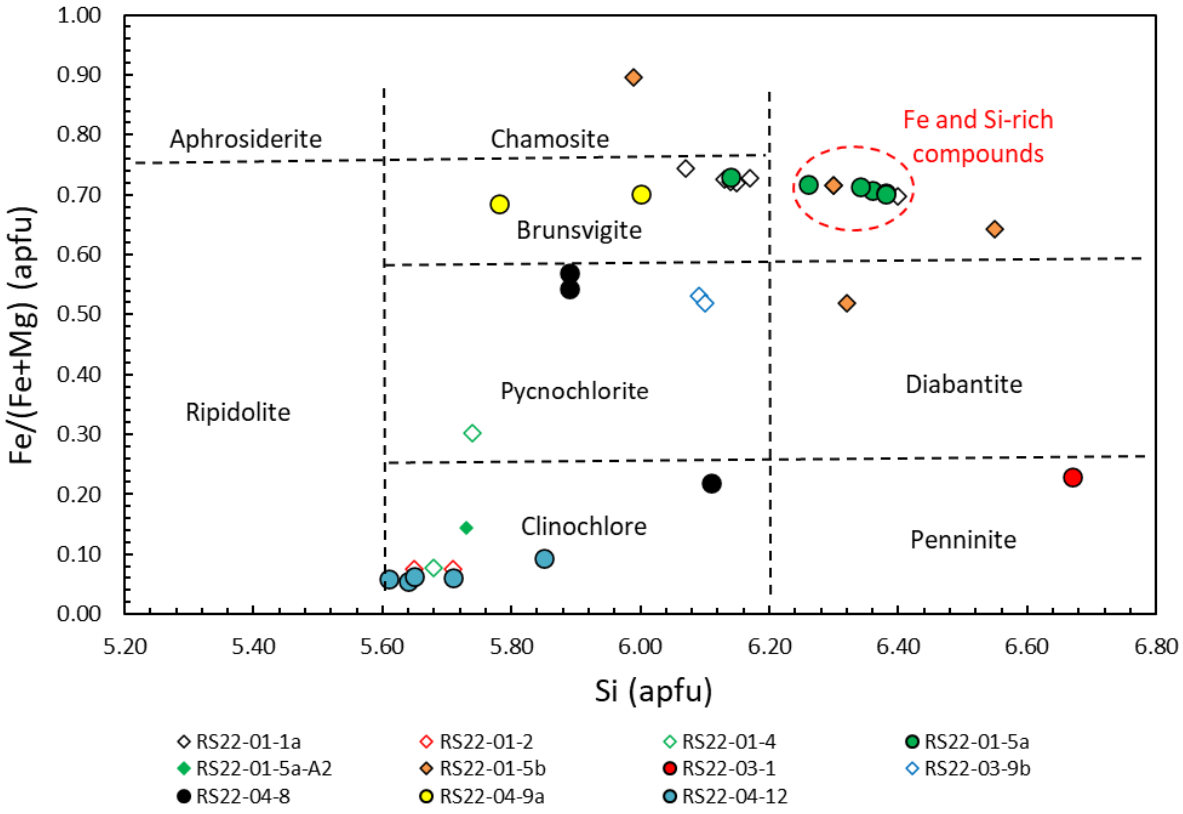

Figure 4.13: *Rockstone chlorite classification diagram according to Hey (1954) classification (symbols in red represent host rock samples; all other colors represent vein-hosted chlorite samples).*

4.6.1) Host Rock and Vein-hosted Chlorite Geothermometry

In this study, the EMP analyses of chlorite (in veins and host rock) were used to calculate the formation temperature of chlorite, and thus of the system that might have formed the graphite in veins. Several investigations (Hey, 1954; Cathelineau, 1988; Caritat et al., 1993; Bourdelle et al., 2013; Bourdelle and Cathelineau, 2015; Bourdelle, 2021) have demonstrated that the composition of chlorite can be used to determine temperatures of chlorite formation because the composition partly rely on chemistry of the system, including the fugacity of oxygen, and finally, temperature and pressure. Basically, two types of thermometers were applied to Rockstone chlorite samples (Cathelineau and Nieva, 1985; Bourdelle and Cathelineau, 2015).

The Cathelineau and Nieva (1985) chlorite geothermometer calculation (equations 1 and 2 below) is mainly based on empiric estimations (Al^{iv} and Al_c^{iv} (corrected) values and the Fe/(Fe+Mg) ratio; Cathelineau and Nieva, 1985; Kranidiotis and MacLean, 1987). The uncertainty of the geothermometer is about ±25°C (Cathelineau and Nieva, 1985).

$$T\ (°C) = 106 \times Al_c^{iv} + 18, \qquad (1)$$

$$Al_c^{iv} = Al^{iv} + 0.7 \times Fe/(Fe + Mg). \qquad (2)$$

The calculations yield formation temperatures within the veins between 144 to 298°C, with a median of 186°C. Temperatures for three host-rock chlorite crystals that texturally do not show a direct relationship to graphite range from 177 to 291°C, with a median of 285°C (Table 4.2).

A more recent graphical representation of the chlorite thermometer (Bourdelle and Cathelineau, 2015) is especially useful for chlorite that crystallized low temperatures (T< 350°C) using the models of Inoue et al. (2009) and Bourdelle et al. (2013) to calibrate and support the graphical diagram. These two model thermometers directly link temperature to the K, equilibrium constant as (equation 3):

$$\text{Al-free Mg-chlorite} + 3\ \text{Mg-sudoite} = 3\ \text{Mg-amesite} + 7\ \text{Quartz} + 4\ H_2O, \qquad (3)$$

The temperature range for this thermometer is between ~50 and ~350°C with an uncertainty of ±25°C (Bourdelle and Cathelineau, 2015). Using Bourdelle and Cathelineau (2015)'s graphical chlorite temperature representation, Rockstone vein-hosted chlorite yielded temperatures ranging from ~150 to 280°C, except for one temperature, which is situated ~112°C isotherm (Fig. 4.14). The majority of the chlorite temperatures are clustered between 200 and 250°C isotherms (Fig. 4.14). According to the thermometric calculations of Bourdelle and Cathelineau (2015) and Cathelineau and Nieva (1985), the calculated temperature ranges appear

to be closely comparable.

The T–R^{2+}–Si diagram of vein-hosted chlorite samples (Fig. 4.14), the data points cluster into two distinct groups. These two groups reflect differences in the Si, Fe^{2+}, and Mg^{2+} compositions of chlorite samples. All data points represent vein-hosted chlorite samples with similar textural characteristics. Chlorite is commonly observed in association with Si-bearing silicates such as quartz and muscovite. The observed Si enrichment in the upper group may be attributed to this spatial association with silicate minerals.

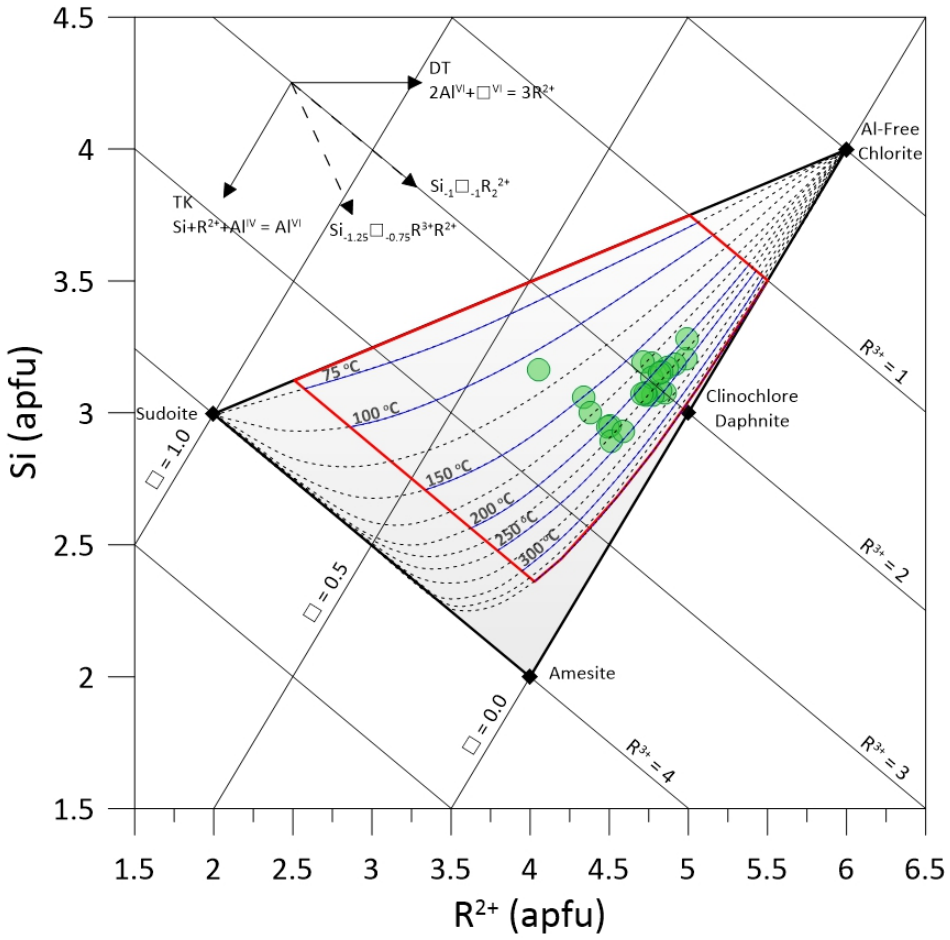

Figure 4.14: *T - R^{2+}- Si diagram of vein-hosted chlorite samples developed by Bourdelle and Cathelineau (2015). This graphical representation diagram was drawn with the windows programme developed by Yavuz et al. (2015) for chlorite classification and temperature calculations.*

4.7) Mica Chemistry and Ti-in-biotite Geothermometry of Host Rock Biotite

Electron microprobe analyses of mica group minerals in the host rock and veins are shown in the Appendix B (Tables 4.3-4.5). Major element compositions of micas from both host rocks (RS22-03-1 and RS22-04-10a) and vein-hosted (RS22-01-5a, RS22-04-8, RS22-04-9a and RS22-04-12) samples show variations in TiO_2, MgO, FeO_t and K_2O contents (Tables 4.3-4.5). According to the M-site cation compositions presented in the electron microprobe analyses, the mica samples can be classified into two main types: dioctahedral (muscovite) and trioctahedral (phlogopite) micas (Tables 4.3-4.5).

TiO_2 concentrations are higher in host rock trioctahedral mica (up to 2.16 wt.%) compared to vein-hosted samples, where TiO_2 ranges between 0.21 and 1.05 wt.%. MgO contents are significantly elevated in vein-hosted trioctahedral micas, with values ranging from 20.25 to 22.88 wt.%, while dioctahedral mica samples from both vein and host rock settings exhibit lower MgO contents, between 2.42 and 4.30 wt.%. Host rock trioctahedral micas display intermediate MgO values (16.71–17.52 wt.%). FeO^t values are highest in host rock (11.12–12.08 wt.%), moderate in vein-hosted trioctahedral mica (2.06–4.34 wt.%), and lowest in dioctahedral mica samples (0.25–6.43 wt.%). Additionally, K_2O contents are relatively consistent with all mica types, ranging from 8.06 to 11.31 wt.%. Vein-hosted dioctahedral and trioctahedral micas generally exhibit slightly higher K_2O values compared to host rock micas (Tables 4.3-4.5).

There is no textural relationship between the trioctahedral micas in the host rock and those present in veins. However, graphite and muscovite exhibit a clear textural association within veins. The Rockstone mica samples were classified in a diagram using their calculated a.p.f.u. values for Mg, Fe, and Al^{iv} (Fig. 4.15). The samples are clearly divided into compositional groups. All samples plot in the phlogopite domain, including both vein-hosted and

host rock samples (Fig. 4.15). A close examination of the mica classification diagram reveals that the trioctahedral mica samples associated with veins are richer in Mg compared to those from the host rock, which are comparatively richer in Fe (Fig. 4.15). This suggests that the fluid responsible for vein formation was relatively enriched in Mg.

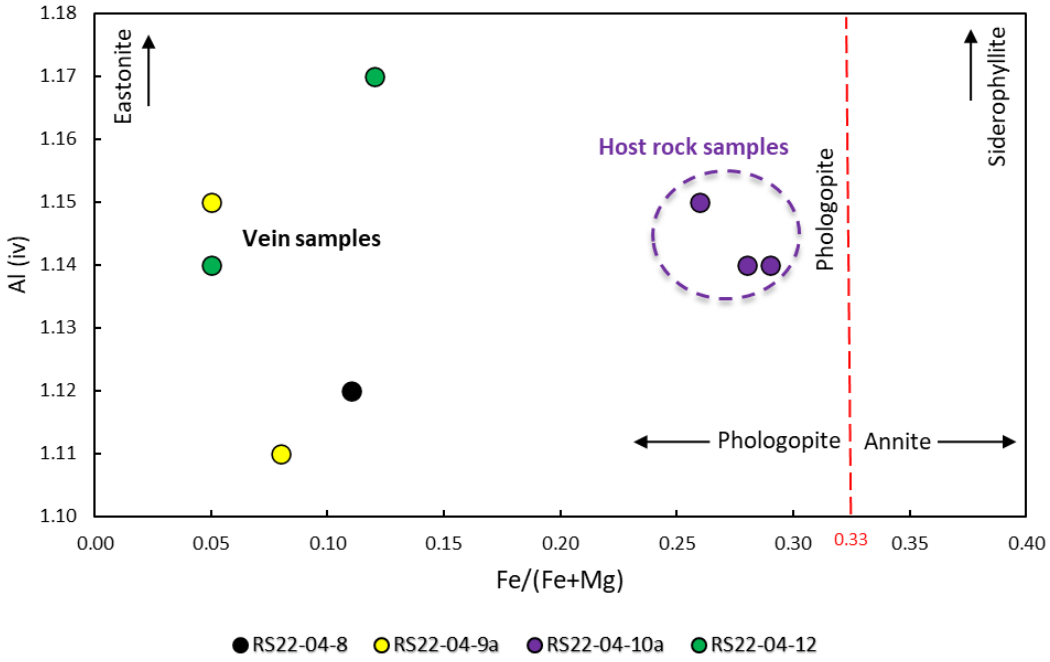

Figure 4.15: *Classification of Rockstone mica minerals (after Rieder et al., 1998; Samples RS22-04-8, RS22-04-9a, and RS22-04-12 represent micas from vein-hosted, while RS22-04-10a represent mica samples from the host rock).*

To estimate the metamorphic temperature of the host rock, three samples (RS22-04-10a) were analyzed (Table 4.5). The samples contain MgO ranging from 16.71 to 17.52 wt.% and FeO_t ranging from 11.12 to 12.08 wt.% (Table 4.5). The structural formulae were calculated on the basis of 11 oxygen atoms per formula unit (*a.p.f.u.*) (Tables 4.3-4.5).

Titanium, Mg, Fe and Al^{vi} contents in biotite can be used to determine temperature in metapelites in the presence of Ti-bearing phases (rutile, ilmenite and titanite) (Henry et al., 2005; Chambers and Kohn, 2012; Wu and Chen, 2015; Sukhorukov et al., 2021; Al-Ani et al., 2022).

The biotite formation temperature was determined using the empirically calibrated Ti-in-biotite geothermometer of Wu and Chen (2015) for ilmenite- or rutile-bearing metapelites; equations 4-7 below. The calibration ranges are: 450–840 °C, 0.1–1.9 GPa, X_{Ti} = 0.02–0.14 in biotite and the precision of the geothermometer is no more than approximately ±65°C.

$$\ln [T\ (°C)] = 6.313 + 0.224 \times \ln (X_{Ti}) - 0.288 \times \ln (X_{Fe}) - 0.449 \times \ln (X_{Mg}) + 0.15\ (GPa), \quad (4)$$

where

$$X_{Ti} = Ti/(Fe + Mg + Al^{vi} + Ti), \quad (5)$$

$$X_{Fe} = Fe/(Fe + Mg + Al^{vi} + Ti), \quad (6)$$

$$X_{Mg} = Mg/(Fe + Mg + Al^{vi} + Ti). \quad (7)$$

X_{Ti} of Rockstone biotite (RS22-04-10a) varies between 0.07 to 0.12, well within the range of the Wu and Chen (2015) calibration (Table 4.5). The calculated temperatures of Rockstone biotite in the host rock vary from 501 to 569°C (±65°C), with a median of 562°C.

4.8) Raman Spectra of Rockstone Graphite Material

The Raman spectra of Rockstone graphite (RS22-01-4, RS22-01-5a, RS22-01-5b, RS22-04-9a, RS22-04-9b) are summarized in Table 4.6 and Figure 4.16. The Raman study is sensitive to grain size and ideal orientation of c-axis (Wopenka and Pasteris, 1993; Beyssac et al., 2002). The Raman spectrum of Rockstone graphite has primarily the first order (1000 to 1800 cm^{-1}) and second order (2400 to 3000 cm^{-1}) regions (Beyssac et al., 2002). The first order regions contain primarily three peaks; D1 (~1340 cm^{-1}), G (~1580 cm^{-1}) and D2 (~1610 cm^{-1}) peaks, where “D” stands for disordered carbonaceous material and “G” means fully ordered graphite (Fig. 4.16). The second order region contains primarily two peaks: S1 (~2450 cm^{-1}) and S2 (~2700 cm^{-1}) (Fig. 4.16). The S2 peak, which represents the overtone of the D1 band, is more prominent than the S1 peak (Fig. 4.16). Refer to the Appendix C for the Raman shifts of all samples.

Table 4.6: *Raman spectroscopies of vein-hosted graphite samples.*

		Raman shift (cm-1)			Height			Peak area			Height ratio	Area ratio	T (°C) (± 50)	
Sample	**Graphite Type**	**G**	**D1**	**D2**	**G**	**D1**	**D2**	**G**	**D1**	**D2**	**R1**	**R2**	***1**	****2**
RS22-01-4-008	folded flakey	1583	1340	1619	4192	1192	605	119792	68592	17132	0.28	0.33	492	466
RS22-01-4-009	folded flakey	1583	1333	1620	3971	4315	1359	114800	210330	25189	1.09	0.60	374	350
RS22-01-4-010	folded flakey	1582	1338	1620	6605	1970	881	144592	87778	9036	0.30	0.36	479	438
RS22-01-5a-004	folded flakey	1583	1336	1618	8931	5527	1967	304794	308727	41017	0.62	0.47	431	402
RS22-01-5b-002	folded flakey	1586	1336	1610	3421	3014	1028	103520	155248	22785	0.88	0.55	396	369
RS22-01-5b-017	folded flakey	1588	1344	1610	1502	635	319	38757	27981	5444	0.42	0.39	468	445
RS22-04-9a-002	aggregate	1583	1334	1620	9820	6510	2150	264687	335113	44603	0.66	0.52	410	360
RS22-04-9a-004	aggregate	1583	1334	1621	12088	7448	2151	318119	368913	42107	0.62	0.51	416	365
RS22-04-9a-006	aggregate	1583	1336	1605	15292	7720	3471	503245	421354	73176	0.50	0.42	453	428
RS22-04-9a-010	aggregate	1582	1339	1602	6943	3291	2129	250678	181010	43026	0.47	0.38	471	464
RS22-04-9b-004	aggregate	1585	1339	1604	3159	1570	1203	123374	97705	23945	0.50	0.40	464	451
RS22-04-9b-006	aggregate	1583	1333	1604	7489	5135	2005	260815	268239	44375	0.69	0.47	433	420

*Beyssac et al. (2002); **Rahl et al. (2005)

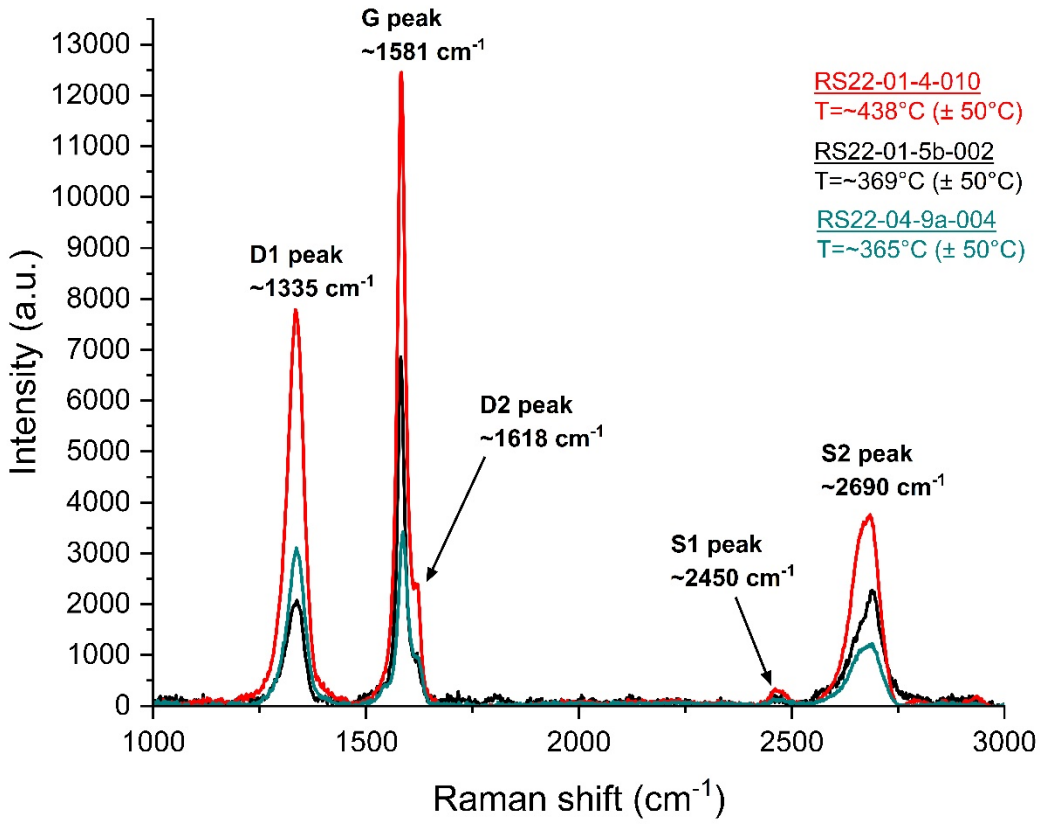

Figure 4.16: *Representative Raman spectroscopy of vein-hosted graphite samples. The first (D1, G and D2) and second order (S1 and S2) peaks are seen together.*

4.8.1) Raman Geothermometry

Generally, R1 and R2 (equations 8 and 9, respectively) ratios represent the Raman parameters that are used for determining the degree of graphite crystallinity (Roberts et al., 1995; Beyssac et al., 2002):

$$R1 = D1/G \text{ (ratio of Raman peaks heights)}, \quad (8)$$

$$R2 = D1/(G+D1+D2) \text{ (ratio of the Raman band areas)}, \quad (9)$$

R1 of poorly ordered carbonaceous matter varies from 1 to ~2.6 but the same ratio for highly ordered material is between 0.1 and 0.3 (Beyssac et al., 2002). R1 parameters of Rockstone

graphite vary from 0.28 to 1.09, which indicates poorly ordered, disordered graphite (Table 4.6). Beyssac et al. (2002) also related R2 to temperature where (equation 10):

$$T\ (°C) = -\ 445 \times R2 + 641\ (\pm 50°C), \qquad (10)$$

and as temperature increases, the R2 ratio gradually decreases. The theoretical temperature range for this equation is between ~330 and 640°C. R2 ratios of Rockstone graphite range from 0.33 to 0.60 (Table 4.6). Calculated peak metamorphic temperatures of vein-hosted graphite range from 374 to 492°C (±50°C) with a median of 443°C (Beyssac et al., 2002; Table 4.6).

Rahl et al. (2005) developed a more sensitive formulation (equation 11) than Beyssac et al. (2002)'s to calculate the peak metamorphic temperature:

$$T\ (°C) = 773.3 + 320.9 \times R1 - 1067 \times R2 - 80.638 \times R2^2\ (\pm 50°C), \qquad (11)$$

The temperature range over which the Rahl et al. (2005) formulation is reliable and is between 100 and 700°C. Calculated temperatures of vein-hosted graphite ranges from 350 to 466°C (±50°C) with a median of 424°C (Rahl et al., 2005; Table 4.6). These calculated temperatures using the two different formulations are consistent with each other and indicates that graphite formed under greenschist facies conditions.

4.9) Carbon and Sulfur Isotope Analyses

4.9.1) Carbon

The $\delta^{13}C_{V\text{-}PBD}$ (‰) values of vein-hosted graphite are given in Table 4.7 and Figure 4.17. The $\delta^{13}C$ values have a narrow range, varying from –41.1 to –33.3‰ with an average value of –36.6‰ (n=28) (Fig. 4.17). Therefore, the results show a ~7 ‰ change in $\delta^{13}C$. The carbon isotope values have highly depleted isotopic signatures. Folded graphite flakes and graphite aggregates (fragments) show a similar range of $\delta^{13}C$ values. The $\delta^{13}C$ values of folded graphite grains range from –38.3 to –33.7‰ with average values of –36.4‰ (n=18). On the other hand,

the $\delta^{13}C$ values of graphite fragments fall within the range of –41.1 to –33.3‰ with average values of –36.9‰ (n=10) (Table 4.7).

Table 4.7: *Carbon isotope data of vein-hosted graphite samples.*

Sample	Explanation	$\delta^{13}C_{V\text{-}PBD}$ (‰)	1σ (‰)
RS22-01-01a-01	Folded grain	-38.3	0.6
RS22-01-01a-02	Folded grain	-36.7	0.6
RS22-01-01a-03	Folded grain	-35.9	0.6
RS22-01-01a-04	Fragments in calcite fill	-35.5	0.6
RS22-01-01a-05	Fragments in calcite fill	-36.8	0.6
RS22-01-01a-06	Fragments in calcite fill	-33.3	0.6
RS22-01-01a-07	Fragments in calcite fill	-35.3	0.6
RS22-01-01a-08	Fragments in calcite fill	-36.6	0.6
RS22-01-04-01	Folded grain	-37.4	0.5
RS22-01-04-02	Folded grain	-36.5	0.5
RS22-01-04-03	Folded grain	-37.5	0.5
RS22-01-04-04	Folded grain	-33.9	0.5
RS22-01-04-05	Folded grain	-35.2	0.5
RS22-01-04-06	Folded grain	-38.2	0.5
RS22-01-04-07	Folded grain	-36.4	0.5
RS22-01-04-08	Folded grain	-37.0	0.5
RS22-01-04-09	Folded grain	-37.5	0.5
RS22-01-04-10	Folded grain	-37.9	0.5
RS22-01-5a-01	Folded grain	-35.7	0.5
RS22-01-5a-02	Folded grain	-33.7	0.5
RS22-01-5a-03	Folded grain	-36.3	0.5
RS22-01-5a-04	Folded grain	-36.8	0.5
RS22-01-5a-05	Folded grain	-34.6	0.5
RS22-04-12-01	Fragments	-38.0	0.5
RS22-04-12-02	Fragments	-36.8	0.5
RS22-04-12-03	Fragments	-37.3	0.5
RS22-04-12-04	Fragments	-41.1	0.5
RS22-04-12-05	Fragments	-38.7	0.5

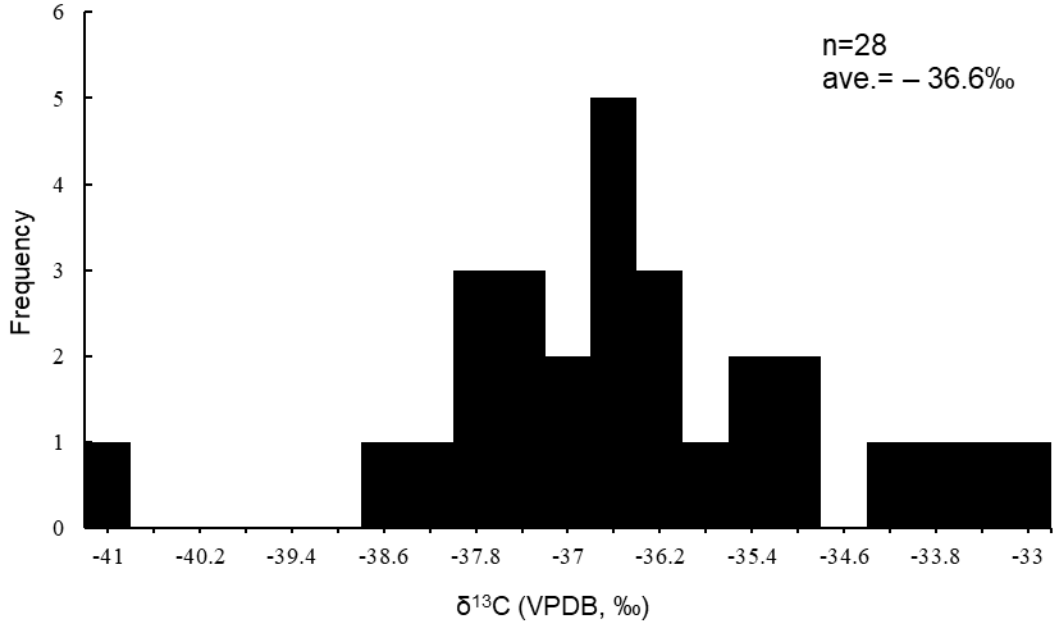

Figure 4.17: *Frequency distribution of carbon isotope composition of vein-hosted graphite samples.*

The bulk carbon isotopic analysis of one sample (RS22-01-4) yielded the $\delta^{13}C$ value of –34.8‰, which is consistent with carbon isotope values obtained from the SIMS analysis. On the other hand, the carbon isotopic analysis of three calcite vein samples yielded the $\delta^{13}C$ values of –5.6, –6.2 and –6.5‰.

4.9.2) Sulfur

The $\delta^{34}S_{V\text{-}CDT}$ (‰) values of sulfides are presented in Table 4.8. and Figure 4.18. Sulfur isotope analyses were performed on recrystallized pyrite grain, in addition to vein-hosted pyrite, sphalerite, and pyrrhotite samples. Vein-hosted pyrite yielded relatively wide range of $\delta^{34}S$ values, ranging from –0.5 to +4.1‰ with the average values of +1.5‰ (n=16). The $\delta^{34}S$ values of recrystallized pyrite within the central zones of the grain exhibit a consistently narrow range, from +0.3‰ to +1.4‰ (n = 9). In contrast, measurements from the outer edge of the grain yield moderately wide and more positive $\delta^{34}S$ values, ranging from +0.9‰ to +4.0‰ (n = 10). This

trend indicates a progressive increase in $\delta^{34}S$ values from the center toward the margins of the recrystallized pyrite crystal, reaching up to +4.0‰ at the edges (Table 4.8). Sphalerite yielded a similar, narrow range of $\delta^{34}S$ values, varying from +2.3 to +4.4‰. Pyrrhotite, the $\delta^{34}S$ values also fall in a narrow range, varying from +2.2 to +3.6‰. Overall, the sulfur isotope compositions of the sulfides primarily show positive values (Table 4.8 and Fig. 4.18).

Table 4.8: *Sulfur isotope data of vein-hosted sulfides.*

Sample	Mineral	$\delta^{34}S$ (CDT ‰)	1σ (‰)
RS22-01-4-01	Pyrite	1.6	0.2
RS22-01-4-02	Pyrite	1.4	0.2
RS22-01-4-03	Pyrite	0.9	0.2
RS22-01-4-04	Pyrite	1.8	0.2
RS22-01-4-05	Pyrite	0.1	0.2
RS22-01-4-06	Pyrite	0.2	0.2
RS22-01-5a-01	Pyrite	-0.5	0.2
RS22-01-5a-02	Pyrite	-0.4	0.2
RS22-01-5a-03	Pyrite	0.6	0.2
RS22-01-5a-04	Pyrite	0.0	0.2
RS22-01-5a-05	Pyrite	1.0	0.2
RS22-03-04-01	Recrystallized pyrite (center)	0.4	0.2
RS22-03-04-02	Recrystallized pyrite (center)	1.4	0.2
RS22-03-04-03	Recrystallized pyrite (center)	0.6	0.2
RS22-03-04-04	Recrystallized pyrite (center)	0.1	0.2
RS22-03-04-05	Recrystallized pyrite (center)	0.9	0.2
RS22-03-04-06	Recrystallized pyrite (center)	0.3	0.2
RS22-03-04-07	Recrystallized pyrite (center)	0.8	0.2
RS22-03-04-08	Recrystallized pyrite (center)	0.7	0.2
RS22-03-04-09	Recrystallized pyrite (center)	0.7	0.2
RS22-03-04-10	Recrystallized pyrite (edge)	3.6	0.2
RS22-03-04-11	Recrystallized pyrite (edge)	2.8	0.2
RS22-03-04-12	Recrystallized pyrite (edge)	1.9	0.2
RS22-03-04-13	Recrystallized pyrite (edge)	2.1	0.2
RS22-03-04-14	Recrystallized pyrite (edge)	2.6	0.2
RS22-03-04-15	Recrystallized pyrite (edge)	2.6	0.2
RS22-03-04-16	Recrystallized pyrite (edge)	1.4	0.2
RS22-03-04-17	Recrystallized pyrite (edge)	0.9	0.2
RS22-03-04-18	Recrystallized pyrite (edge)	1.5	0.2
RS22-03-04-19	Recrystallized pyrite (edge)	4.0	0.2

Table 4.8: *(continued).*

Sample	Mineral	$\delta^{34}S$ (CDT ‰)	1σ (‰)
RS22-01-5a-01	Sphalerite	3.3	0.6
RS22-01-5a-02	Sphalerite	4.6	0.6
RS22-01-5a-03	Sphalerite	2.3	0.6
RS22-01-5a-04	Sphalerite	3.8	0.6
RS22-01-5a-05	Sphalerite	2.6	0.6
RS22-01-5a-06	Sphalerite	3.6	0.6
RS22-01-5a-07	Sphalerite	4.0	0.6
RS22-04-12-01	Sphalerite	4.1	0.6
RS22-04-12-02	Sphalerite	4.6	0.6
RS22-04-12-03	Sphalerite	3.1	0.6
RS22-04-12-04	Sphalerite	6.7	0.6
RS22-04-12-05	Sphalerite	3.7	0.6
RS22-04-12-06	Sphalerite	2.8	0.6
RS22-04-12-07	Sphalerite	2.9	0.6
RS22-04-12-08	Sphalerite	4.4	0.6
RS22-04-12-01	Pyrrhotite	2.2	0.2
RS22-04-12-02	Pyrrhotite	3.6	0.2
RS22-04-12-03	Pyrrhotite	3.4	0.2
RS22-04-12-04	Pyrrhotite	3.3	0.2
RS22-04-12-05	Pyrrhotite	2.4	0.2

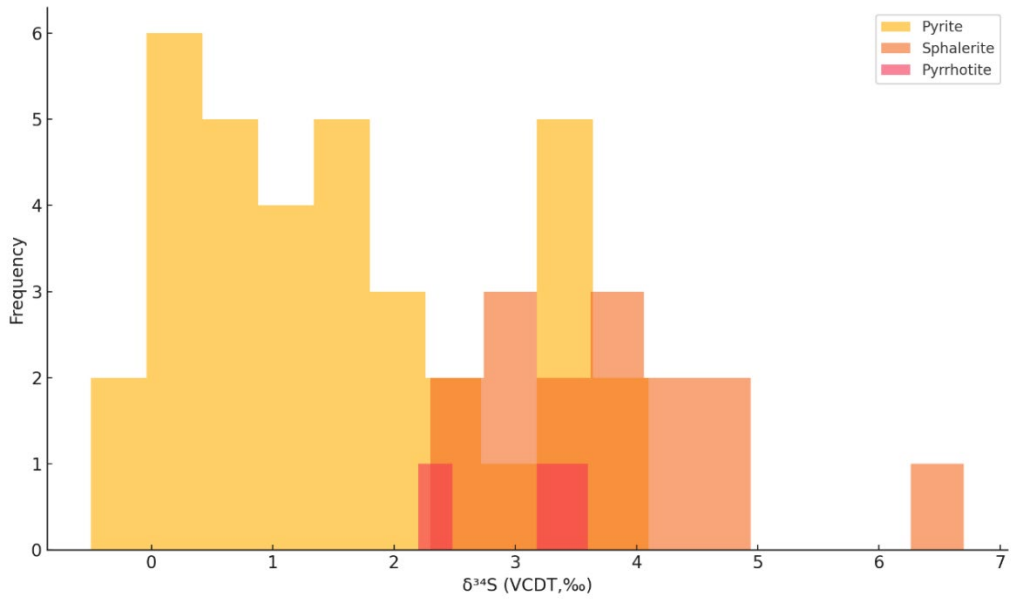

Figure 4.18: *Frequency distribution of sulfur isotope composition of vein-hosted sulfides.*

CHAPTER 5 – DISCUSSION

5.1) Origin of Carbon and Sulfur

Carbon isotope ratios of graphite are primarily used to infer the source of carbon and fluid history in the system that formed the graphite (Schoell and Wellmer, 1981; Weis et al., 1981; Luque et al., 1998; Luque et al., 2012). Furthermore, carbon isotope studies of graphite can also be significant in terms of seeking evidence for early life in the Archean (Schidlowski, 2001; Luque et al., 2012). As mentioned previously (Section 1.3), graphite has primarily three main carbon sources. These are grouped as biogenic (organic), crustal carbonate (e.g., marine limestone and marble) and mantle sources (e.g., in hydrothermal formations), of which the latter two are considered inorganic carbon sources (Weis et al., 1981; Luque et al., 2012). These different reservoirs have distinct carbon isotopic ranges:

- Organic carbon $\delta^{13}C$ values range from ~ -40 to -10‰ with a mean value of -23‰;
- Graphite derived from marine carbonates has a narrow $\delta^{13}C$ range from -2 to +2‰ (average 0‰), which is isotopically heavier than the value for organic matter; and,
- Mantle-derived carbon isotopic compositions are ~7‰ (Fig. 5.1; Weis et al., 1981; Luque et al., 2012).

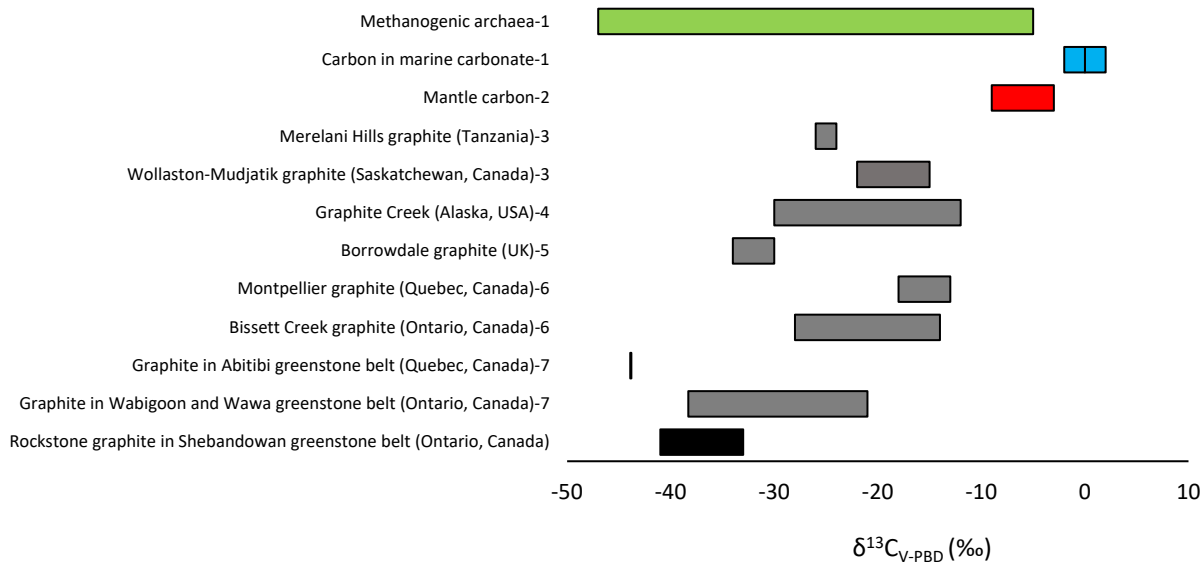

Figure 5.1: *Ranges of $\delta^{13}C$ values from different carbon-bearing reservoirs, as well as graphite of organic origin in Canada and worldwide, based on recent studies. 1-Schidlowski (1988) and Schidlowski (2001); 2-Deines et al. (1991) and Pearson et al. (1994); 3-Toma et al. (2022); 4-Case et al. (2023); 5-Barrenechea et al. (2009); 6-Taner et al. (2017) and Drever et al. (2023); 7- Schoell and Wellmer (1981). Archaea – green; marine carbonates – blue; mantle carbon – red; graphite samples from different locations – grey; Rockstone graphite – black.*

Identifying the source(s) of carbon in graphite is essential for interpreting its fluid history, physico-chemical conditions of crystallization and is therefore critical for reconstructing the geological processes responsible for graphite formation (Ohmoto and Rye, 1979; Duke and Rumble, 1986; Luque et al., 2012; Taner et al., 2017; Drever et al., 2023). Although inorganic graphite deposits do exist particularly in Canada (e.g., Albany and Miller graphite deposits; Conly and Moore, 2015), the majority of graphite in this region are of organic origin (e.g., Wollaston-Mudjatik, Montpellier and Bissett Creek graphite deposits; Toma et al., 2022; Drever et al., 2023). This is supported by recent studies of graphite-bearing units from Canada (Saskatchewan, Quebec, and Ontario) and other regions worldwide (Tanzania, Alaska, and England), which vary significantly in age and consistently indicate that the carbon in graphite is

of organic origin (Fig. 5.1). In Tanzania, graphite from the Merelani Hills is hosted within Neoproterozoic metasedimentary rocks. In contrast, graphite occurrences in the Wollaston-Mudjatik domain (Saskatchewan), Montpellier (Quebec), and Bissett Creek (Ontario) are associated with Mesoproterozoic metasedimentary rocks. Additionally, graphite from Graphite Creek (Alaska) is hosted in Cretaceous metasedimentary rocks. Organic graphite in Borrowdale, UK, occurs within Ordovician volcanic rocks. Meanwhile, graphite found in the Wabigoon, Wawa, and Abitibi greenstone belts of Canada is hosted in Archean metasedimentary and metavolcanic rocks, such as the Rockstone graphite occurrence in the Shebandowan greenstone belt (Schoell and Wellmer, 1981; Barrenechea et al., 2009; Taner et al., 2017; Toma et al., 2022; Case et al., 2023; Drever et al., 2023). The $\delta^{13}C$ values for Rockstone graphite, ranging from -41 to -33‰, are relatively homogeneous compared to other typical organic graphite deposits in Canada and worldwide (Fig. 5.1; Schoell and Wellmer, 1981; Barrenechea et al., 2009; Taner et al., 2017; Toma et al., 2022; Drever et al., 2023; Case et al., 2023), and are among the lowest reported for Precambrian graphite (Fig. 5.1). The only known exception is graphite from the Neoarchean Abitibi greenstone belt in Languedoc Township, Quebec, which has a $\delta^{13}C$ value of –43.8‰ (Fig. 5.1; Schoell and Wellmer, 1981). The $\delta^{13}C$ compositions of Rockstone graphite falls within the expected range of carbon isotopic ratios for organic compounds, particularly those associated with methanogenic archaea as the organic precursor (Fig. 5.1). Moreover, the very low and narrow range of isotope values suggests a single organic carbon source. Consequently, the results indicate that the graphite in Rockstone was derived from organic matter deposited in Neoarchean basins of the Superior Province. Given the Archean age of Rockstone graphite, the organic precursor was likely derived from a marine ecosystem.

Primarily, ^{13}C depletion in organic matter occurs during bacterial reduction. As a result, highly depleted graphitic carbon may originate from anaerobic process such as methanogenesis (Fig. 5.2; Schoell and Wellmer, 1981; Slotznick and Fischer, 2016). Alternatively, ^{13}C depletion in graphite may also be attributed to re-precipitation from CH_4-rich fluids derived from ^{13}C-depleted organic residues (e.g., archaea) under low fO_2 conditions (i.e., in reducing environments; Fig. 5.2; Bottinga, 1969; Barrenechea et al., 2009). Therefore, the very low $\delta^{13}C$ values in graphite in vein systems from the Rockstone property can be explained by precipitation of CH_4-rich fluids, potentially sourced from isotopically light organic precursors. This process may have occurred during devolatilization and/or migration of pre-existing ^{13}C-depleted graphite at depth, driven by metamorphism and/or tectonic activity (Fig. 5.2; Morikiyo 1986; Gautneb and Tveten 2000; Luque et al., 2012; Pascal et al., 2015; Pascal et al., 2016; Santos et al., 2022; Drever et al., 2023). Hahn-Weinheimer and Hirner (1981) and Dunn and Valley (1992) describe several mechanisms that may cause variations in $\delta^{13}C$ values in graphite: (1) devolatilization caused by any degree of metamorphism, (2) precipitation of graphite from fluids containing methane with differing carbon isotope compositions, and (3) isotopic exchange between graphite and isotopically heavy carbon compounds such as crustal carbonates. In the study area, the latter process may involve the minor calcite veins associated with graphite. Any of these mechanisms can account for the observed 7.8 ‰ range in $\delta^{13}C$ values of graphite (Fig. 5.1). Overall, the $\delta^{13}C$ values of Rockstone graphite, ranging from -41‰ to -33‰, fall within the typical range for organic carbon (-40‰ to -10‰).

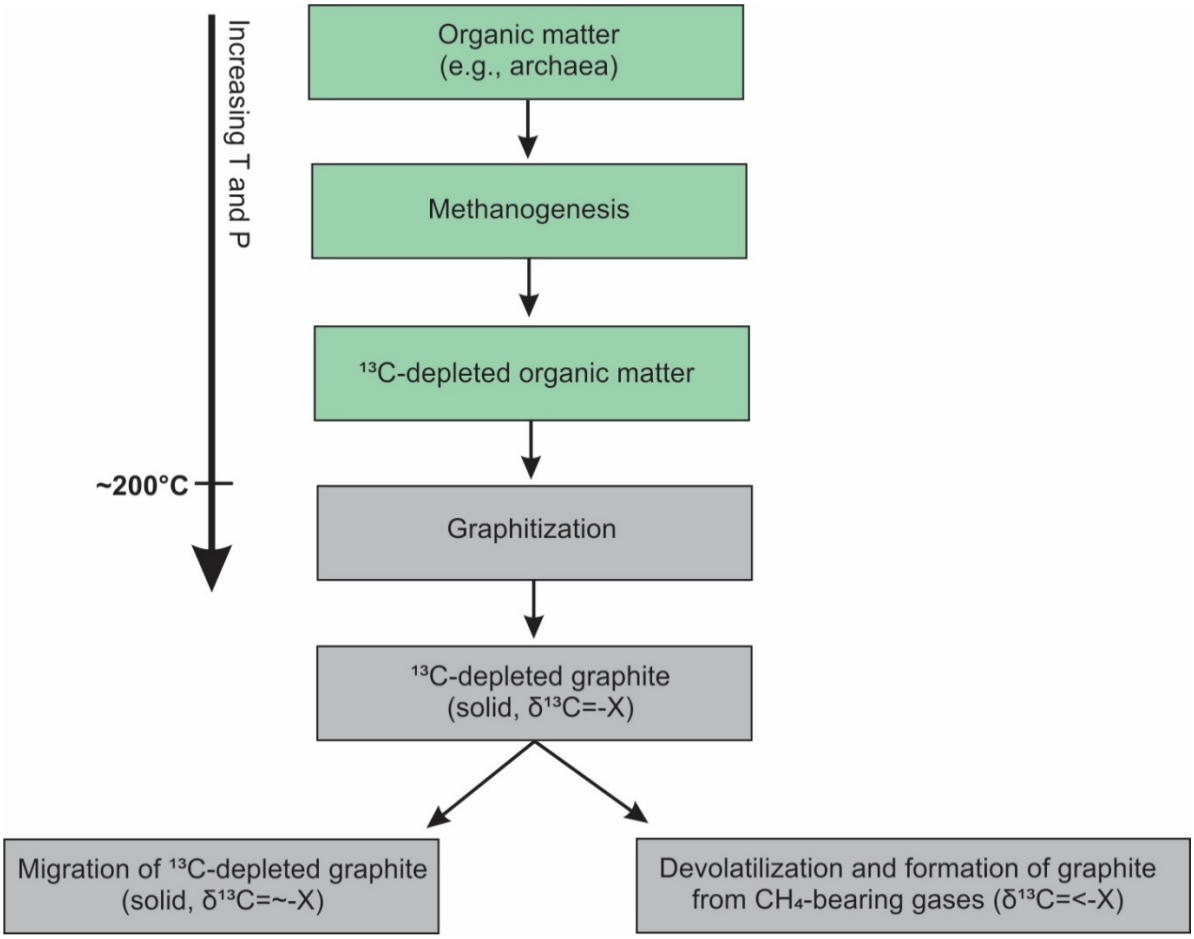

Figure 5.2: *Schematic diagram showing the maturation of organic matter with increasing pressure and temperature with depth, and the evolution of $\delta^{13}C$ values in graphite (modified from Crespo et al., 2004; Luque et al., 2012).*

As an alternative to formation of graphite, the frequent association of graphite with hydrous minerals such as chlorite, muscovite along with the presence of quartz, albite and sulfide mineral paragenesis (e.g., pyrite, sphalerite) in the veins suggests that there is a possibility of hydrothermal graphite formation through Fischer-Tropsch (FT) reactions (Horita, 2005; Ortega et al., 2010; Conly and Moore, 2015). This interpretation is primarily supported by the occurrence of graphite within chlorite and sulfide-rich veins, which are commonly interpreted as products of hydrothermal alteration (Barrenechea et al., 2009; Ortega et al., 2010).

CH_4, which is commonly present in reducing geological environments, can contribute to graphite precipitation through reactions involving O_2 or CO_2. One such reaction (equation 12) involves the oxidation of CH_4:

$$\mathbf{CH_4 + O_2 \rightarrow C_{(graphite)} + 2H_2O} \qquad (12)$$

Alternatively, graphite can also precipitate via a redox reaction (equation 13) between CH_4 and CO_2:

$$\mathbf{CH_4 + CO_2 \rightarrow 2C_{(graphite)} + 2H_2O} \qquad (13)$$

These reactions represent abiotic carbon precipitation pathways that are analogous to Fischer-Trophy (FT) synthesis, mostly occurring under hydrothermal conditions (Horita, 2005; Barrenechea et al., 2009; Ortega et al., 2010; Conly and Moore, 2015). Graphite is typically found in association with hydrous silicate minerals (e.g., chlorite and muscovite) and the presence of sulfides and CH_4-rich fluids indicates a strongly reducing environment. It is plausible that CH_4-rich fluids, migrating through structural conduits, precipitated graphite by decomposing CH_4 under favorable pressure-temperature conditions. Simultaneously, H_2O is incorporated into minerals during their formation, which may facilitate graphite precipitation (Ortega et al., 2010).

Furthermore, the presence of deep-seated organic matter (depleted in ^{13}C) may have served as the carbon source for these hydrothermal fluids. The observed mineral assemblages and isotopic signatures may therefore record a hydrothermal pathway for Rockstone graphite formation.

The formation of Rockstone graphite appears to be unique, as it likely originated from a single organic carbon source (as discussed above) and exhibits poor crystallinity (i.e., a turbostratic structure), as indicated by Raman and TEM results. This combination suggests a complex tectonic history that influenced the graphite's precipitation mechanisms. One possibility

is that CH_4-bearing metamorphic fluids were devolatilized from organic-rich rocks under reducing conditions. Alternatively, or additionally, organic matter may have been emplaced along shear zones, migrating upward from metasedimentary and metavolcanic host rocks (Fig. 5.2; Nabelek et al., 2003; Luque et al., 2012; Pascal et al., 2016a; Pascal et al., 2016b; Santos et al., 2022; 2024).

Sulfides in the Rockstone property have $\delta^{34}S$ values range between -0.5 to +6.7‰, a spread of approximately 7‰ (standard deviation of 1.5‰; Figs. 5.3 and 5.4). The sulfur isotopic compositions of Archean rocks, metamorphic rocks, seawater, and volcanogenic massive sulfides (VMS) deposits have been extensively studied (Ohtomo, 1996; Franklin et al., 2005; Jamieson et al., 2006; Huston et al., 2010; Johnston, 2011; Sharman et al., 2015).

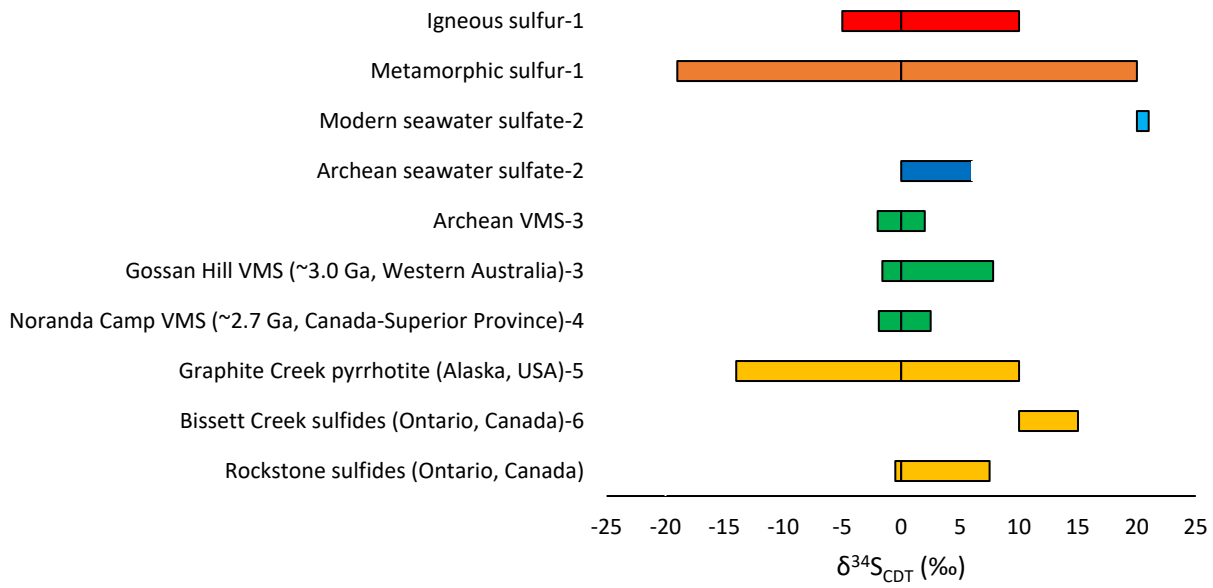

Figure 5.3: *Ranges of $\delta^{34}S$ values for Rockstone sulfides and examples from different sulfur-bearing reservoirs in Canada and worldwide, based on recent studies, as well as sulfides associated with graphite formation in 5 and 6. 1-Hoefs (2009); 2-Strauss (1986) and Hoefs (2009); 3-Sharpe and Gemmell (2000) and Huston et al. (2010); 4-Sharman et al. (2015); 5-Case et al. (2023); 6-Drever et al. (2023). Igneous sulfur – red; metamorphic sulfur – orange;*

sulfur in modern seawater sulfate and Archean seawater sulfate – blue; sulfur in VMS settings – green; sulfides associated with graphite from Alaska and Ontario – yellow.

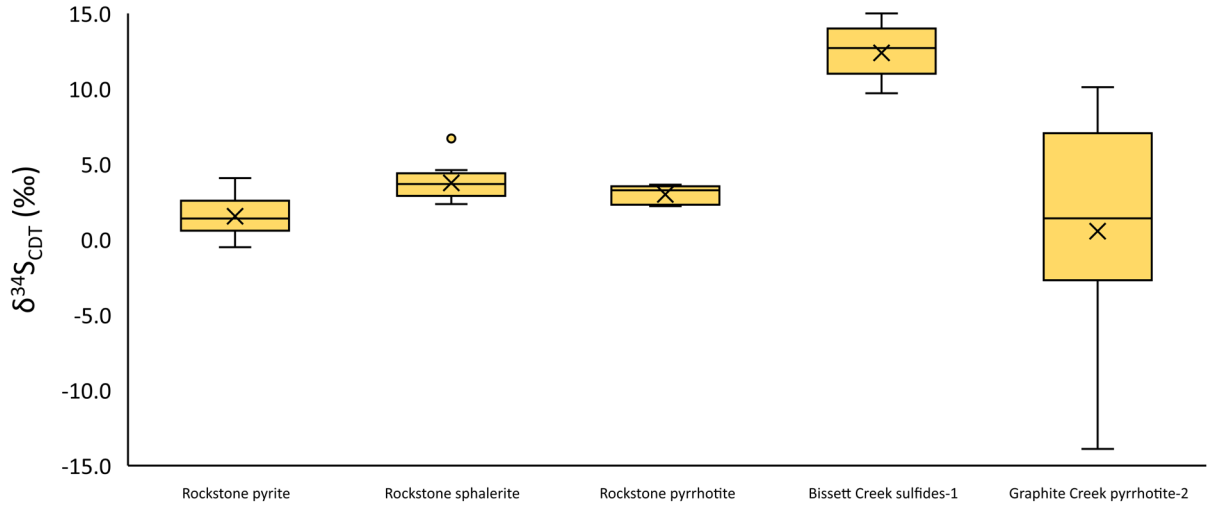

Figure 5.4: *Box-and-whisker plot of $\delta^{34}S$ values of sulfide minerals from the Rockstone property, compared with $\delta^{34}S$ values of sulfide samples associated with graphite in Ontario (Canada) and Alaska (USA). 1-Drever et al. (2023); 2-Case et al. (2023).*

According to Ohtomo (1996), the $\delta^{34}S$ composition of Archean seawater sulfate (SO_4^{2-}) is relatively uniform between 0 and 2‰ (Fig. 5.3). Strauss (1986) and Sharpe and Gemmel (2000) suggest that $\delta^{34}S$ abundances in Archean seawater sulfate can vary more broadly, from 2 to 6‰. However, sulfides from Archean VMS settings generally show $\delta^{34}S$ values ranging from -2‰ to +8‰ (Fig. 5.3; Huston et al., 2010; Sharman et al., 2015). For example, sulfides from the VMS deposits of Gossan Hill (Mesoarchean, 3.0 Ga), Western Australia and Noranda (Neoarchean, 2.7 Ga), Abitibi greenstone belt, Canada range between -1.6 and 7.8‰ and between -1.9 and +2.5‰, respectively (Fig. 5.3). In addition, $\delta^{34}S$ values of metamorphic sulfur reservoirs span a wide range, -20‰ to +20‰, indicating the influence of diverse sulfur sources (e.g., seawater sulfate, sedimentary and magmatic) and metamorphic processes such as devolatilization, redox

reactions, and the remobilization or recrystallization of pre-existing sulfide minerals (Hoefs, 2009; Faure and Mensing, 2005). These ranges overlap with the $\delta^{34}S$ values observed in Rockstone sulfide minerals (Fig. 5.3). The sulfur isotopic compositions of Rockstone sulfides may suggest the involvement of sulfur derived from both Archean seawater sulfate and a magmatic source (Figs 5.3 and 5.4). The presence of metasedimentary and metavolcanic host rocks, along with nearby VMS deposits, supports the hypothesis that interaction between seawater sulfate and magmatic sulfur contributed to the formation of the Rockstone sulfides. Furthermore, the involvement of metamorphic sulfur, released during devolatilization of the surrounding sedimentary rocks, may have also influenced the sulfur isotope signatures observed in the Rockstone sulfides (Fig. 5.3).

The sulfur isotopic composition of sulfides can be affected by various sulfur sources (e.g., Archean seawater sulfate, magmatic sulfur and sedimentary sulfur) as well as by several processes such as microbial reduction, redox conditions, fluid mixing, metamorphism and/or devolatilization (Strauss, 1986; Faure and Mensing, 2005; Franklin et al., 2005; Huston et al., 2010; Bucholz et al., 2020). In a deformed pyrite clast in the host rock, $\delta^{34}S$ values increase from 0.7‰ in the core to 2.4‰ in the rim of the clast. This enrichment towards the rim indicates a relative increase in ^{34}S. In contrast, there is no sulfur isotope zoning observed in vein sulfides associated with graphite in veins, where sphalerite, pyrrhotite, and pyrite exhibit $\delta^{34}S$ values ratios up to 6.7‰. The presence of sulfur isotope in the deformed pyrite suggests that metamorphism-related recrystallization may have altered the sulfur isotopic composition of the pyrite (Martin et al., 2024). The slightly high er $\delta^{34}S$ values observed in sphalerite and pyrrhotite, relative to pyrite, likely reflect equilibrium sulfur isotope fractionation. In this process, pyrite preferentially incorporates the lighter isotope (^{32}S) due to its disulfide bonding, resulting in

relative enrichment of ^{34}S in sphalerite and pyrrhotite. This isotopic pattern may have been further enhanced by late-stage re-equilibration during cooling (Fig. 5.4). Alternatively, the observed variations could also result from devolatilization and recrystallization during metamorphism (Faure and Mensing, 2005; Martin et al., 2024).

5.2) Significance of TEM Observations

The morphology and nanostructure of Rockstone graphite reveal deformation patterns between graphene layers. The detailed TEM study (HRTEM and STEM images) on vein graphite demonstrate that Rockstone graphite exhibits a spectrum of structures, ranging from disordered to ordered at the nanometer scale (Figs. 4.10-4.12). The graphite displaying the highest degree of crystallinity is found in a vein with calcite fillings. Wopenka and Pasteris (1993) and Beyssac et al. (2002) demonstrated that graphite crystallinity increases with increasing temperature. The temperatures of up to 466°C obtained from Raman spectroscopy can be considered indicative of low- to medium-range temperature conditions for graphitization (Table 4.4). Additionally, graphite is mostly structurally disordered. These features are characterized by distortions within the graphene layers (e.g., dislocations and kink bands; Katagiri 1988; Wopenka and Pasteris, 1993; Palosaari et al., 2020). Notably, mechanical polishing of the samples can introduce structural disorders (Wopenka and Pasteris, 1993). The structural characteristics of Rockstone graphite resemble turbostratic carbon (T-carbon), which is characterized by random orientations of the graphite crystallites, such as distortions in the graphene layers (as demonstrated in Dr. Andrew Conly's previous XRD studies on Rockstone graphite, personal communication, 2025; Li et al., 2007; Conly and Moore 2015). The metasedimentary and metavolcanic rocks in the study area were affected by high strain deformation during D2 within the Shebandowan greenstone belt (Corfu and Stott, 1986; 1998). This deformation episode likely deformed

Rockstone graphite, characterized by turbostratic disorder within graphene layers (Corfu and Stott, 1998; Harris et al., 2023). Therefore, Rockstone graphite is turbostraticly deformed, most likely due to tectonic activity that enhanced porosity and permeability in shear zones (Fig. 5.5; Williams et al., 1991; Corfu and Stott, 1998; Pascal et al., 2016b; Harris et al., 2023).Taken together, Raman results are in good agreement with TEM data, indicating structural disorder in the graphite crystal structure.

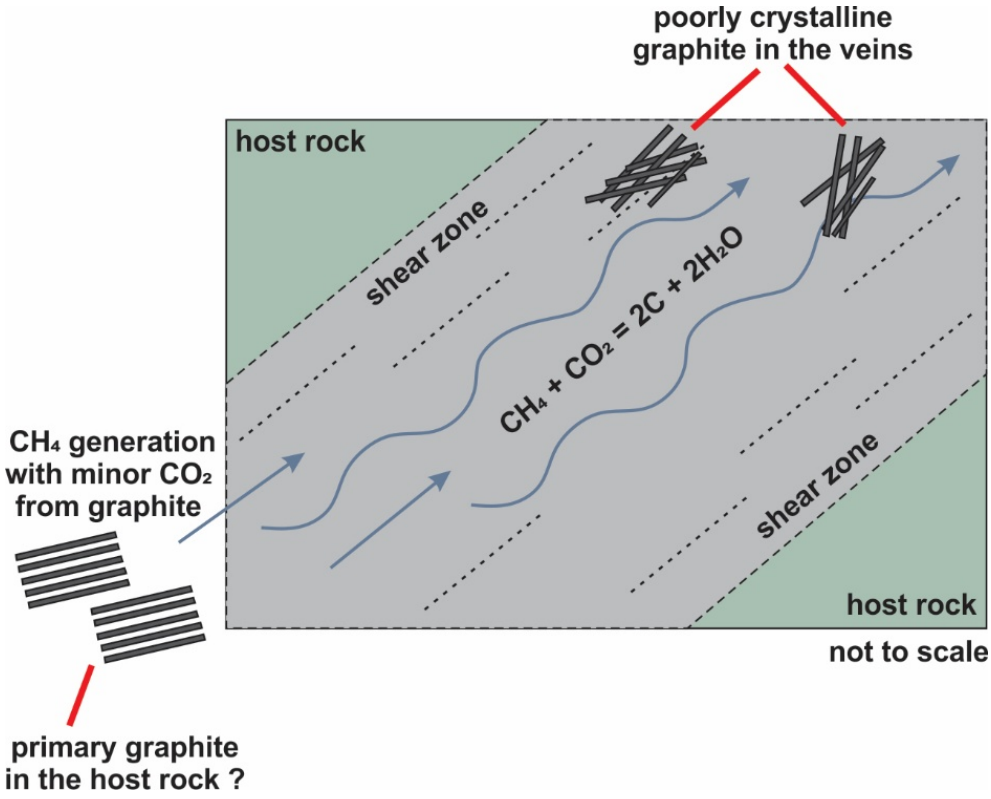

Figure 5.5: *A conceptual model for the formation of poorly crystalline graphite from potential primary graphite at depth in shear zones, which facilitate fluid migration along fractures to the surface via methane and carbon dioxide reactions in the host rock (modified from Upton & Craw, 2008, 2014).*

5.3) Implications for Geothermometry

Graphite formation in the Earth's crust typically occurs under greenschist to granulite facies metamorphism conditions, with pressures ranging from 0.5 to 3.5 GPa and temperatures

between 300°C and 750°C. However, in hydrothermal settings, graphite can also form at temperatures as low as 200°C (Pasteris and Wopenka, 1991; Luque et al., 1998; Beyssac et al., 2002).

The rocks in the Greenwater assemblage of the Shebandowan greenstone belt, which encompasses the study area, have undergone deformation and metamorphism at greenschist facies conditions, 250 to 450°C and 0.5 to 0.8 GPa (Beakhouse et al., 1996; Corfu and Stott, 1998; Sotiriou et al., 2019). Greenschist facies metamorphism of the graphite-bearing host rock is primarily indicated by mineral assemblages containing amphibole, epidote and chlorite. However, these determinations may not apply to all supracrustal rocks in the Shebandowan greenstone belt.

Three distinct geothermometers (Ti-in-biotite, chlorite and Raman) were applied to the Rockstone samples to estimate the peak metamorphic temperature and the crystallization temperatures of chlorite, biotite, and graphite. Ti-in-biotite temperatures in the host rock indicate peak, regional metamorphic temperature of ~500°C, the lower end of amphibolite facies metamorphism.

The crystallinity of graphite is primarily influenced by increasing metamorphic grade. As metamorphic grade increases, disordered carbon compounds evolve into more ordered carbon (Wopenka and Pasteris, 1993; Beyssac et al., 2002). Consequently, Raman derived temperatures on graphite provide information about peak metamorphic temperature. Raman data indicate that Rockstone graphite crystallized between 350°C and 466°C (±50°C), suggesting lower grade and/or retrograde metamorphic conditions than the Ti-in-biotite temperatures. Raman temperatures of vein graphite are variable, likely reflecting different degrees of crystallization due to deformation and/or metamorphic grade. However, these temperatures should be

interpreted with caution, as deformation can alter the band areas in the Raman shifts, thereby affecting temperature estimates (Kirilova et al., 2017). Therefore, Raman spectroscopy, derived temperatures may not accurately represent the temperature when graphite crystallized.

Two different chlorite geothermometers yielded comparable temperature estimates. Cathelineau and Nieva's (1985) empirical equation yielded temperatures ranging from 144° and 298°C (±25°C), with one exception of ~110°C. Similarly, Bourdelle et al. (2013) and Bourdelle and Cathelineau, (2015)'s semi-empirical equation produced temperatures between 112 and 280°C (±25°C). Although all chlorite geothermometers produced similar temperature ranges, the formulations of Bourdelle et al. (2013) and Bourdelle and Cathelineau (2015) are likely more accurate for estimating chlorite crystallization in the Rockstone context because they explicitly account for subtle compositional variations such as Si, Fe, Mg and Al content that influence chlorite stability and Bourdelle et al.'s equations do not account for ferric iron (Fe^{3+}) in its calculations, which is suitable for the reducing environment of the Rockstone property because of the presence of graphite. Cathelineau and Nieva's (1985) thermometer is more general and does not fully consider these compositional dependencies, which can lead to small but systematic differences in temperature estimates. Therefore, even if the overall ranges overlap, Bourdelle et al.'s equations are better calibrated as a graphical representation for the specific chemical characteristics of the chlorites in Rockstone.

In the host rock, crystallization temperatures of chlorite are significantly lower than those of biotite. This difference can be explained by petrographic observations showing that most of the biotite is altered to chlorite, likely during regional metamorphism accompanied by fluid infiltration and breakdown of higher-grade minerals (e.g., biotite).

Both chlorite geothermometers for vein chlorite produced temperatures of up to 300°C,

indicating greenschist facies metamorphic conditions. However, despite the limited reliability of Raman-based temperature estimates, they indicate peak metamorphic temperatures that are approximately 200°C higher than those indicated by chlorite geothermometers. The Rockstone graphite used for the Raman study is very fine-grained (~10–100 μm) and highly deformed, which hindered the identification of the crystallographic c-axis during Raman measurements. Consequently, this increased the uncertainty in the temperature calculations derived from the Raman data. Therefore, it can be concluded that this sample is not ideal for Raman analysis. However, given that the Ti-biotite temperatures reflect peak metamorphic temperature, both the Raman and chlorite temperatures imply overprinting low-grade metamorphic conditions.

In summary, based on the Ti-in-biotite thermometry (501-563 °C), Raman spectroscopy (350-466 °C), and chlorite geothermometry (144-298 °C), graphite formation most likely occurred after peak metamorphism, along a retrograde path, and in association with deformation. Graphite formation is post-peak, as the Raman-derived temperatures of graphite are lower than the peak metamorphic conditions indicated by Ti-in-biotite thermometry. Lower-temperature indicators (Raman and chlorite) and the likely structural nature of graphite (deformation during exhumation) suggests a retrograde path, meaning graphite formed while the rock was cooling and deforming after the peak metamorphism.

5.4) Origin of Rockstone Graphite Formation

In Precambrian low-grade metasedimentary rocks, graphite is generally considered to be coeval with sedimentation, given that the origin of carbon is typically organic (Schidlowski, 2001; Buseck and Beyssac, 2014). In the Rockstone study area, the presence of graphite, sulfides, and silicate-bearing veins along fractures (Fig 5.5) in the host rock suggests that graphite precipitation is epigenetic. Petrographic observations, including cryptocrystalline

fragments and vein graphite, support the epigenetic model for graphite mineralization at Rockstone.

Organic matter buried in anoxic, marine sediments, undergoes anaerobic decomposition, a process that primarily produces CH_4 with minor amounts of CO_2 as a byproduct (Fig. 5.6; Botz et al., 1996). This reaction can be described as (equation 14):

$$\mathbf{2CH_2O}_{\text{(organic matter)}} \rightarrow \mathbf{CH_4}_{\text{(methane)}} + \mathbf{CO_2}_{\text{(carbon dioxide)}} \qquad (14)$$

CH_4 and minor CO_2 might precipitate graphite in both the host rock and fractures during metamorphism and deformation, as described by reaction 15:

$$\mathbf{CH_4}_{\text{(methane)}} + \mathbf{CO_2}_{\text{(carbon dioxide)}} \rightarrow \mathbf{2C}_{\text{(graphite)}} + \mathbf{2H_2O}_{\text{(water)}} \qquad (15)$$

Following graphite formation, reactions (equation 16) between aqueous metamorphic fluids and graphite can lead to the release of CH_4-bearing fluids that migrate through fractures in the host rock and re-precipitate poorly crystalline graphite during episodes of tectonic activity (Fig. 5.5; Touret, 2001; Pascal et al., 2016a and reference therein):

$$\mathbf{2C}_{\text{graphite}} + \mathbf{2H_2O}_{\text{water}} \rightarrow \mathbf{CH_4}_{\text{(methane)}} + \mathbf{CO_2}_{\text{(carbon dioxide)}}. \qquad (16)$$

Considering the geology of the study area, specifically the protolith, the carbon and sulfur isotope results suggest a marine depositional environment with characteristics typical of VMS settings (e.g., abundant sulfides such as pyrite, sphalerite, pyrrhotite, chalcopyrite, and galena as well as Shebandowan gold mines in the surrounding region; Fig. 5.6).

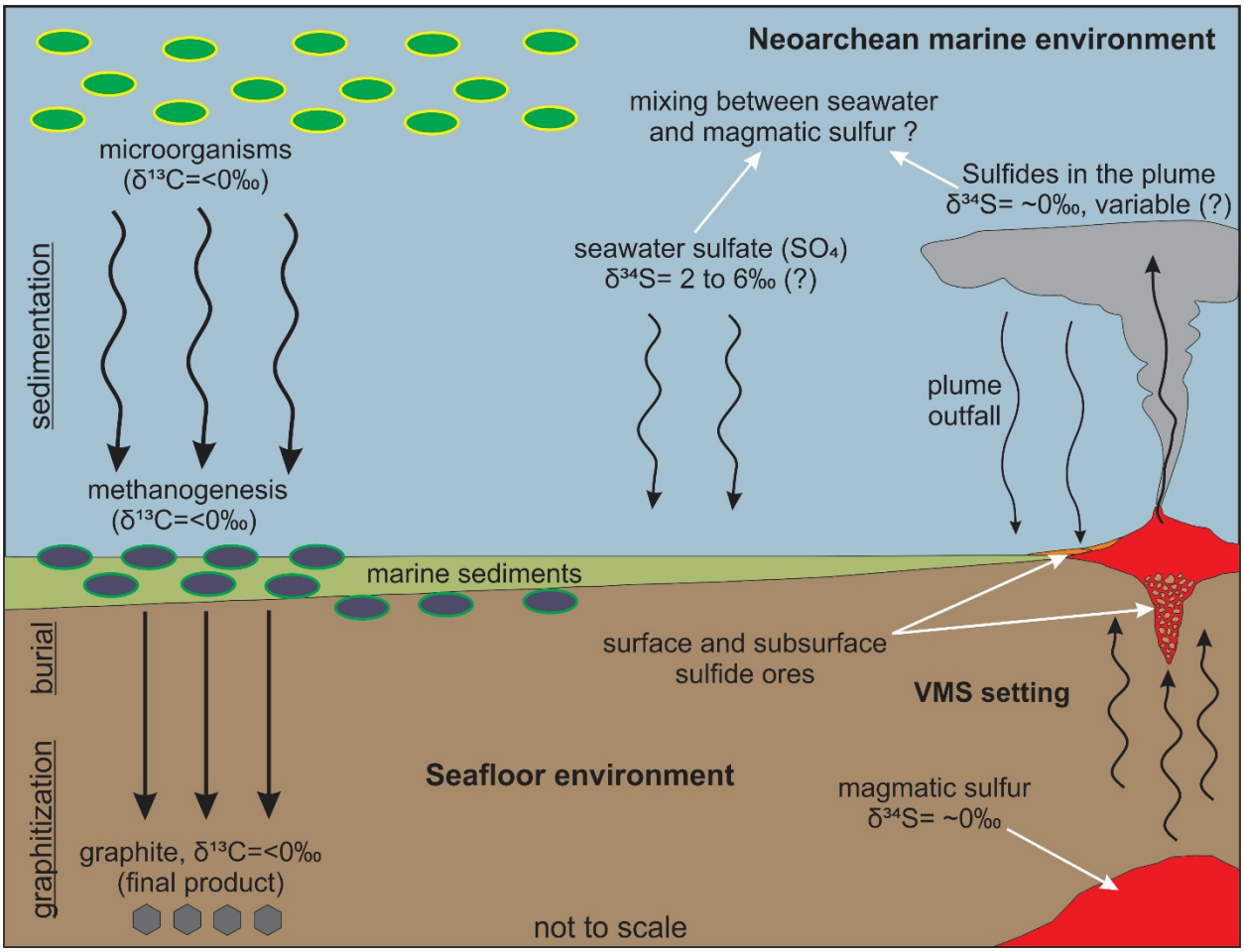

Figure 5.6: *Conceptual model illustrating the genesis of Rockstone graphite and associated sulfide minerals in a Neoarchean marine environment with characteristics of a volcanogenic massive sulfide (VMS) setting (modified from Massoth et al., 1988; Farquhar & Wing, 2003; Sharman et al., 2015). The $\delta^{34}S$ ratios of magmatic sulfur, VMS-related sulfides, and seawater sulfate are compiled from Hoefs (2009), Sharman et al. (2015), and Sharpe & Gemmell (2000), respectively.*

The strongly negative carbon isotope values further support the organic origin of carbon. Therefore, two processes are proposed for graphite formation. First, biogenic carbon was converted to graphite within the host rock during regional metamorphism, a process known as graphitization (Figs 5.2, 5.6; Buseck and Beyssac, 2014). Second, vein graphite, which is highly depleted in ^{13}C, may have formed from two main processes: (1) devolatilization of organic

matter during metamorphism, and/or (2) fluids transporting carbon from an existing graphite source at depth, during retrograde metamorphism (Fig. 5.5). During these processes, graphite precipitated in veins alongside silicates and sulfides. Devolatilization of organic matter during metamorphism is the dominant process that explains the isotopic composition and the precipitation of graphite (Luque et al., 2012). As a result of the devolatilization of organic matter, which is relatively depleted in ^{13}C, CH_4 is released into the geological environment during prograde metamorphism. This CH_4 is typically depleted in ^{13}C; consequently, the graphite precipitated from CH_4 within the veins is also characterized by low ^{13}C composition (Luque et al., 2012).

The poor crystallinity of the Rockstone graphite strengthens the possibility of crystallization at low temperatures, which are indicated by Raman temperatures (Wopenka and Pasteris, 1993; Luque et al., 2012). However, TEM study of Rockstone graphite revealed significant structural deformation. This deformation influences the Raman band regions (e.g., G and D peaks) that are essential to calculating Raman temperatures. Consequently, Raman derived temperatures of Rockstone graphite are most likely reflective of the deformation effects rather than solely thermal history (Kirilova et al., 2017). This deformation-related influence also provides a plausible explanation for the disordered crystalline structure, suggesting that the poor crystallinity is most likely consequence of deformation processes (Wopenka and Pasteris, 1993; Kirilova et al., 2017).

The association of hydrous minerals such as chlorite, muscovite and sericite with graphite and Ti-bearing minerals within the veins suggests that H_2O-rich fluids were involved in altering the original mineral assemblage (from reaction 2). Although the carbon isotope values (-6.5 to -5.6‰) of late calcite veins suggest a magmatic origin, the relatively ^{13}C-depleted signature of

CO_2, produced through reaction (3), may also have contributed to the formation of these calcite veins during metamorphism and deformation (Pascal et al., 2016a).

Papineau et al. (2011) reported highly depleted $\delta^{13}C$ values (-20.4 to -25.3‰) in graphite from the Eoarchean Nuvvuagittuq greenstone belt, Hudson Bay, northern Quebec. They concluded that such isotopic signatures do not fully represent organic carbon unless the graphite is demonstrably contemporaneous with the host rock. In addition, they noted that the graphite is poorly crystalline, and that Raman-derived temperatures of ~380 °C are significantly lower than the estimated peak metamorphic temperature of around 640 °C based on Ti-in-zircon thermometry for the host rock. Based on these findings, they concluded that the carbon in the Nuvvuagittuq graphite is unlikely to be of organic origin. However, Papineau et al. (2011) also acknowledged that graphite may have originally been organic and was later re-mobilized by fluids during metamorphism. This latter interpretation may also apply to the formation of Rockstone graphite.

Overall, the precipitation of Rockstone graphite in fractures of the host rock likely occurred contemporaneously with regional metamorphism and deformation. Graphite-chlorite-quartz veins typically precipitate by reactions of CH_4-rich metamorphic fluids. The alteration of biotite to chlorite in the host rock, and the formation temperatures derived geothermometrically for host rock chlorite, vein chlorite and graphite supports formation at low-grade metamorphic conditions.

CHAPTER 6 – CONCLUSIONS

The Rockstone graphite formation in Shebandowan greenstone belt of the Superior Province is little understood in terms of deposition and deformation history. However, the combination of petrographic, geothermometric and isotopic results here provide a robust framework for interpreting the geological history of Rockstone graphite and sulfides. Therefore, the following conclusions can be drawn within the scope of this research:

1- Graphite formation at Rockstone can be considered epigenetic, as indicated by petrographic observations showing graphite occurring primarily in cross-cutting vein textures within the host rock, an indicator commonly associated with epigenetic processes and the presence of hydrothermal minerals such as chlorite, muscovite and sulfide minerals (e.g., pyrite, sphalerite).

2- Graphite in the veins is fine-grained (~10 to 80 μm) and associated with chlorite, quartz, pyrite and sphalerite. As shown in the previous XRD results (A. Conly, personal communication, 2025), both Raman spectroscopy and TEM analyses in this study indicate that the graphite is structurally deformed. In particular, TEM reveals turbostratic disorder, including features such as dislocations and faulting between graphene layers.

3- An attempt was made to reconstruct the metamorphic history of graphite using temperatures derived from various geothermometers (Ti-in-biotite, chlorite and Raman). Therefore, temperature calculations on various minerals (biotite, chlorite and graphite) suggest that graphite formed during deformation and after peak metamorphism.

4- Both devolatilization and/or migration of organic carbon might be the main mechanism that precipitated graphite from metamorphic fluids in fractures of the host rock. Alternatively, the close association of graphite with chlorite, muscovite, and sulfide minerals such as pyrite and sphalerite within veins may suggest that graphite precipitation could also result from Fischer-

Tropsch (FT) reactions.

5- Highly depleted $\delta^{13}C$ data strongly suggest that the origin of carbon in the graphite is biogenic, and this depletion can be attributed to methanogenesis and devolatilization. Therefore, Rockstone graphite can be considered to represent relicts of early life forms in the Neoarchean.

6- $\delta^{34}S$ values of Rockstone sulfides typically reflect Archean signatures, suggesting that the sulfides originated from either magmatic or metamorphic fluids.

REFERENCES

Al-Ani, T., Ahtola, T., Cutts, K., & Torppa, A. (2022). Metamorphic evolution of graphite in the Paleoproterozoic Savo Schist Belt (SSB), Central Finland: constraints from geothermetric modeling. *Ore Geology Reviews, 141*, pp. 104-672.

Bajc, A.F. (1999). Results of regional humus and till sampling in the eastern part of the Shebandowan Greenstone Belt, northwestern Ontario, Ontario Geological Survey, Open File Report 5993.

Barber, D.J. (1981). Demountable polished extra-thin sections and their use in transmission electron microscopy. *Mineralogical Magazine 44*, pp. 357-359.

Barber, D.J. (1993). Radiation damage in ion-milled specimens: characteristics, effects, and methods of damage limitation. *Ultramicroscopy 52*, pp. 101-125.

Barnes John, H. (2003). Replacement of equipment in survey lab means new capabilities. *Pennsylvania Geology 33 (3),* pp. 2-12.

Barrenechea, J.M., Luque, F.J., Millward, D., Ortega, L., Beyssac, O., & Rodas, M. (2009). Graphite morphologies from the Borrowdale deposit (NW England, UK): Raman and SIMS data. *Contributions to Mineralogy and Petrology*, 158, pp. 37-51.

Beakhouse, G.P., Stott, G.M., Blackburn, C.E., Breaks, F.W., Ayer, J., Stone, D., Farrow, C. & Corfu, F. (1996). Western Superior Province-Field Trip Guidebook A5/B6, Geological Association of Canada Annual Meeting, Winnipeg, Manitoba, May 27-29, 1996.

Berger, B.R. (1993). Geology of Adrian and Marks townships; Ontario Geological Survey, Open File Report 5862, 90pp.

Bernal, J.D. (1924). The structure of graphite. Proceedings of the Royal Society London A 106, pp. 749–773.

Beyssac, O., Goffe, B., Chopin, C. & Rouzaud, J.N. (2002). Raman spectra of carbonaceous material in metasediments: a new geothermometer. *Journal of Metamorphic Geology*. 20, pp. 859‑871.

Beyssac, O., & Rumble, D. (2014). Graphitic carbon: a ubiquitous, diverse, and useful geomaterial. *Elements, 10*, pp. 415-420.

Blackburn, C.E., Johns, G.W., Ayer, I. & Davis, D.W. (1991). Wabigoon subprovince; in Geology of Ontario, Ontario Geological Survey, Special Volume 4, Part 1, pp. 303-381.

Blackadar, R.G. (1956). Differentiation and assimilation in the Logan sills, Lake Superior district, Ontario; *American Journal of Science, 254*, pp. 623-645.

Bourdelle, F., Parra, T., Chopin, C. & Beyssac, O. (2013). A new chlorite geothermometer for diagenetic to low-grade metamorphic conditions. *Contribution Mineralogy and Petrology 165 (4)*, pp. 723–735.

Bourdelle, F. & Cathelineau, M. (2015). Low-temperature chlorite geothermometry: a graphical representation based on a T–R2+–Si diagram. *European Journal of Mineralogy 27 (5)*, pp. 617–626.

Bourdelle, F. (2021). Low-temperature chlorite geothermometry and related recent analytical advances: a review. *Minerals 11*, 130. https://doi.org/10.3390/min11020130.

Bottinga, Y. (1969). Calculated fractionation factors for carbon and hydrogen isotope exchange in the system calcite–carbon dioxide– graphite–methane–hydrogen–water vapor. *Geochimica Cosmochimica Acta* 33: pp. 49–64. doi:10.1016/0016-7037(69)90092-1

Botz, R., Pokojski, H., Schmitt, M., & Thomm, M. (1996). Carbon isotope fractionation during bacterial methanogenesis by CO2 reduction. *Organic Geochemistry*, 25, pp. 255-262.

Bucher, K., & Grapes, R. (2011). *Petrogenesis of Metamorphic Rocks* (8th ed.). Springer. 441 pp.

Bucholz, C.E., Biasi, J.A., Beaudry, P., & Ono, S. (2020). Sulfur isotope behavior during metamorphism and anatexis of Archean sedimentary rocks: A case study from the Ghost Lake batholith, Ontario, Canada. *Earth and Planetary Science Letters*, 549, 116494.

Buseck, P. R. (1983). Electron microscopy of minerals. American Scientist, 71(2), 175-185.

Buseck, P.R. & Beyssac, O. (2014). From Organic Matter to Graphite: Graphitization. Elements 10 (6): pp. 421–426. doi: https://doi.org/10.2113/gselements.10.6.421.

Cameron, E.M. (1983). Genesis of Proterozoic iron-formation: sulphur isotope evidence. *Geochimica et Cosmochimica Acta*, 47, pp. 1069-1074.

Card, K.D. & Ciesielski, A. (1986). DNAG #1. Subdivisions of the Superior Province of the Canadian Shield; Geoscience Canada, v. 13, pp. 5-13.

Caritat, P., Hutcheon, I. & Walshe, J. L. (1993). Chlorite geothermometry: a review. *Clays and Clay Minerals 41(2)*, pp. 219–239. doi:10.1346/CCMN.1993.0410210.

Carter, M.W. (1990). Geology of Goldie and Horne Townships, Ontario Geological Survey, Open File Report 5720.

Case, G.N.D., Karl, S.M., Regan, S.P. *et al.* (2023). Insights into the metamorphic history and origin of flake graphite mineralization at the Graphite Creek graphite deposit, Seward Peninsula, Alaska, USA. *Mineralium Deposita 58*, pp. 939–962. https://doi.org/10.1007/s00126-023-01161-3

Cathelineau, M. & Nieva, D. (1985). A chlorite solid solution geothermometer. The Los Azufres (Mexico) geothermal system: *Contributions to Mineralogy and Petrology 91*, pp. 235-244.

Cathelineau, M. (1988). Cation site occupancy in chlorites and illites as a function of temperature *Clay Minerals 23*, pp. 471-485.

Chen L, Xu J. & Chen J. (2015). Applications of scanning electron microscopy in earth sciences. *Science China: Earth Sciences 58*: pp. 1768–1778, doi:10.1007/s11430-015-5172-9.

Chorlton, L. (1987). Geological setting of gold mineralization in the western part of the Shebandowan greenstone belt, District of Thunder Bay, northwestern Ontario; Ontario Geological Survey, Open File Report 5636, 348pp.

Conly, A.G. & Moore, L.C. (2015). Geology, ore characteristics, and origin of the Albany graphite deposit. In: Simandl, G.J. and Neetz, M., (Eds.), Symposium on Strategic and Critical Materials Proceedings, November 13-14, 2015, Victoria, British Columbia. British Columbia Ministry of Energy and Mines, British Columbia Geological Survey Paper 2015-3, pp. 173-185.

Corfu, F. & Stott, G.M. (1986). U–Pb ages for late magmatism and regional deformation in the Shebandowan belt, Superior Province, Canada; *Canadian Journal of Earth Sciences, 23*, pp. 1075–1082.

Corfu, F. & Stott, G.M. (1998). Shebandowan greenstone belt, western Superior Province: U/Pb ages, tectonic implications, and correlations; *Geological Society of America Bulletin, 110*, pp. 1467-1484.

Coueslan, C.G. (2023). Affinity and petrogenesis of the Huzyk Creek metal-enriched graphite deposit: A metamorphosed metalliferous black shale in the Trans-Hudson Orogen of Manitoba, Canada. *The Canadian Mineralogist 60 (6)*, pp. 853–880. doi: https://doi-org.uml.idm.oclc.org/10.3749/canmin.2100001.

Cullen, D. & Garry Clark, J. (2014). Technical report on the Rockstone Property, Thunder Bay Mining Division, northwestern Ontario. Clark Exploration Consulting for Deveron Resources Ltd., Thunder Bay, Ontario; URL <https://www.sedarplus.ca/csa-party/records/document.html?id=212f9507378fac7c3dc2fc8448576a398cc359602d9170f9461b856a4c79b757> October 2024, 32pp.

Crespo, E., Luque, J., Fernandez-Rodriguez, C., Rodas, M., Diaz-Azpiroz, M., Fernandez-Caliani & J.C., Barrenechea, J.F. (2004). Significance of graphite occurrences in the Aracena Metamorphic Belt, Iberian Massif. *Geological Magazine* 141, pp. 687-697.

Crowe, D.E., & Vaughan, R.G. (1996). Characterization and use of isotopically homogeneous standards for in situ laser microprobe analysis of 34S/32S ratios. *American Mineralogist*, 81, pp. 187 - 193.

Deines, P., Harris, J.W., Robinson, D.N., Gurney, J.J., & Shee, S.R. (1991). Carbon and oxygen isotope variations in diamond and graphite eclogites from Orapa, Botswana, and the nitrogen content of their diamonds. *Geochimica et Cosmochimica Acta*, 55, pp. 515-524.

Deines, P. (2002). The carbon isotope geochemistry of mantle xenoliths. *Earth-Science Reviews 58*, pp. 247–278.

Dissanayake, C. B. (2013). Origin of vein graphite in high-grade metamorphic terrains. Role of organic matter and sediment subduction. *Mineralium Deposita, 29 (1)*, pp. 57–67, https://doi.org/10.1007/BF03326396.

Drever, C., Kinney, C., & Yakymchuk, C. (2023). Petrogenesis of extra-large flake graphite at the Bissett Creek deposit, Canada. *Mineralium Deposita 584*, pp. 731-750. doi:10.1007/s00126-022-01145-9.

Duke, E.F., & Rumble, D.I. (1986). Textural and isotopic variations in graphite from plutonic rocks, South-Central New Hampshire. *Contributions to Mineralogy and Petrology*, 93, pp. 409-419.

Dunn, S.R. & Valley, J.W. (1992). Calcite-graphite isotope geothermometry: a test for polymetamorphism in marble, Tudor gabbro aureole, Ontario, Canada. *Journal of Metamorphic Geology* 10, 487e501.

Engvik, A.K., Gautneb, H., Mørkved, P.T., Solberg, J.K., & Erambert, M. (2023). Proterozoic deep carbon—characterisation, origin and the role of fluids during high-grade metamorphism of graphite (Lofoten–Vesterålen Complex, Norway). *Minerals 13(10)*: 1279. https://doi.org/10.3390/min13101279.

European Commission. (2020). Critical raw materials resilience: charting a path towards greater security and sustainability. Document 52020DC0474, COM/2020/474 final.

Farquhar, J., & Wing, B.A. (2003). Multiple sulfur isotopes and the evolution of the atmosphere. *Earth and Planetary Science Letters*, 213, pp. 1-13.

Faure, G. and Mensing, T.M. (2005). Isotope Principle and Applications. 3rd Edition, John Wiley & Sons, Hoboken. 928 pp.

Foster, M.D. (1960). Interpretation of composition of trioctahedral micas. U. S. Geological Survey. Prof. Pap. 354B, pp. 1–49. https://doi.org/10.3133/pp354B.

Franklin, J.M., Gibson, H.L., Jonasson, I.R., Galley, A.G. (2005). Volcanogenic massive sulfide deposits. In: Hedenquist, JW, Thompson JFH, Goldfarb RJ, Richards JP (eds) Economic geology 100th Anniversary Volume, *Society of Economic Geologists*, Inc. Littleton, CO, pp 523–560.

Freise, E. J. & A. Kelly. (1963). The deformation of graphite crystals and the production of the rhombohedral form, *Philosophical Magazine 8:93*, pp. 1519-1533, DOI: 10.1080/14786436308207315

Galvez, M., Beyssac, O., Martinez, I., Benzerara, K., Chaduteau, C., Malvoisin, B. and Malavieille, J. (2013). Graphite formation by carbonate reduction during subduction. *Nature Geoscience* 6, pp. 473–477. https://doi org.uml.idm.oclc.org/10.1038/ngeo1827

Goldstein, J., Newbury, D.E., Joy, D.C., Lyman, C.E., Echlin, P., Lifshin, E., Sawyer, L. & Michael, J.R. (2007). Scanning Electron Microscopy and X-Ray Microanalysis: Third Edition. Springer. 550 pp.

Gautneb, H., & Tveten, E. (2000). The geology, exploration and characterisation of graphite deposits in the Jennestad area, Vesteralen, northern Norway. *Ngu-Bull* 436, pp. 67-74.

Hahn-Weinheimer, P., & Hirner, A. (1981). Isotopic evidence for the origin of graphite. Geochemical Journal 15, pp. 9-15.

Harris, J.R., Ayer, J., Naghizadeh, M., Smith, R., Snyder, D., Behnia, P., Parsa, M., Sherlock, R., Trivedi, M. (2023). A study of faults in the Superior province of Ontario and Quebec using the random forest machine learning algorithm: spatial relationship to gold mines. *Ore Geology Reviews 157*, pp. 17. https://doi.org/10.1016/j.oregeorev.2023.105403

Hart, T.R. (2007). Geochronology of the Hamlin and Wye Lakes Area, Shebandowan Greenstone Belt, Thunder Bay District, Summary of Field Work and Other Activities, Open File Report 6213. Ontario Geological Survey, pp. 9-1 to 9-8.

Hewitt, D.F. (1965). Graphite in Ontario. Ontario Department of Mines, Industrial Mineral Report No. 20, 66 pp.

Hey, M.H. (1954). A new review of the chlorites. *Mineralogical magazine and journal of the Mineralogical Society 30*, pp. 277–292.

Hoefs, J. (2009). Stable Isotope Geochemistry. 6th Edition, *Springer-Verlag*, Berlin Heidelberg. 285p.

Horita, J. (2005). Some perspectives on isotope biosignatures for early life. *Chemical Geology*, 218, pp. 171-186.

Hu, H., Zhang, L., Lan, C. & Liu, Z. (2023). Petrological evidence for deep subduction of organic carbon to subarc depths. *Communications Earth & Environment 4*, 418. https://doi.org/10.1038/s43247-023-01085-w.

Huston, D.L., Pehrsson, S., Eglington, B.M. & Zaw, K. (2010). The geology and metallogeny of volcanic-hosted massive sulfide deposits: variations through geologic time and with tectonic setting. *Economic Geology*, 105:571.

Jamieson, J.W., Wing, B.A., Hannington, M.D. & Farquhar, J. (2006). Evaluating isotopic equilibrium among sulfide mineral pairs in Archean ore deposits: case study from the Kidd Creek VMS deposit, Ontario, Canada. *Economic Geology*, 101: pp. 1055–1061

Jobin-Bevans, S., Kelso, I. & Cullen, D. (2006). NI 43-101 Technical report on the Tower Mountain gold deposit, Conmee Township, northwestern Ontario, Canada for ValGold Resources Ltd., 95pp.

Johnston, D.T. (2011). Multiple sulfur isotopes and the evolution of Earth's surface sulfur cycle. *Earth-Science Review*, 106: pp. 161–183.

Jones, N.W. (1984). Petrology of some Logan diabase sills, Cook County, Minnesota; Minnesota Geological Survey, Report of Investigations 29, 40pp.

Katagiri, G., Ishida, H., & Ishitani, A. (1988). Raman spectra of graphite edge planes. *Carbon*, 26, pp. 565-571.

Kehlenbeck, M.M. (1988). A fault-bounded outlier of Archean clastic rocks near Thunder Bay, Ontario; *Canadian Journal of Earth Sciences, 25*, pp.152-156.

King, R.J. (2006). "Minerals explained 43: Graphite," in Geology Today 22-2, Blackwell Publishing Inc., pp. 71–77.

Kirilova, M., Toy, V.G., Rooney, J.S., Giorgetti, C., Gordon, K.C., Collettini, C., & Takeshita, T. (2017). Structural disorder of graphite and implications for graphite thermometry. *Solid Earth*, 9, pp. 223-231.

Kita, N.T., Huberty, J.M., Kozdon, R., Beard, B.L., & Valley, J.W. (2011). High-precision SIMS oxygen, sulfur and iron stable isotope analyses of geological materials: accuracy, surface topography and crystal orientation. *Surface and Interface Analysis*, 43, 5pp.

Kranidiotis, P. & MacLean, W.H. (1987). Systematics of chlorite alteration at the Phelps Dodge massive sulphide deposit, Matagami, Quebec. Economic Geology 82, pp. 1898-191.

Kwiecinska, B. (1978). On the rhombohedral modifications in natural graphite and semi-graphites. *Mineralogia Polonica 9*, pp. 3–12.

Kwiecinska, B., & Petersen, H.J. (2004). Graphite, semi-graphite, natural coke and natural char classification-ICCP system. *The International Journal of Coal Geology 57*, pp. 99–116.

Kwiecinska, B., Pusz, S. & Valentine, B.J. (2019). Application of electron microscopy TEM and SEM for analysis of coals, organic-rich shales and carbonaceous matter. *International Journal of Coal Geology 211,* 13pp.

Landis, C. A. (1971). Graphitization of dispersed carbonaceous material in metamorphic rocks. *Contributions to mineralogy and petrology 30(1)*, pp. 34-45.

Laves, F., & Baskin, Y. (1956). On the Formation of the Rhombohedral Graphite Modification. *Zeitschrift für Kristallographie, 107(5-6)*, pp. 337-356. https://doi.org/10.1524/zkri.1956.107.5-6.337

Lee, M. R. (2010). Transmission electron microscopy (TEM) of Earth and planetary materials: a review. *Mineralogical Magazine 74(1),* pp. 1–27. doi:10.1180/minmag.2010.074.1.1.

Li, Z. Q., Lu, C. J., Xia, Z. P., Zhou, Y., & Luo, Z. (2007). X-ray diffraction patterns of graphite and turbostratic carbon. *Carbon, 45(8)*, pp. 1686-1695.

Lipson, H., & Stokes, A.R. (1942). The structure of graphite. Proceedings of the Royal Society London A 181, pp. 101–105.

Liu, R., Hull, S., & Fayek, M. (2011). A new approach to measuring D/H ratios with the CAMECA IMS-7F. *Surface and Interface Analysis* 43, pp. 458–461. DOI: 10. 1002/sia.3467

Lodge, R.W.D., Gibson, H.L., Stott, G.M., Hundak, G.J., Jirsa, M.A. & Hamilton, M.A. (2013). New U–Pb geochronology from Timiskaming-type assemblages in the Shebandowan and Vermilion greenstone belts, Wawa subprovince, Superior Craton: Implications for the Neoarchean development of the southwestern Superior Province. *Precambrian Research 235*, pp. 264-277.

Lodge, R.W.D., Gibson, H.L., Stott, G.M., Franklin, J.M. & Hudak, G.J. (2015). Geodyamic setting, crustal architecture, and VMS metallogeny of ca. 2720 Ma greenstone belt assemblages of the northern Wawa subprovince, Superior Province. *Canadian Journal of Earth Science 52*, pp. 196–214.

Luque, F. J., Barrenechea, J. F., & Rodas, M. (1993). Graphite geothermometry in low and high temperature regimes: two case studies. *Geological Magazine, 130(4)*, pp. 501–511. doi:10.1017/S0016756800020562

Luque, F.J., Pasteris, J.D., Wopenka, B., Rodas, M. & Barrenechea, J.F. (1998). Natural fluid deposited graphite: mineralogical characteristics and mechanisms of formation. *American Journal of Science* 298, 471e498. pp. 471-498.

Luque, F.J., Crespo-Feo, E., Barrenechea, J.F., & Ortega, L. (2012). Carbon isotopes of graphite: implications on fluid history. *Geoscience Frontiers 3*, pp. 197–207.

Luque, F.J., Huizenga, J.-M., Crespo-Feo, E., Wada, H., Ortega, L., & Barrenechea, J.F. (2014). Vein graphite deposits: geological settings, origin, and economic significance. *Mineralium Deposita 49*, pp. 261–277.

Martin, A. J., Jamieson, J. W., Petersen, S., Fayek, M., & Escartin, J. (2024). Fluid flow, mineralization and deformation in an oceanic detachment fault: Microtextural, geochemical and isotopic evidence from pyrite at 13°30'N on the Mid-Atlantic Ridge. *Geochemistry, Geophysics, Geosystems*, *25*, e2023GC011033. https://doi.org/10.1029/2023GC011033.

Massoth, G.J., Milburn, H.B., Hammond, S.R., Butterfield, D.A., McDuff, R.E., Lupton, J.E. (1988). The geochemistry of submarine venting fluids at Axial Volcano, Juan de Fuca Ridge; new sampling methods and a vents program rational. In: Deluca MP, Babb I (eds) Global venting, midwater, and benthic ecological processes (88–4). *National Undersea Research Program Report*, Rockville, MD, pp. 29–59

Morikiyo, T. (1986). Hydrogen and carbon isotope studies on the graphite-bearing metapelites in the northern Kiso district of central Japan. *Contributions to Mineralogy and Petrology* 94: pp. 165‑177.

Muller, D.A. (2009). Structure and bonding at the atomic scale by scanning transmission electron microscopy. *Nature Materials 8*, pp. 263-270.

Nabelek, P.I., Wilke, M., Huff, T.A. & Wopenka, B. (2003). Methane, an important component of fluids in graphitic metapelites. *Geochimica et Cosmochimica Acta* Supplement 67, 317.

National Minerals Information Center. (2024). U.S. Geological Survey mineral commodity summaries 2024 Data Release (ver. 2.0, March 2024): U.S. Geological Survey data release, https://doi.org/10.5066/P144BA54.

Natural Resources Canada. (2023). Critical Minerals. https://www.canada.ca/en/campaign/critical-minerals-in-canada/critical-minerals-an-opportunity-for-canada.html. Accessed 17 Dec 2023.

O'Keefe, M.A. (2008). Seeing atoms with aberration corrected sub-Angstrom electron microscopy. *Ultramicroscopy 108*, 1 pp. 96-209.

Ohmoto, H., & Rye, R.O. (1979). Isotopes of sulfur and carbon, In Barnes HL (ed) *Geochemistry of hydrothermal ore deposits*, 2d ed. Wiley, New York, pp. 509-567.

Ohmoto, H. (1996). Formation of volcanogenic massive sulfide deposits: The Kuroko perspective. *Ore Geology Reviews*, 10, pp. 135-177.

Ohtomo, Y., Kakegawa, T., Ishida, A., Nagase, T., & Rosing, M.T. (2014). Evidence for biogenic graphite in early Archaean Isua metasedimentary rocks. *Nature Geoscience*, 7, pp. 25-28.

Ortega, L., Millward, D., Luque, F. J., Barrenechea, J. F., Beyssac, O., Huizenga, J. M., Rodas, M., Clarke, S. M. (2010). The graphite deposit at Borrowdale (UK): a catastrophic mineralizing event associated with Ordovician magmatism. *Geochimica et Cosmochimica Acta*, *74*(8), pp. 2429-2449.

Osmani, I. A. (1997). Geology and mineral potential: Greenwater Lake area, west-central Shebandowan greenstone belt: Ontario Geological Survey Report 296, 135pp.

Pearson D.G., Boyd, F.R., Haggerty, S.E., Pasteris, J.D., Field, S.W., Nixon, P.H. & Pokhilenko, N.P., 1994, The characterization of graphite in cratonic lithospheric mantle: A petrological carbon isotope and Raman spectroscopic study: *Contributions to Mineralogy and Petrology*, v. 115, pp. 449–466

Palosaari, J., Latonen, R., Smått, J., Raunio, S. & Eklund, O. (2020). The flake graphite prospect of Piippumäki—an example of a high-quality graphite occurrence in a retrograde metamorphic terrain in Finland. *Mineralium Deposita*, pp. 1-14.

Parnell, J., Brolly, C., & Boyce, A. J. (2021). Mixed metamorphic and fluid graphite deposition in Palaeoproterozoic supracrustal rocks of the Lewisian Complex, NW Scotland. *Terra Nova, 33*, pp. 541–550. https://doi.org/10.1111/ter.12546

Pascal, M., Ansdell, K. M. & Annesley, I. R. (2015). Graphite-bearing and graphite-depleted basement rocks in the Dufferin Lake zone, south-central Athabasca Basin, Saskatchewan. *Geological Survey of Canada,* Open File*, 7791*, pp. 83-92. https://doi.org/10.4095/295786

Pascal, M., Boiron, M.-C., Ansdell, K., Annesley, I.R., Kotzer, T., Jiricka, D., & Ciney, M. (2016a). Fluids preserved in variably altered graphitic pelitic schists in the Dufferin Lake zone, south-central Athabasca Basin, Canada: Implications for graphite loss and uranium deposition. Mineralium Deposita, DOI 10.1007/s00126-015-0628-6.

Pascal, M., Ansdell, K., Annesley, I.R., Kotzer, T., & Jiricka, D. (2016b). Graphite-Bearing Pelitic Schists and Their Altered Equivalents in the Dufferin Lake Zone, South-Central Athabasca Basin, Saskatchewan: Constraints on Graphite Formation and Destruction, and Implications for Uranium Mineralization. *Canadian Mineralogist*, 54, pp. 1459-1491.

Pasteris, J.D. & Wopenka, B. (1991). Raman spectra of graphite as indicators of degree of metamorphism. *Canadian Mineralogist 29*, pp. 1-9.

Papineau, D., Gregorio, B.T., Cody, G.D., O'Neil, J., Steele, A., Stroud, R.M., & Fogel, M.L. (2011). Young poorly crystalline graphite in the >3.8-Gyr-old Nuvvuagittuq banded iron formation. *Nature Geoscience*, 4, pp. 376-379.

Percival, J.A. (2007). Geology and metallogeny of the Superior Province, Canada. In Mineral Resources of Canada: A Synthesis of Major Deposit Types, District Metallogeny, the Evolution of Geological Provinces, and Exploration Methods. Edited by W.D. Goodfellow. Geological Association of Canada, Mineral Deposits Division, Special Publication No. 5, pp. 903–928

Percival, J.A., & Easton, R.M. (2007). Geology of the Canadian Shield in Ontario: an update; Ontario Geological Survey, Open File Report 6196, Geological Survey of Canada, Open File 5511, Ontario Power Generation, Report 06819-REP-01200-10158-R00, 65p.

Percival, J.A., Skulski, T., Sanborn-Barrie, M., Stott, G.M., Leclair, A.D., Corkery, M.T., & Boily, M. (2012). Geology and tectonic evolution of the Superior Province, Canada. Chapter 6 In Tectonic Styles in Canada: The LITHOPROBE Perspective. Edited by J.A. Percival, F.A. Cook, and R.M. Clowes. *Geological Association of Canada*, Special Paper 49, pp. 321–378.

Philpotts, A. R., & Ague, J. J. (2022). Principles of Igneous and Metamorphic Petrology (3rd ed.). Cambridge: *Cambridge University Press.* 774p.

Polat, A. (2009). The geochemistry of Neoarchean (ca. 2700 Ma) tholeiitic basalts, transitional to alkaline basalts, and gabbros, Wawa Subprovince, Canada: Implications for petrogenetic and geodynamic processes. *Precambrian Research 168*, pp. 83-105.

Rahl, J.M., Anderson, K.M., Brandon, M. & Fassoulas, C. (2005). Raman spectroscopic carbonaceous material thermometry of low-grade metamorphic rocks: Calibration and application to tectonic exhumation in Crete, Greece. *Earth and Planetary Science Letter*, pp. 240, 339‑354.

Rantitsch, G., Lammerer, W., Fisslthaler, E., Mitsche, S. & Kaltenbock, H. (2016). On the discrimination of semi-graphite and graphite by Raman spectroscopy. *International Journal of Coal Geology 159*, pp. 49–56.

Ren, Y., Li, J., Sun, X., Li, Z., & Sun, Z. (2022). Genesis of metal sulfides and its significance on graphite mineralization in the Huangyangshan graphite deposit, East Junggar, Xinjiang Province, China. *Minerals, 12*, 1450. https://doi.org/10.3390/min12111450.

Reynolds, W.N. (1968). Physical Properties of Graphite. Materials Science Series, Elsevier, Amsterdam, 193 pp.

Riciputi, L.R., Paterson, B.A., & Ripperdan, R. (1998). Measurement of light stable isotope ratios by SIMS: Matrix effects for oxygen, carbon, and sulfur isotopes in minerals. *International Journal of Mass Spectrometry*, 178, pp. 81-112.

Rieder, M., Cavazzini, G., D'Yakonov, Y.S., Frank-Kamenetskii, V.A., Gottardi, G., Guoggenheim, S., Koval, P.V., Müller, G., Neiva, A.M.R., Radoslovich, E.W., et al. (1998). Nomenclature of the micas. *Canadian Mineralogist* 36, pp. 905–912.

Roberts, S., Tricker, P.M. & Marshall, J.E.A. (1995). Raman spectroscopy of chitinozoans as a maturation indicator. *Organic Geochemistry*, 23, pp. 223‑228.

Robinson, G.R., Jr., Hammarstrom, J.M., & Olson, D.W. (2017). Graphite, chap. J of Schulz, K.J., DeYoung, J.H., Jr., Seal, R.R., II, and Bradley, D.C., eds., Critical mineral resources of the United States—Economic and environmental geology and prospects for future supply: U.S. Geological Survey Professional Paper 1802, pp. J1–J24, https://doi.org/10.3133/pp1802J.

Rogers, M.C. & Berger, B.R. (1995). Precambrian geology, Adrian, Marks, Sackville, Aldina and Duckworth townships; Ontario Geological Survey, Report 295, 66p.

Sage, R.P., Lightfoot, P.C. & Doherty, W. (1996). Bimodal cyclical Archean basalts and rhyolites from the Michipicoten (Wawa) greenstone belt, Ontario; Geochemical evidence for magma contributions from the asthenospheric mantle and ancient continental lithosphere near the southern margin of the Superior Province: *Precambrian Research 76*, pp. 119-153.

Santaguida, F. (2001). Precambrian geology compilation series – Thunder Bay sheet. Ontario Geological Survey, Map 2664, 1:250,000.

Santos, F.H., da Silva Amaral, W., Filho, E.C., de Andrade Caxito, F., Souza, A.C., Martins, D.T., & de Andrade Feitosa, B. (2024). The origin and fate of organic carbon in graphite–manganese bearing rocks and implications for the Lomagundi–Jatuli Event. *Scientific Reports*, 14p.

Schneiders, B.R., Scott, J.F. & Smyk, M.C. (1998). Report of Activities, 1997, Resident Geologist Program, Thunder Bay South Regional Resident Geologist's Report: Thunder Bay South District; Ontario Geological Survey, Open File Report 5971, 56 pp.

Schoell, M. &Wellmer, FW. (1981). Anomalous ^{13}C depletion in early Precambrian graphites from Superior Province, Canada. *Nature* 290, pp. 696–699 https://doi.org/10.1038/290696a0

Schidlowski, M. (1988). Application of stable carbon isotopes to early biochemical evolution on Earth. *Annual Reviews Earth and Planetary Sciences 15*, pp. 47-72.

Schidlowski, M. (2001). Carbon isotopes as biogeochemical recorders of life over 3.8 Ga of Earth history: evolution of a concept. *Precambrian Research 106*, pp. 117–134.

Sharman, E.R., Taylor, B.E., Minarik, W.G., Dubé, B., & Wing, B.A. (2015). Sulfur isotope and trace element data from ore sulfides in the Noranda district (Abitibi, Canada): implications for volcanogenic massive sulfide deposit genesis. *Mineralium Deposita*, 50, pp. 591-606.

Sharpe, R., & Gemmell, J.B. (2000). Sulfur isotope characteristics of the Archean Cu–Zn Gossan Hill VHMS deposit, Western Australia. *Mineralium Deposita*, 35, pp. 533-550.

Sharpe, R. (2013). The geochemistry and geochronology of the Bong uranium deposit, Thelon basin, Nunavut, Canada. M.Sc. thesis, University of Manitoba. http://hdl.handle.net/1993/18485.

Sheahan, M. Fayek, D. Quirt, C. & W. Jefferson. (2016). A Combined Ingress-Egress Model for the Kianna Unconformity-Related Uranium Deposit, Shea Creek Project, Athabasca Basin, Canada. *Economic Geology*; 111 (1): pp. 225–257. doi: https://doi.org/10.2113/econgeo.111.1.225

Shegelski, R.J. (1980). Archean cratonization, emergence and red bed development, Lake Shebandowan area, Canada. *Precambrian Research 12*, pp. 331–347.

Simandl, G. J., Paradis, S., & Akam, C. (2015). Graphite deposit types, their origin, and economic significance. *British Columbia Ministry of Energy and Mines & British Columbia Geological Survey*, 3, pp. 163-171.

Slotznick, S.P., & Fischer, W.W. (2016). Examining Archean methanotrophy. *Earth and Planetary Science Letters*, 441, pp. 52-59.

Song, H., Chi, G., Wang, K., Li, Z., Bethune, K.M., Potter, E.G., & Liu, Y. (2022). The role of graphite in the formation of unconformity-related uranium deposits of the Athabasca Basin, Canada: A case study of Raman spectroscopy of graphite from the world-class Phoenix uranium deposit. *American Mineralogist 107 (11)*, pp. 2128–2142. doi: https://doi-org.uml.idm.oclc.org/10.2138/am-2022-8158.

Sotiriou, P., Polat, A., & Frei, R. (2019). Petrogenesis and geodynamic setting of the Neoarchaean Haines Gabbroic Complex and Shebandowan greenstone belt, southwestern Superior Province, Ontario, Canada. *Lithos*. pp. 324–325

Spence, H.S. (1920). Graphite. Department of Mines, Canada, Publication No. 511, 250 pp.

Strauss, H. (1986). Carbon and sulfur isotopes in Precambrian sediments from the Canadian Shield. *Geochimica et Cosmochimica Acta*, 50, pp. 2653-2662.

Stott, G. M. & Schwerdtner, W. M. (1981). A structural analysis of the central part of the Shebandowan metavolcanic metasedimentary belt: Ontario Geological Survey Open-File Report 5349, 44 pp.

Stott, G.M. & Schnieders, B.R. (1983). Gold mineralization in the Shebandowan belt and its relation deformation patterns; in the geology of gold in Ontario, Ontario Geological Survey, Miscellaneous Paper 110, pp.181-193.

Stott, G.M. (1985). A structural analysis of the central part of the Archean Shebandowan greenstone belt and a crescent-shaped granitoid pluton, northwestern Ontario; unpublished PhD thesis, University of Toronto, Toronto, Ontario, 285 pp.

Stott, G.M. (2011). A revised terrane subdivision of the Superior Province in Ontario; Ontario Geological Survey, Miscellaneous Release—Data 278.

Taner, M.F, Drever, C., Yakymchuk, C., & Longstaffe, F.J. (2017). Origin of graphite in the Southwestern Grenville province. *Canadian Mineralogist 55*, pp. 1041–1055. https://doi.org/10.3749/canmin.1700029

Taylor, Jr, H.A. (2006). Graphite. In: Kogel, J., Trivedi, N., Barker, J., Krukowski, S. (eds), Industrial Minerals & Rocks. Society for Mining, Metallurgy, and Exploration. pp. 507–519.

Thurston, P.C. (1991). Archean geology of Ontario: Introduction; *in* Geology of Ontario, Ontario Geological Survey, Special v.4, pt.1, pp.73–80.

Toma, J., Creaser, R.A., Card, C., Stern, R.A., Chacko, T., & Steele-McInnis, M. (2022). Re-Os Systematics and Chronology of Graphite: *Geochimica et Cosmochimica Acta, 323*, pp. 164–182, https://doi.org/10.1016/j.gca.2022.02.012.

Toma, J. & Creaser, R.A. (2023). Did subducted graphite fertilize the Franciscan mantle wedge with radiogenic Os? *Geology; 51* (11), pp. 1057–1061. doi: https://doi.org/10.1130/G51331.1

Touret, J.L.R, Huizengab, J.M., Kehelpannalad, K.V.W., & Piccolia, F. (2019). Vein-type graphite deposits in Sri Lanka: The ultimate fate of granulite fluids. *Chemical Geology 508*, pp. 167–181.

Touret, J.L.R. (2001). Fluids in metamorphic rocks. *Lithos* 55: pp. 1–25

Qing, J., Richards, V. L. & Van Aken, D. C. (2017). Growth stages and hexagonal-rhombohedral structural arrangements in spheroidal graphite observed in ductile iron. *Carbon 116*, pp. 456-469.

Upton, P. & Craw, D. (2008). Modelling the role of graphite in development of a mineralised mid-crustal shear zone, Macraes mine, New Zealand. *Earth Planet Sci Letters* 266: pp. 245-255.

Upton, P. & Craw, D. (2014). Modelling of structural and lithological controls on mobility of fluids and gold in orogenic belts, New Zealand. In: Garofalo PS, Ridley JR (eds) Gold-Transporting Hydrothermal Fluids in the Earth's Crust. *Geol Soc London Special Publ*. 402: pp. 231-253.

Verma, C., & Quraishi, M. A. (Eds.). (2023). Activated carbon: Progress and applications. *Royal Society of Chemistry*. 450pp.

Walker, R.G. and James, N.P. (1992). Facies models, response to sea level changes; Geological Association of Canada, 409pp.

Weiblen, P.W., Mathez, E.A. & Morey, G.B. (1972). Logan intrusions; *in* Geology of Minnesota: A Centennial Volume, Minnesota Geological Survey, pp. 394-406.

Weis, P.L., Friedman, I. & Gleason, J.P. (1981). The origin of epigenetic graphite: evidence from isotopes. *Geochimica et Cosmochimica Acta 45*, pp. 2325-2332.

Whitney, D.L. & Evans, B.W. (2010). Abbreviations for names of rock-forming minerals. *American Mineralogist 95*, pp. 185-187.

Williams, H.R., Stott, G.M., Heather, K.B., Muir, T.L. & Sage, R.P. (1991). Wawa Subprovince; *in* Geology of Ontario, Ontario Geological Survey, Special 4-1, pp. 485–542.

Williams, D.B. & Carter, C.B. (1996). Transmission electron microscopy: a textbook for materials science. *Plenum Press*, 729 pp.

Wopenka, B. & Pasteris, J.D. (1993). Structural characterization of kerogens to granulite facies graphite: Applicability of Raman microprobe spectroscopy. *American Mineralogist*. 78, pp. 533‑577.

Wu, C., & Chen, H. (2015). Revised Ti-in-biotite geothermometer for ilmenite- or rutile-bearing crustal metapelites. *Science Bulletin*, 60, pp. 116-121.

Yavuz, F., Kumral, M., Karakaya, N., Karakaya, M.Ç., & Yildirim, D.K. (2015). A Windows program for chlorite calculation and classification. *Computers & Geosciences*, 81, pp. 101-113.

Zhang, C., He, X., Sun, L., Santosh, M., Chi, J., Yu, X., Li, Z., & Meng, Y. (2023). Graphitization in Paleoproterozoic granulites from the Taihua Complex, North China Craton: Constraints from laser Raman spectroscopy, carbon isotopes and geochronology. *Lithos 454-455*, 16pp.

Appendix A (Table 4.2): *Electron microprobe analysis for the Rockstone host rock and vein-hosted chlorite.*

Sample no	RS22-01-1a-1	RS22-01-1a-2	RS22-01-1a-3	RS22-01-1a-4	RS22-01-1a-5	RS22-01-1a-6	RS22-01-2-HR-1	RS22-01-2-HR-2	RS22-01-4-1
Composition (wt %)									
SiO_2	28.68	27.20	27.49	27.28	26.83	27.26	30.16	29.97	30.34
TiO_2	0.01	0.01	0.01	0.01	0.02	0.02	0.00	0.01	0.00
Al_2O_3	12.86	14.76	14.85	15.25	15.19	15.39	20.37	21.01	21.19
FeO_t	37.20	36.90	37.44	36.79	36.76	36.14	4.60	4.66	4.66
MnO	0.21	0.19	0.26	0.19	0.20	0.22	0.19	0.20	0.32
MgO	9.04	8.06	7.83	7.85	7.16	7.85	31.63	31.60	31.62
CaO	0.36	0.19	0.25	0.28	0.31	0.25	0.18	0.04	0.01
Na_2O	0.00	0.02	0.01	0.01	0.02	0.02	0.00	0.00	0.00
Total	88.36	87.33	88.14	87.66	86.49	87.15	87.13	87.29	87.2
Calculated formulae (all values in *a.p.f.u.*) on the basis of 28 oxygen									
Si	6.40	6.15	6.17	6.13	6.07	6.14	5.71	5.65	5.68
Al (iv)	1.60	1.86	1.84	1.88	1.94	1.87	2.28	2.34	2.31
Al (vi)	1.78	2.07	2.08	2.16	2.18	2.21	2.26	2.33	2.36
Ti	0.00	0.00	0.00	0.00	0.00	0.00	0.00	0.00	0.00
Fe	6.95	6.98	7.02	6.92	7.08	6.81	0.72	0.73	0.73
Mn	0.04	0.04	0.05	0.04	0.04	0.04	0.03	0.03	0.05
Mg	3.01	2.71	2.62	2.63	2.45	2.63	8.93	8.89	8.83
Ca	0.08	0.04	0.06	0.06	0.07	0.06	0.04	0.01	0.00
Na	0.01	0.01	0.00	0.00	0.01	0.01	0.00	0.00	0.00
Fe/(Fe+Mg)	0.70	0.72	0.73	0.72	0.74	0.72	0.07	0.08	0.08
*T(°C)	154	180	177	181	186	181	285	291	288

*****Temperature estimation according to Cathelineau and Nieva (1985); HR: host rock.

Table 4.2: *(continued).*

Sample no	RS22-01-4-2	RS22-01-5a-1	RS22-01-5a-2	RS22-01-5a-3	RS22-01-5a-4	RS22-01-5a-5	RS22-01-5a-6	RS22-01-5a-7	RS22-01-5b-1
Oxide composition (wt %)									
SiO_2	28.57	28.27	28.09	28.39	28.53	27.98	27.18	29.64	28.14
TiO_2	0.00	0.01	0.01	0.00	0.01	0.00	0.02	0.01	0.03
Al_2O_3	19.27	13.43	13.73	14.11	14.37	14.77	15.42	20.80	14.20
FeO_t	17.15	36.87	36.70	35.72	35.35	36.48	36.31	8.40	36.91
MnO	0.58	0.23	0.24	0.22	0.26	0.23	0.31	0.26	0.21
MgO	22.21	8.58	8.31	8.44	8.44	8.09	7.56	27.80	8.22
CaO	0.03	0.15	0.19	0.22	0.25	0.18	0.28	0.02	0.16
Na_2O	0.01	0.03	0.01	0.00	0.00	0.00	0.00	0.02	0.03
Total	87.82	87.57	87.28	87.1	87.21	87.73	87.08	86.95	87.9
Calculated formulae (all values in *a.p.f.u.*) on the basis of 28 oxygen									
Si	5.74	6.36	6.34	6.38	6.38	6.26	6.14	5.73	6.30
Al (iv)	2.25	1.65	1.67	1.64	1.64	1.75	1.88	2.27	1.71
Al (vi)	2.31	1.91	1.98	2.08	2.14	2.14	2.23	2.46	2.03
Ti	0.00	0.00	0.00	0.00	0.00	0.00	0.00	0.00	0.01
Fe	2.88	6.94	6.93	6.71	6.61	6.83	6.86	1.35	6.91
Mn	0.10	0.04	0.05	0.04	0.05	0.04	0.06	0.04	0.04
Mg	6.66	2.88	2.79	2.82	2.81	2.70	2.54	8.01	2.74
Ca	0.01	0.04	0.05	0.05	0.06	0.04	0.07	0.00	0.04
Na	0.00	0.01	0.00	0.00	0.00	0.00	0.00	0.01	0.01
Fe/(Fe+Mg)	0.30	0.71	0.71	0.70	0.70	0.72	0.73	0.14	0.72
*T(°C)	261	158	161	159	159	169	181	278	165

Table 4.2: *(continued).*

Sample no	RS22-01-5b-2	RS22-01-5b-3	RS22-01-5b-4	RS22-01-5b-5	RS22-03-1-HR	RS22-03-9b-1	RS22-03-9b-2	RS22-04-8-1	RS22-04-8-2
Oxide composition (wt %)									
SiO_2	25.25	29.48	27.95	30.37	34.41	28.01	27.81	27.61	27.68
TiO_2	0.01	0.01	0.02	0.03	0.06	0.01	0.00	0.17	0.06
Al_2O_3	14.42	12.25	14.18	19.42	16.73	14.94	14.65	18.73	18.98
FeO_t	44.51	34.50	36.55	24.12	11.98	27.67	27.00	27.36	28.71
MnO	0.19	0.20	0.25	0.23	0.54	2.87	2.72	0.25	0.32
MgO	2.89	10.74	8.18	12.60	22.66	13.68	14.08	12.93	12.19
CaO	0.17	0.16	0.17	0.18	1.50	0.20	0.22	0.06	0.07
Na_2O	0.03	0.02	0.03	0.00	0.06	0.02	0.01	0.03	0.02
Total	87.47	87.36	87.33	86.95	87.63	87.4	86.49	87.14	88.03
Calculated formulae (all values in *a.p.f.u.*) on the basis of 28 oxygen									
Si	5.99	6.55	6.30	6.32	6.67	6.09	6.10	5.89	5.89
Al (iv)	2.00	1.46	1.72	1.75	1.39	1.90	1.90	2.13	2.13
Al (vi)	2.02	1.75	2.04	3.01	2.42	1.92	1.88	2.58	2.62
Ti	0.00	0.00	0.00	0.01	0.01	0.00	0.00	0.03	0.01
Fe	8.83	6.41	6.89	4.20	1.94	5.03	4.95	4.88	5.11
Mn	0.04	0.04	0.05	0.04	0.09	0.53	0.51	0.05	0.06
Mg	1.02	3.56	2.74	3.91	6.54	4.43	4.60	4.11	3.86
Ca	0.04	0.04	0.04	0.04	0.32	0.05	0.05	0.01	0.02
Na	0.01	0.01	0.01	0.00	0.02	0.01	0.00	0.01	0.01
Fe/(Fe+Mg)	0.90	0.64	0.72	0.52	0.23	0.53	0.52	0.54	0.57
*T(°C)	179	144	165	187	177	202	203	225	223

Table 4.2: *(continued).*

Sample no	RS22-04-8-3	RS22-04-9a-1	RS22-04-9a-2	RS22-04-12-1	RS22-04-12-2	RS22-04-12-3	RS22-04-12-4	RS22-04-12-5
Oxide composition (wt %)								
SiO_2	31.48	27.05	26.28	29.90	29.65	30.20	29.56	30.74
TiO_2	1.03	0.01	0.03	0.02	0.02	0.01	0.04	0.01
Al_2O_3	18.64	18.20	18.87	21.75	21.29	21.27	21.31	20.63
FeO_t	11.67	33.11	33.58	3.26	3.55	3.56	3.75	5.36
MnO	0.50	0.28	0.16	0.51	0.56	0.56	0.59	0.68
MgO	23.42	7.92	8.65	31.41	31.24	31.11	30.83	29.31
CaO	0.96	0.17	0.09	0.02	0.02	0.01	0.03	0.06
Na_2O	0.58	0.02	0.03	0.01	0.00	0.01	0.01	0.17
Total	87.65	86.76	98.59	87.69	86.33	86.73	86.12	86.96
Calculated formulae (all values in *a.p.f.u.*) on the basis of 28 oxygen								
Si	6.11	6.00	5.78	5.64	5.61	5.71	5.65	5.85
Al (iv)	1.94	2.04	2.24	2.36	2.39	2.29	2.35	2.16
Al (vi)	2.32	2.71	2.65	2.47	2.47	2.45	2.44	2.46
Ti	0.15	0.00	0.01	0.00	0.00	0.00	0.01	0.00
Fe	1.89	6.14	6.18	0.51	0.56	0.56	0.59	0.85
Mn	0.08	0.05	0.03	0.08	0.09	0.09	0.10	0.11
Mg	6.78	2.61	2.83	8.84	8.81	8.78	8.78	8.32
Ca	0.20	0.04	0.02	0.00	0.00	0.00	0.01	0.01
Na	0.22	0.01	0.01	0.00	0.00	0.00	0.00	0.06
Fe/(Fe+Mg)	0.22	0.70	0.69	0.05	0.06	0.06	0.06	0.09
*T(°C)	235	200	223	295	298	287	294	270

Appendix B (Table 4.3): *Electron microprobe analysis of vein-hosted dioctahedral micas.*

Sample no	RS22-01-5a-1	RS22-01-5a-2	RS22-01-5a-3	RS22-04-9a-1	RS22-04-9a-2	RS22-04-9a-3	RS22-04-9a-4	RS22-04-12-1
Oxide composition (wt %)								
SiO_2	45.47	47.91	46.96	46.58	47.69	46.73	46.97	47.66
TiO_2	0.26	0.24	0.21	0.37	0.24	0.73	0.36	0.21
Al_2O_3	31.01	26.09	26.24	30.80	32.51	32.15	31.49	30.16
FeO_t	4.15	6.43	4.82	1.86	0.70	0.35	0.96	0.42
MnO	0.03	0.07	0.06	0.06	0.00	0.00	0.03	0.02
MgO	2.92	4.30	6.00	3.76	2.42	2.54	3.90	3.86
CaO	0.00	0.02	0.01	0.01	0.01	0.00	0.00	0.01
Na_2O	0.30	0.33	0.28	0.23	0.27	0.27	0.25	0.24
K_2O	10.20	8.06	8.37	10.65	11.08	11.31	10.79	11.08
F	0.11	0.15	0.09	0.14	0.02	0.01	0.19	0.15
Total	94.45	93.60	93.04	94.46	94.94	94.09	94.94	93.80
Calculated formulae (all values in a.p.f.u.) on the basis of 11 oxygen								
Si	3.11	3.30	3.24	3.16	3.18	3.16	3.15	3.23
Ti	0.01	0.01	0.01	0.02	0.01	0.04	0.02	0.011
Al (iv)	0.89	0.70	0.76	0.85	0.82	0.85	0.85	0.77
Al (vi)	1.61	1.42	1.38	1.61	1.74	1.71	1.64	1.64
Fe (tot)	0.24	0.37	0.28	0.11	0.04	0.02	0.05	0.02
Mg	0.30	0.44	0.62	0.38	0.24	0.26	0.39	0.39
Mn	0.00	0.00	0.00	0.00	0.00	0.00	0.00	0.00
Na	0.04	0.04	0.04	0.03	0.04	0.04	0.03	0.03
K	0.89	0.71	0.74	0.92	0.94	0.97	0.92	0.96
Ca	0.00	0.00	0.00	0.00	0.00	0.00	0.00	0.00
F	0.02	0.03	0.02	0.03	0.00	0.00	0.04	0.03
OH	1.98	1.97	1.98	1.97	2.00	2.00	1.96	1.97
M site	2.16	2.25	2.29	2.12	2.03	2.02	2.11	2.06
Mg/(Mg+Fe)	0.56	0.54	0.69	0.78	0.86	0.93	0.88	0.94

Appendix B (Table 4.4): *Electron microprobe analysis of vein-hosted trioctahedral micas.*

Sample no	RS22-04-8	RS22-04-9a-5	RS22-04-9a-6	RS22-04-12-2	RS22-04-12-3
Oxide composition (wt %)					
SiO_2	40.88	40.23	41.18	40.52	40.21
TiO_2	0.99	1.05	0.84	0.83	0.83
Al_2O_3	18.06	17.26	17.55	17.65	17.99
FeOt	4.34	2.11	3.48	2.09	2.06
MnO	0.33	0.17	0.17	0.27	0.28
MgO	20.25	22.88	21.58	22.62	22.74
CaO	0.19	0.02	0.03	0.02	0.00
Na_2O	0.49	0.11	0.47	0.10	0.09
K_2O	9.82	10.67	9.92	10.57	10.62
F	1.78	1.87	1.65	2.03	1.74
Total	96.59	96.37	96.87	96.70	96.56
Calculated formulae (all values in a.p.f.u.) on the basis of 11 oxygen					
Si	2.88	2.85	2.89	2.86	2.83
Ti	0.05	0.056	0.044	0.044	0.044
Al (iv)	1.12	1.15	1.11	1.14	1.17
Al (vi)	0.38	0.28	0.34	0.32	0.33
Fe (tot)	0.26	0.13	0.20	0.12	0.12
Mg	2.13	2.41	2.26	2.38	2.39
Mn	0.02	0.01	0.01	0.02	0.02
Na	0.07	0.02	0.06	0.01	0.01
K	0.88	0.96	0.89	0.95	0.95
Ca	0.01	0.00	0.00	0.00	0.00
F	0.40	0.42	0.37	0.45	0.39
OH	1.60	1.58	1.63	1.55	1.61
M site	2.83	2.89	2.86	2.88	2.89
Mg/(Mg+Fe)	0.89	0.95	0.92	0.95	0.95

Appendix B (Table 4.5): *Electron microprobe analysis of host rock micas.*

Sample no	RS22-03-1	RS22-04-10a-1	RS22-04-10a-2	RS22-04-10a-3
Oxide composition (wt %)				
SiO_2	48.16	38.48	38.69	38.59
TiO_2	0.56	2.10	2.16	1.29
Al_2O_3	31.89	14.80	14.95	15.60
FeOt	0.25	11.12	11.87	12.08
MnO	0.04	0.26	0.26	0.25
MgO	2.90	17.52	16.97	16.71
CaO	0.01	0.04	0.02	0.02
Na_2O	0.23	0.08	0.07	0.06
K_2O	10.97	10.13	9.90	10.03
F	0.26	0.39	0.23	0.39
Total	95.27	94.92	95.12	95.02
Calculated formulae (all values in a.p.f.u.) on the basis of 11 oxygen				
Si	3.20	2.85	2.86	2.86
Ti	0.03	0.117	0.120	0.072
Al (iv)	0.80	1.15	1.14	1.14
Al (vi)	1.70	0.14	0.16	0.22
Fe (tot)	0.01	0.69	0.73	0.75
Mg	0.29	1.94	1.87	1.85
Mn	0.00	0.02	0.02	0.02
Na	0.03	0.01	0.01	0.01
K	0.93	0.96	0.93	0.96
Ca	0.00	0.00	0.00	0.00
F	0.05	0.09	0.05	0.09
OH	1.95	1.91	1.95	1.91
M site	2.04	2.90	2.90	2.90
Mg/(Mg+Fe)	0.95	0.74	0.72	0.71
*T(°C)	N/A	562.60	569.10	501.10

*Temperature estimation according to Wu and Chen (2015).

Appendix C: *Raman spectroscopy of vein-hosted graphite samples*.

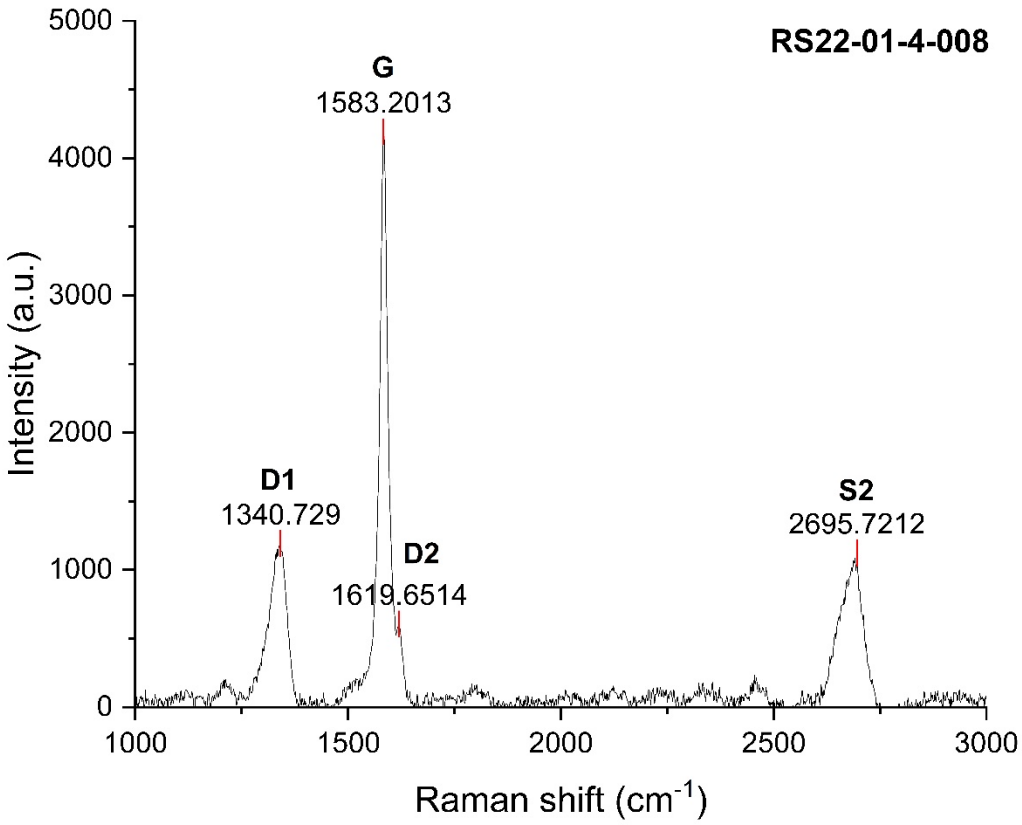

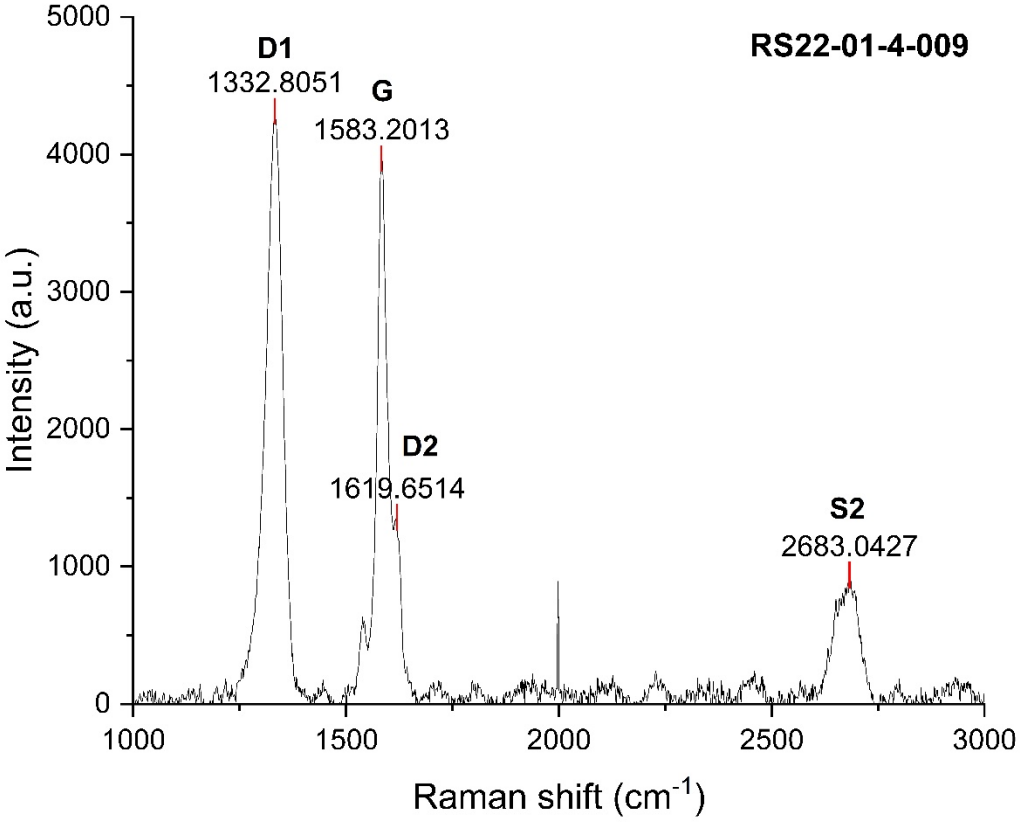
RS22-01-4-009
D1
1332.8051
G
1583.2013
D2
1619.6514
S2
2683.0427
Intensity (a.u.)
Raman shift (cm-1)
5000
4000
3000
2000
1000
0
1000
1500
2000
2500
3000

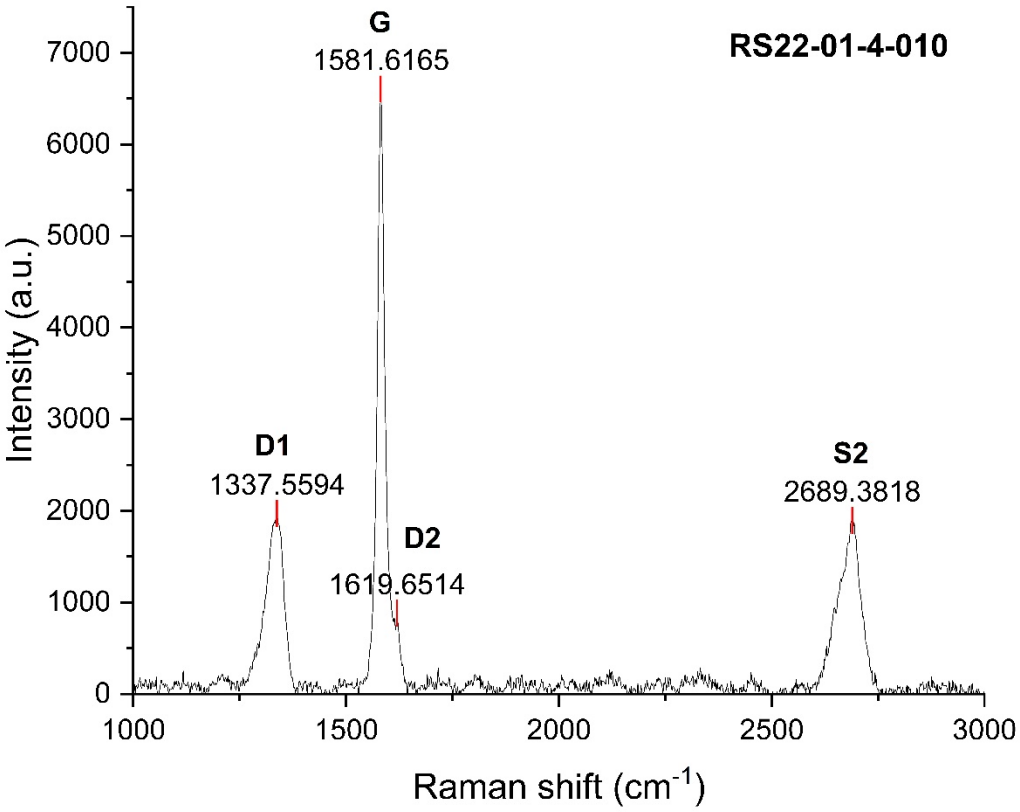
G
1581.6165
RS22-01-4-010
D1
1337.5594
D2
1619.6514
S2
2689.3818
Intensity (a.u.)
Raman shift (cm-1)
7000
6000
5000
4000
3000
2000
1000
0
1000
1500
2000
2500
3000

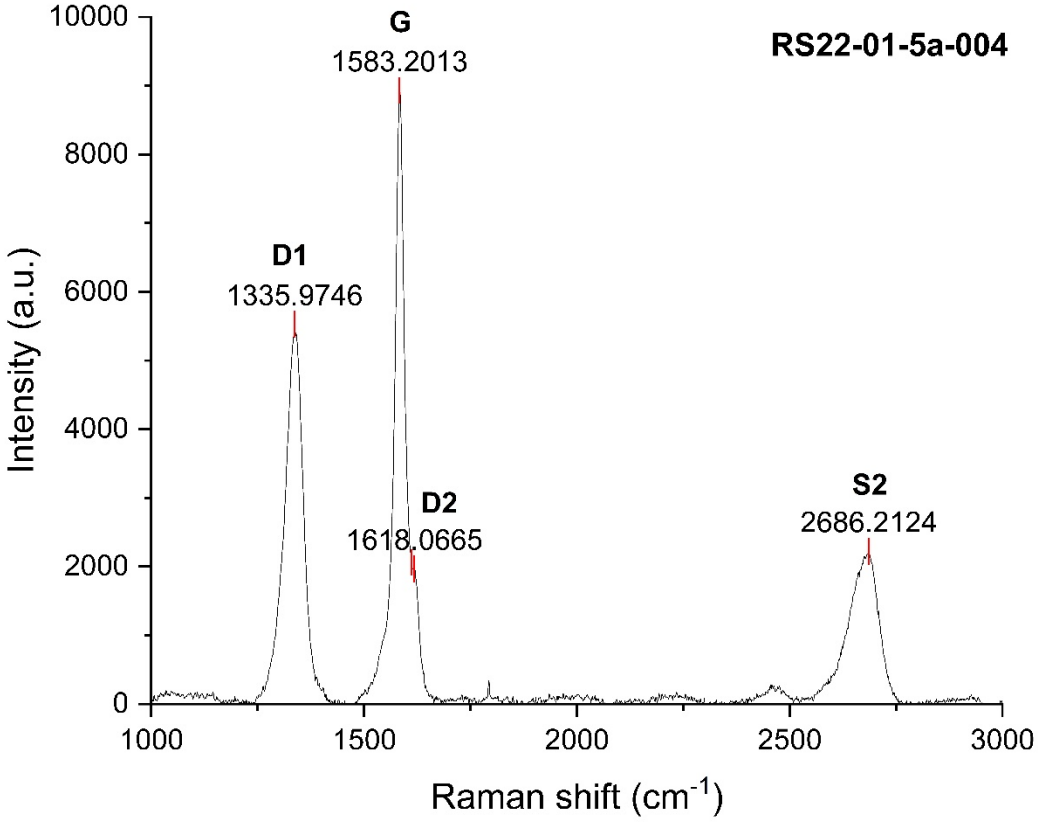
RS22-01-5a-004
G
1583.2013
D1
1335.9746
D2
1618.0665
S2
2686.2124
Intensity (a.u.)
Raman shift (cm-1)
10000
8000
6000
4000
2000
0
1000
1500
2000
2500
3000

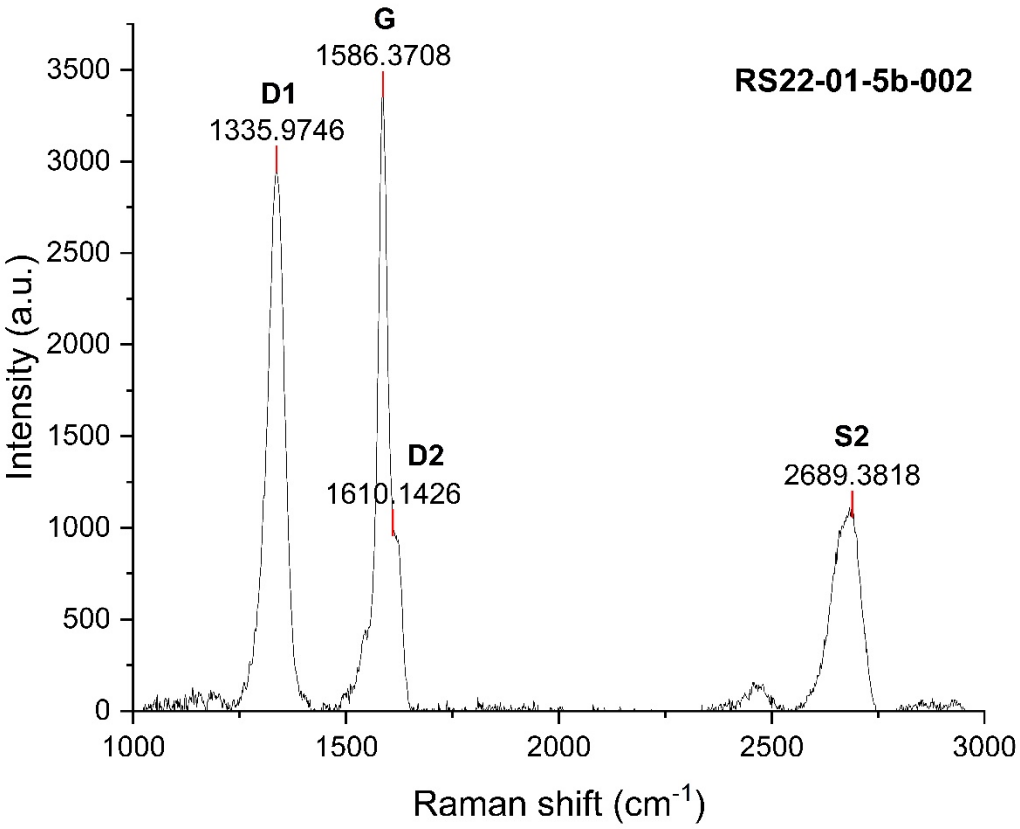
G
1586.3708
D1
1335.9746
RS22-01-5b-002
D2
1610.1426
S2
2689.3818
Intensity (a.u.)
Raman shift (cm-1)
0
500
1000
1500
2000
2500
3000
3500
1000
1500
2000
2500
3000

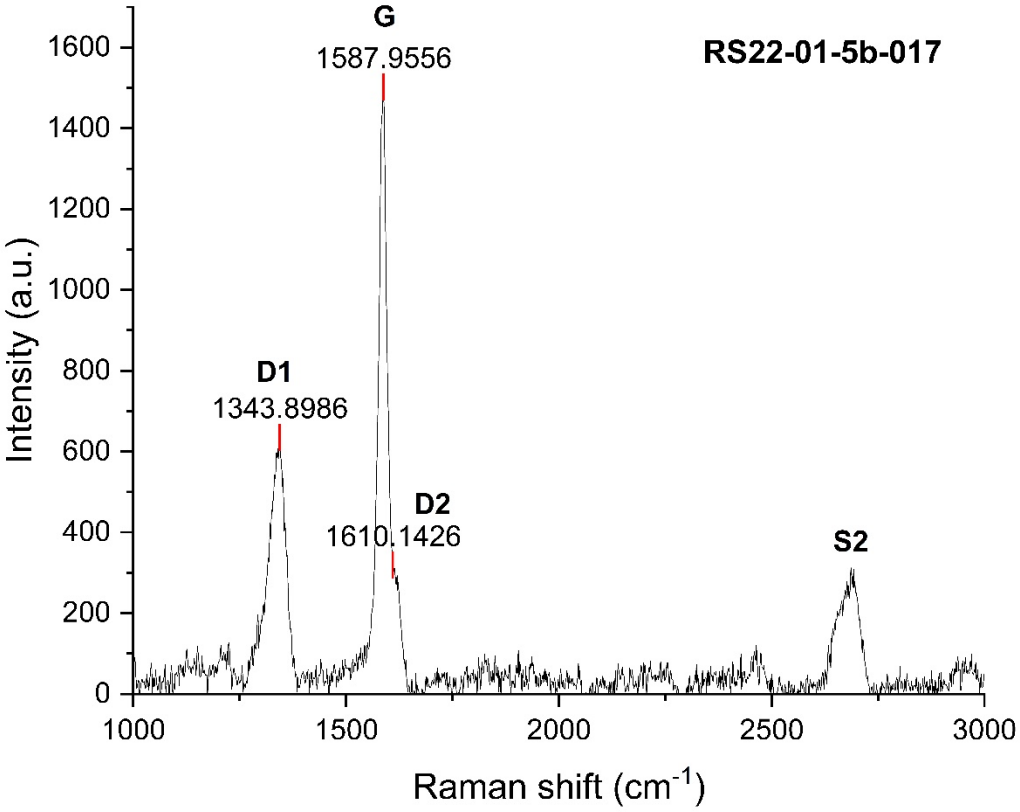
G
1587.9556
RS22-01-5b-017
D1
1343.8986
D2
1610.1426
S2
Intensity (a.u.)
Raman shift (cm-1)
0
200
400
600
800
1000
1200
1400
1600
1000
1500
2000
2500
3000

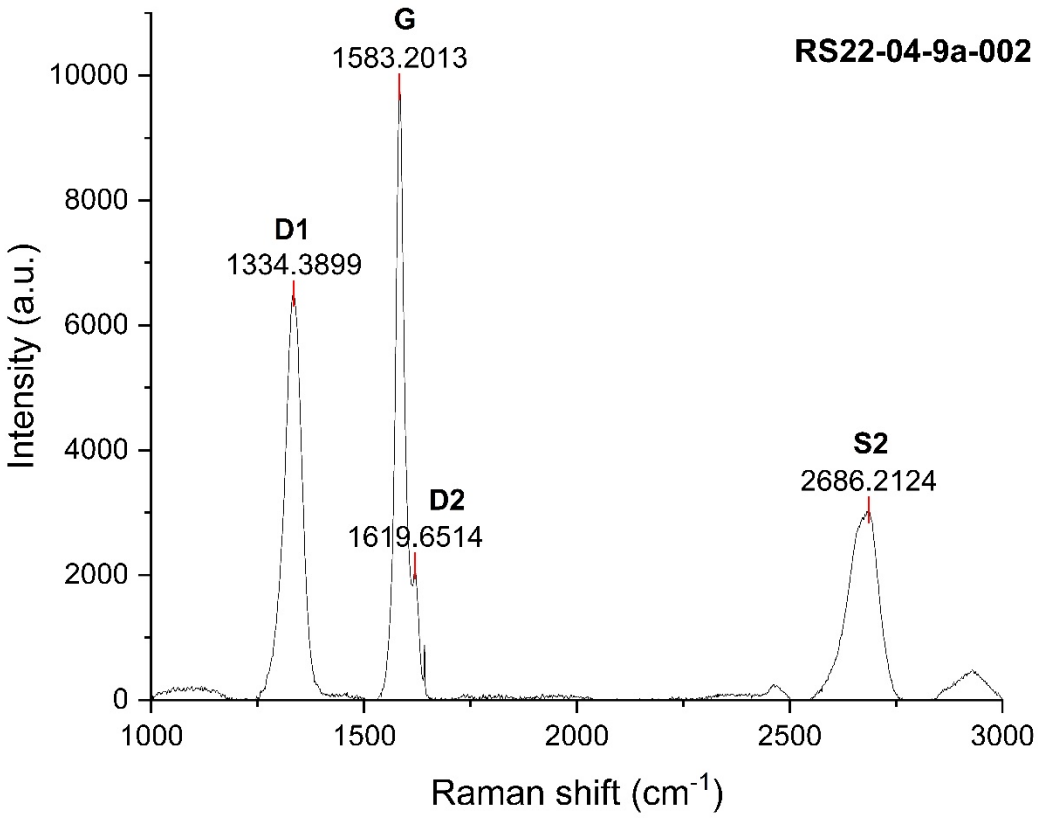
G
1583.2013
RS22-04-9a-002
D1
1334.3899
D2
1619.6514
S2
2686.2124
Intensity (a.u.)
Raman shift (cm-1)
0
2000
4000
6000
8000
10000
1000
1500
2000
2500
3000

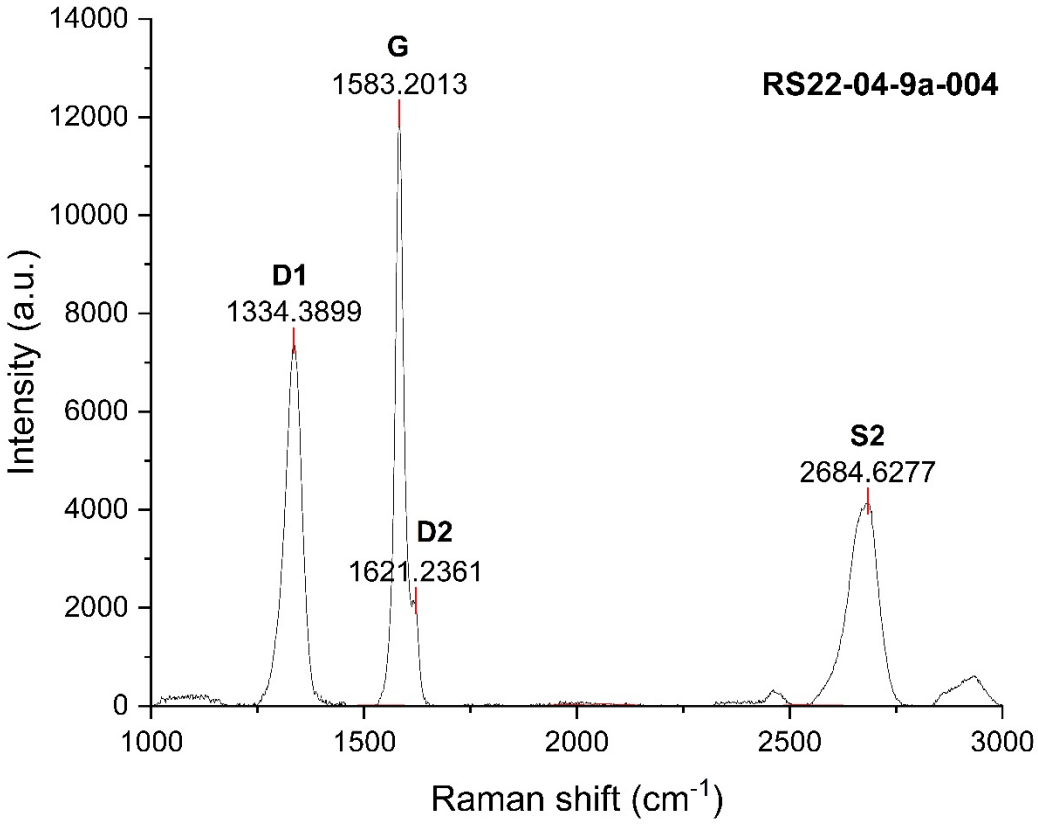
G
1583.2013
RS22-04-9a-004
D1
1334.3899
D2
1621.2361
S2
2684.6277
Intensity (a.u.)
Raman shift (cm-1)
14000
12000
10000
8000
6000
4000
2000
0
1000
1500
2000
2500
3000

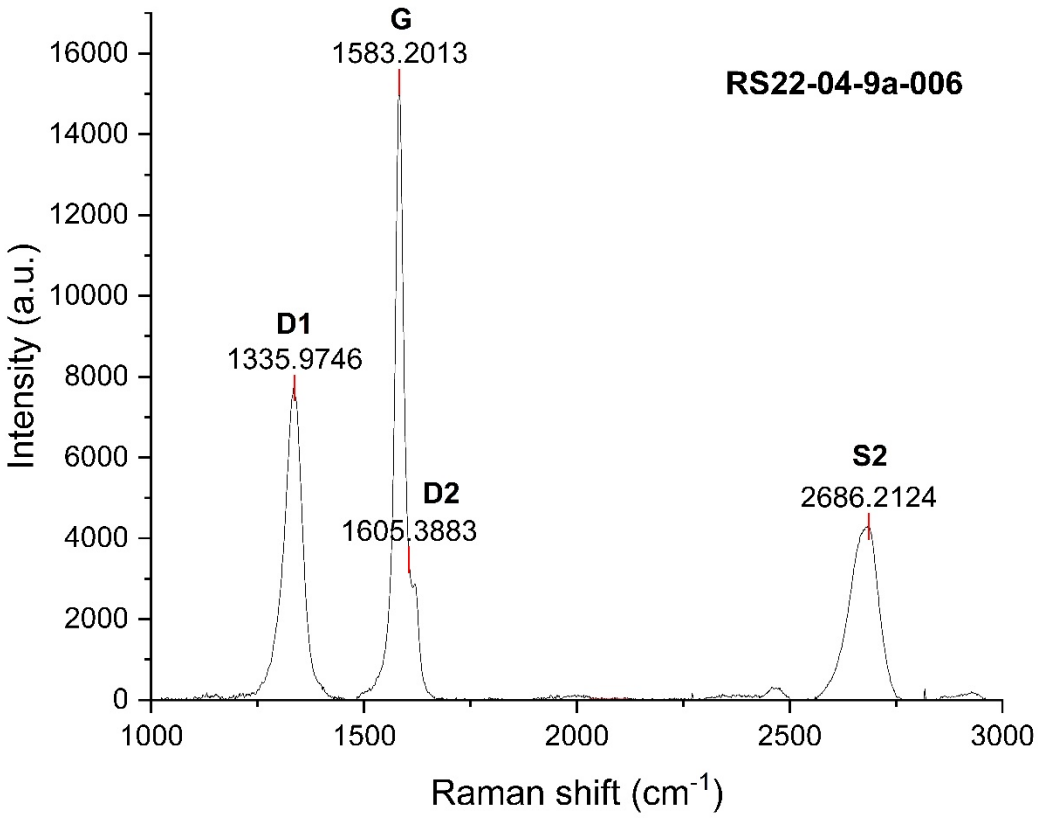
G
1583.2013
RS22-04-9a-006
D1
1335.9746
D2
1605.3883
S2
2686.2124
Intensity (a.u.)
Raman shift (cm-1)
16000
14000
12000
10000
8000
6000
4000
2000
0
1000
1500
2000
2500
3000

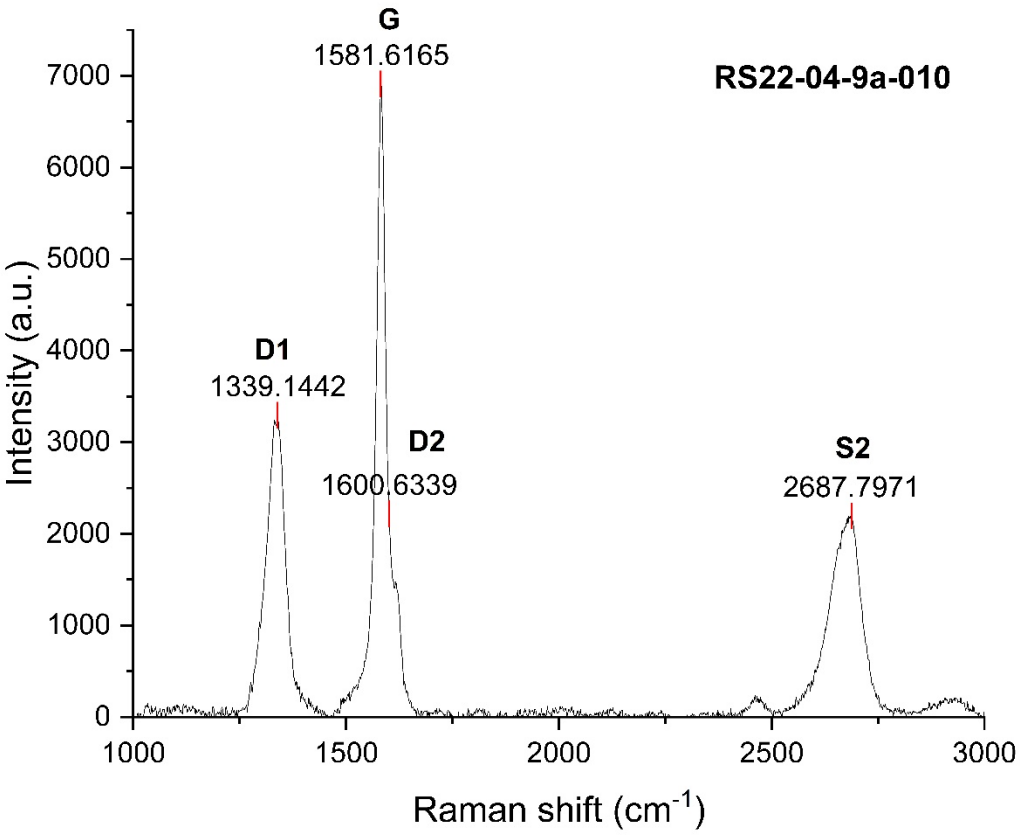
G
1581.6165
RS22-04-9a-010
D1
1339.1442
D2
1600.6339
S2
2687.7971
Intensity (a.u.)
Raman shift (cm-1)
0
1000
2000
3000
4000
5000
6000
7000
1000
1500
2000
2500
3000

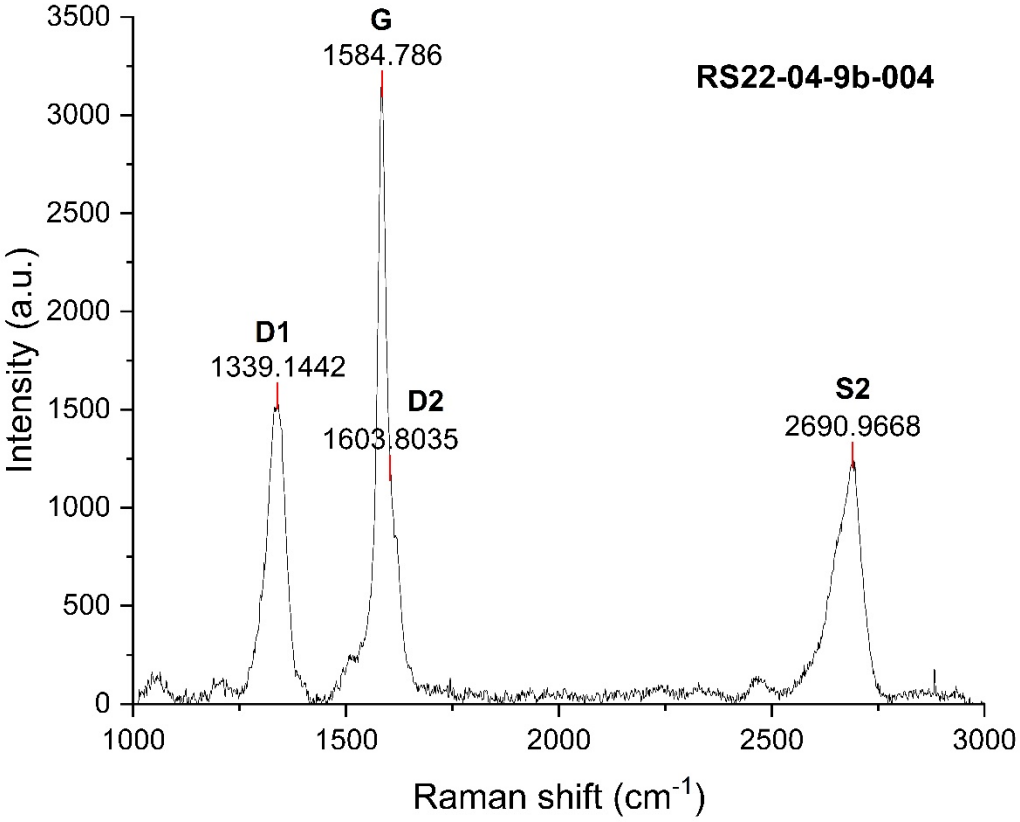
G
1584.786
RS22-04-9b-004
D1
1339.1442
D2
1603.8035
S2
2690.9668
Intensity (a.u.)
Raman shift (cm-1)
3500
3000
2500
2000
1500
1000
500
0
1000
1500
2000
2500
3000

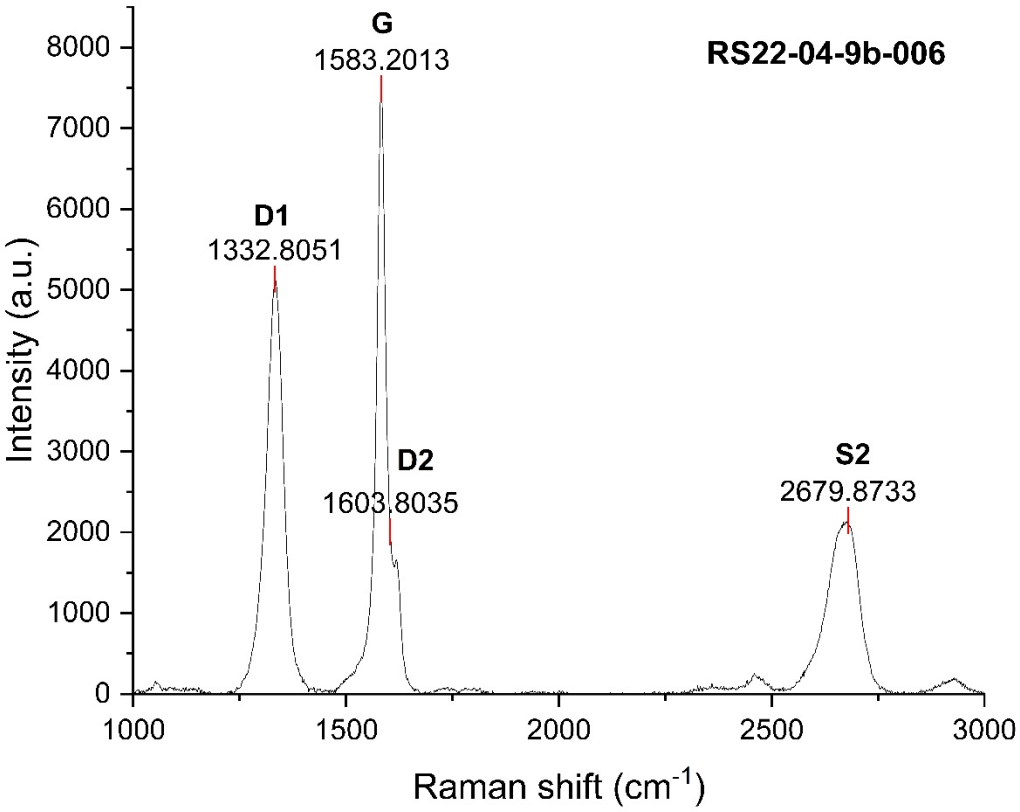
G
1583.2013
RS22-04-9b-006
D1
1332.8051
D2
1603.8035
S2
2679.8733
Intensity (a.u.)
Raman shift (cm-1)
8000
7000
6000
5000
4000
3000
2000
1000
0
1000
1500
2000
2500
3000